Journal of Fluids and Structures 70 (2017) 464–499

Contents lists available at ScienceDirect

Journal of Fluids and Structures

journal homepage: www.elsevier.com/locate/jfs

Fluid–structure interactions in a cylindrical layered wave guide with application in the spinal column to syringomyelia☆

Novak S.J. Elliott[a,b,*], Anthony D. Lucey[a], Duncan A. Lockerby[c], Andrew R. Brodbelt[d]

[a] Fluid Dynamics Research Group, Department of Mechanical Engineering, Curtin University, GPO Box U1987, Perth, WA 6845, Australia
[b] El Grupo de Investigación de la Dinámica de Fluidos, Xe' Lajuj No'j, Apartado Postal No. 247, Quetzaltenango 09001, Guatemala
[c] Fluid Dynamics Research Centre, School of Engineering, University of Warwick, Coventry CV4 7AL, United Kingdom
[d] The Walton Centre NHS Foundation Trust, Liverpool, L9 7LJ, United Kingdom

ARTICLE INFO

Keywords:
Eigenvalue
Wave propagation
Dispersion
Syringomyelia
Homeostasis

ABSTRACT

Syringomyelia is a disease of the spinal cord in which fluid-filled cavities, called syrinxes, form and expand, compressing the surrounding neural tissue and producing neurological damage. This condition can occur following spinal injury and has limited treatment options in part because of a lack of understanding of its origins. Current pathogenic theories make predictions from localised disturbances in the cerebrospinal fluid dynamics. The poroelastic spinal cord tissues have an effective compressibility as a result of the localised displacement of the intercellular fluid. Also, despite the disease progressing over months and years, the mechanical perturbations from the heart and breathing cycles and from coughs and sneezes operate over much shorter timescales of seconds down to fractions of a second, respectively. To model these pathological features, we solve the harmonic eigenvalue problem for a two-dimensional elastic fluid–solid cylindrically layered waveguide. We analyse the dispersion behaviour and mode shapes over a wide wavelength spectrum and investigate the influence of Poisson's ratio on the wave mode characteristics. The healthy model consists of an elastic solid cylinder (spinal cord) and a surrounding annulus of inviscid fluid (cerebrospinal fluid in the subarachnoid space). To model syringomyelia we then add a cylindrical fluid space (syrinx) within the elastic cylinder. For the geometry with the inner fluid conduit present (diseased spinal cord in situ), the dispersion diagrams show three modes (0, 1, 2) that are propagatory across the wavelength spectrum. At long wavelengths, axial displacement dominates over radial, normal stress dominates over shear, but these become of the same order of magnitude as the wavelength approaches the radius of the elastic cylinder (spinal cord). Wave modes 0 and 1 induce relative motion between the elastic cylinder and the fluid contained within, which supports Williams's so-called slosh mechanism for syrinx lengthening, and all three modes involve stress concentrations (indicated by localised gradient peaks) in the inner wall of the elastic cylinder adjacent to the contained fluid, which would tend to support radial syrinx expansion. Mode 2 is the most sensitive to changes in Poisson's ratio (spinal cord tissue compressibility). We also investigate the progression of post-traumatic syringomyelia by simulating a sequence of discrete states in the gradual occlusion of the subarachnoid space and the subsequent formation and radial expansion of a syrinx. We predict that syrinx-fluid sloshing, hence the stress so induced, diminishes with the continued radial expansion of the syrinx. The largest normal stress concentrations at the syrinx boundary, which appear for modes 0 and 1, initially diminish with radial syrinx expansion; however, they

☆ Presented in part at the 6th Australasian Congress on Applied Mechanics, 12–15 Dec 2010, Perth WA, Australia (Elliott et al., 2010), and at the ASME Pressure Vessels and Piping Conference, 20–24 Jul 2014, Anaheim CA, USA (Elliott et al., 2014).

* Corresponding author at: Fluid Dynamics Research Group, Department of Mechanical Engineering, Curtin University, GPO Box U1987, Perth, WA 6845, Australia.
E-mail address: n.s.j.elliott@curtin.edu.au (N.S.J. Elliott).

http://dx.doi.org/10.1016/j.jfluidstructs.2016.11.007
Received 30 March 2016; Received in revised form 24 September 2016; Accepted 9 November 2016
Available online 07 March 2017

reach a minimum value for intermediate syrinx diameters. On this basis we hypothesize that syrinx development may be part of a homeostatic mechanism to alleviate stress in the spinal cord. Understanding this process may aid in treatment development. The present work also has applications in industrial systems and serves as a platform for more advanced modelling of cylindrical waveguides in biological systems.

1. Introduction

1.1. Problem overview

This paper treats a fundamental problem in fluid–structure interaction (FSI), the dynamics of a cylindrical fluid–solid layered waveguide, which was inspired by and has application to the spinal disease syringomyelia. We study the wave-propagation characteristics of the spinal anatomy using the axisymmetric models depicted in Fig. 1(a) and 1(b), which contain, respectively, cross-sectional representations of the healthy spinal cord (SC) and a diseased SC with a fluid-filled cavity, termed a syrinx. We elucidate the dispersive properties of the spinal canal that have received little attention to date. Syringomyelia is a challenging condition to treat, with many patients developing progressive neurological disability that often does not improve with treatment. The present results are relevant, in particular, to the interpretation of measurements of CSF pulse waves and to understanding their potential role in syrinx development in post-traumatic syringomyelia. Understanding the cause will help improve treatment. Cylindrically-layered fluid–solid structures are a physiological building block, e.g., the arteries in the cardiovascular network and the ureter in the renal system, which may be augmented through pathologies (e.g., atherosclerosis) and associated treatments (e.g., catheter). More broadly, the analysis of the basic waveguide will also find applications in engineered systems.

Fig. 2 is the spinal anatomy represented by the engineering model depicted in Fig. 1(a). As shown, the soft SC lies within the protective confines of the bony canal formed through the vertebrae. Occupying the intervening annular space are the pia mater membrane, adhered to the cord surface, the cerebrospinal fluid (CSF) of the surrounding subarachnoid space, the bounding arachnoid mater and dura mater membranes, along with a collection of blood vessels (omitted in figure), nerves, fat and the ligaments that suspend the cord in place. The spine constitutes part of the wall that surrounds the thorax and abdomen. The epidural veins form a pair of channels that run the length of the anterior extradural aspect of the SC, and are connected to the veins of the spinal vertebrae, the attached muscles and the abdominal cavity. Any pressure perturbation in the thorax and abdomen will thus be transmitted to the spinal canal via these epidural veins.

We are concerned with wave propagation in our cylindrical models, which may be excited by a fluid pressure impulse. The pressure rise generated in the thorax and abdomen during coughing, or any similar percussive manoeuvre (sneezing, laughing, yawning, crying, valsalva), compresses the veins in the major body cavities, which displaces blood into the spinal epidural veins thereby transmitting most of the pressure rise along with it. As the contents of the spinal canal are essentially fluid-filled valveless flexible tubes, epidural pressure impulses are transmitted to the CSF, cord and membranes as waves having speeds determined by the spinal dynamic compliance. In Williams's human coughing experiments (Williams, 1972, 1976; Lockey et al., 1975), the so-induced CSF pressure impulses were of approximately 1 s duration with an abdominal pressure rise of 10–13 kPa (75–100 mm Hg) and had speeds of around 4.5 m/s. The ejection airspeeds of coughs and sneezes themselves were shown recently to reach similar values (Tang et al., 2013).

We now look at the progress that has been made in mathematical modelling of the spinal canal and the limitations that persist, which provides the rationale for the present approach.

1.2. Background

1.2.1. General trends

Table 1 lists all mathematical modelling papers published in peer-reviewed journals and edited books related to syringomyelia that model the flow of spinal CSF and intra-cord fluid using a continuum approach. These models have been categorized by their physics and mathematics, and within each category are ordered chronologically. Two-way fluid-structure interaction (2w-FSI) refers to the fully coupled solution of a fluid flow and the deformation of a flexible solid. One-way fluid-structure interaction (1w-FSI) models also have both fluid and solid motion but the latter is prescribed; i.e., the solid affects the fluid but not vice versa. The third physics category contains the computational fluid dynamics (CFD) models, which solve fluid flow through a static rigid geometry. There have been several studies published on the fluid mechanics at the craniocervical junction (e.g., Hentschel et al., 2010; Linge et al., 2011, 2014; Shaffer et al., 2014). Although these model the congenital condition Chiari malformation, which is found in around three quarters of all cases of syringomyelia (Williams, 1990), the fluid mechanics of the spinal canal itself was not in their scope, hence their omission from Table 1.

In the mathematics, we differentiate between analytical (Analyt) and numerical (Num) solutions; see Table 1 caption for an explanation of the various solution methods. The number of spatial dimensions (Dim) of the models are listed and a superscripted '∞' indicates that one of these dimensions (usually along the spinal axis) is infinite; i.e., there are no end conditions. The model geometries are either (i) idealized (1D, 2D, 3D), such as in a system of axisymmetric tubes, (ii) simplified (2D, 3D), in which anatomical-like

Nomenclature

Abbreviations

CSF	Cerebrospinal fluid
SC	Spinal cord
SSS	Spinal subarachnoid space

Latin symbols

D	A matrix differential operator
E	Young's modulus of elasticity
K	Bulk modulus
L	Discrete matrix approximation of the Helmholtz differential operator
R	Radius of spinal cord
U	Displacement amplitude as a function of radius
c	Phase speed
f	Frequency
k	Wave number
p	Pressure
r	Radial coordinate of the cylindrical system
t	Time
u	Displacement
z	Axial coordinate of the cylindrical system
$\mathfrak{L}$	Helmholtz differential operator

Greek symbols

Θ	Vector of discrete approximations of the scalar potentials
Λ	Wavelength
Φ	Amplitude of the scalar potential φ as a function of radius
Ψ	Amplitude of the scalar potential ψ
θ	Circumferential coordinate of the cylindrical system
λ	Lamé's first parameter of elasticity
μ	Shear modulus (Lamé's second parameter of elasticity)
ν	Poisson's ratio
ρ	Density
σ	Stress
φ	Scalar potential
ψ	Scalar potential
ω	Angular frequency

Subscripts

bulk	Refers to a property of the bulk compression wave
dura	Refers to a property of the dura mater
f	Refers to a property of a fluid layer
s	Refers to a property of a solid layer
s1	Refers to a property of the dilatational wave in an infinite elastic solid medium
s2	Refers to a property of the shear wave in an infinite elastic solid medium
syrinx	Refers to a property of a fluid-filled syrinx
N	Refers to the number of discretization points in the approximation of a Chebyshev polynomial
r	Refers to a quantity varying in the radial direction
rr	Refers to the normal component of the stress tensor in cylindrical coordinates
rz	Refers to the shear component of the stress tensor in cylindrical coordinates
z	Refers to a quantity varying in the axial direction
θ	Refers to a quantity varying in the circumferential direction

Superscripts

(n)	Denotes the order of the differential in the matrix operator M

Modifiers

~	Denotes a quantity multiplied by $i\omega$
˘	Denotes a quantity multiplied by ik_z
–	Denotes the inclusion of the boundary conditions in matrix L
^	Denotes a normalized quantity

features have been constructed from primitive shapes/volumes, or (iii) human (3D), which are reconstructions of realistic craniospinal anatomy from patient/volunteer magnetic resonance images (Geom: Ideal, Simple, Human, respectively). The constitutive models of the fluid (I: inviscid, V: viscous, V^{pore}: viscous fluid in a poroelastic matrix) and solid (LE: linear elastic, LVE: linear viscoelastic, LPE-Darcy/Biot: linear poroelastic based on Darcy flow or Biot's consolidation theory, respectively) components of the models are listed. For FSI models, we also point out if dispersion (Disp) is supported. The final pair of columns states whether the model was validated—if so, against what variable(s)—if not, the nature of the investigation, which often took the form of a parametric sensitivity study (PSS). The terms validation and verification are sometimes used interchangeably in the literature. They are, however, distinct concepts. Verification is a check of the mathematics to ensure that the equations are being solved correctly; an analytical solution can be used to verify a numerical one. Validation is a check of the physics to ensure that the correct equations are being solved; this is achieved by agreement between theoretical predictions and physical measurements of the system being studied.

Table 1 enables us to identify several broad trends between syringomyelia models. To begin with, of the FSI models (one-way and two-way), all but one (Støverud et al., 2016) have either idealized or simplified 1D or 2D geometries, which are often semi-infinite. In contrast, the CFD models are predominantly 3D, finite and anatomically realistic. This is explained by the need to simplify the more complex mechanics of the FSI systems to make them solvable and comprehensible, and to permit direct comparison of the rigid CFD model predictions with human pathologies. Most of the analytical models are 2w-FSI. These treat the fluids as inviscid and generally assume linear elastic solids and long wavelengths.[1] The numerical 2w-FSI models, on the other hand, are evenly split into two

[1] In a conference abstract, Cathalifaud et al. (2015) reported predictions of a 1D coaxial tubes model with viscous CSF and blood and poroelastic cord tissue; the non-linear solution was computed numerically while the linearised governing equation, a damped-wave equation, was solved analytically.

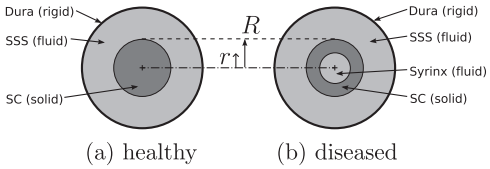

Fig. 1. Cross-sectional views of the semi-infinite axisymmetric models of the (a) healthy and (b) diseased spinal canal, with the elastic solid (spinal cord: SC), rigid solid (dura) and inviscid fluid (spinal subarachnoid space: SSS, syrinx) layers indicated; r is the radial coordinate and R is the SC radius.

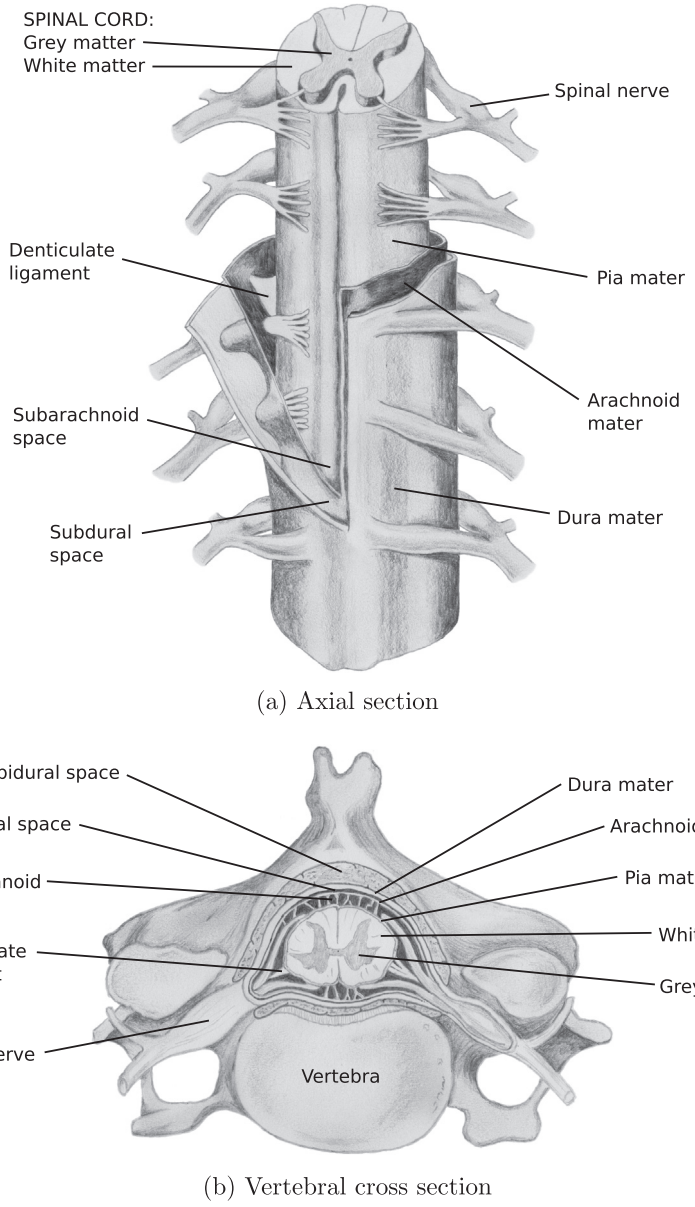

Fig. 2. The gross spinal anatomy showing a cylindrical structure composed of nervous tissues (spinal cord: grey matter and white matter, spinal nerves), elastic membranes (pia mater, arachnoid mater, dura mater), fluid spaces (subarachnoid space, subdural space), a fatty space (epidural space) and supporting ligaments (denticulate ligament), all housed in the vertebral bones; blood vessels excluded for simplicity.

categories and all include viscous dissipation. Half are non-porous models that have viscous fluids and largely linear viscoelastic solids, which support dispersive wave propagation (Bertram et al., 2005, 2008, Bertram, 2009, 2010). The rest are poroelastic models, which contain viscous pore fluid in a linear elastic matrix but whose boundary conditions preclude dispersion (Harris and Hardwidge, 2010; Støverud et al., 2011, 2016; Drøsdal et al., 2013). Three of the four 1w-FSI models are of an idealized spinal

Table 1
Theoretical continuum models of spinal biomechanics related to syringomyelia.

Reference	Physics	Maths	Solution	Dim	Geom	Fluids	Solids	Disp	Val	Notes
Lockey et al. (1975)	2w-FSI	Analyt	Bessel	2	Ideal	I	LE	N[a]	N	PSS: dura wave speed (dura thickness, SSS blockage)
Berkouk et al. (2003); Carpenter et al. (2003)			MoC	1	Ideal	I	LE	N	N	PSS: transmural pressure wave speed, pressure amplification (cross-sectional area ratio)
Elliott et al. (2009)			MoC	1^{∞}	Ideal	I	LE	N	Y[b]	Transmural pressure wave speed (Jackson and Williams, 1979; Greitz et al., 1999)
Cirovic (2009)			RF	2^{∞}	Ideal	I	LE	N	Y	Four wave speeds, used results from Bertram et al. (2005)
Cirovic and Kim (2012)			MoC	1	Ideal	I	LE	N	N	1D analytical model developed as computationally inexpensive alternative to a 2D numerical model, accuracy verified
Elliott (2012)			FDM/Quad	1^{∞}	Ideal	I	LPE-Darcy	N	Y[c]	As per Elliott et al. (2009)
Present Paper			HEV	2^{∞}	Ideal	I	LE	Y	Y	Wave speed (Williams, 1976; Kalata et al., 2009)
Bertram et al. (2005)		Num	FEM	2	Ideal	V	LE	Y	Y	Resonant frequency of end-to-end wave travel (Williams, 1976)
Bertram et al. (2008)			FEM	2	Ideal	V	LVE	Y	Y[d]	As per Bertram et al. (2005)
Bertram (2009)			FEM	2	Simple	V	LVE	Y	Y[e]	As per Bertram et al. (2005); pulse wave speed (Kalata et al., 2009)
Bertram (2010)			FEM	2	Simple	V	LVE	Y	Y	Pulse wave speed (Williams, 1976; Jackson and Williams, 1979; Greitz et al., 1999; Kalata et al., 2009), resonance (Williams, 1976)
Harris and Hardwidge (2010)			FEM	2	Ideal	$V^{(pore)}$	LPE-Darcy	N	N[f]	PSS: pore pressure and tissue stress (diffusion constant)
Støverud et al. (2011)			FEM	2	Ideal	V	LPE-Biot	N	N[g]	PSS: SC deformation, pore fluid velocity (homogeneous vs. heterogeneous SC permeability)
Drøsdal et al. (2013)			FEM	2	Ideal	V	LPE-Darcy	N	N[h]	PSS: longitudinal pressure profiles/fields (permeable cords with vs. without central canal)
Støverud et al. (2016)			FEM	3	Human	$V^{(pore)}$	LPE-Biot	N	N[i]	PSS: fluid pressure and velocity, SC displacement (elastic properties and permeabilities of SC tissues, presence vs. absence of anterior median fissure and pia mater)
Wang and Olbricht (2011)	1w-FSI	Analyt	CT	2^{∞}	Ideal[j]	V	–	N	N	PSS: PVS flow rate & pressure grad (PVS half amplitude, PVS hydraulic permeability)
Bilston et al. (2003)		Num	FVM	2	Ideal[j]	V	–	N	N	PSS: PVS flow rate & pressure grad, CC expansion (wave shape, speed, amplitude & length, syrinx press, PVS area)
Bilston et al. (2010)			FVM	2	Ideal[j]	V	–	N	N	PSS: net PVS flow into cord (Vascular-CSF phase, pia permeability)
Pahlavian et al. (2015b)			FVM	3	Human	V	–	N	N	PSS: pressure dissociation, integrated longitudinal impedance, peak velocities, duration of bidirectional flow, wall shear stress (static vs. dynamic geometry)
Gupta et al. (2008)	CFD	Analyt	Mathieu	3^{∞}	Ideal	V	–	–	N	Analytical model developed as computationally inexpensive alternative to a numerical model, accuracy verified
Berselli et al. (2014)			Fourier	2^{∞}	Ideal	V	–	–	N	Analytical model developed as computationally inexpensive alternative to a numerical model, accuracy verified
Loth et al. (2001)		Num	FDM	2^{∞}, 3^{∞}	Ideal	V	–	–	N[k]	PSS: velocity, pressure gradient and shear stress profiles (1D vs. 2D models); Reynolds, Womersley and Dean numbers in patient-specific SSS
Bilston et al. (2006)			FVM	2	Ideal	V	–	–	N	PSS: pressure field (obstruction permeability & porosity)
Stockman (2006)			LBM	3	Simple	V	–	–	N[l]	PSS: velocity profiles/fields (anatomical detail: empty SSS, progressively adding nerve bundles, trabeculae, denticulate ligament)
Stockman (2007)			LBM	3	Simple	V	–	–	Y[m]	Effective dispersion coefficient for oscillatory tube flow (Watson, 1983)
Roldan et al. (2009)			BEM	3	Human	V	–	–	N[n]	PSS: axial velocity fields at systole/diastole, pressure field at inlet and SSS outer surface at systole (normal vs. Chiari patient geometries)
Linge et al. (2010)			FVM	3	Simple	V	–	–	N[o]	Pressure and velocity fields during cardiac cycle in SSS and CSF spaces at the craniocervical junction
Cheng et al. (2012)			FVM-FEM	3	Human	V	–	–		MRI peak CSF velocity at C2 level over cardiac cycle

(continued on next page)

Table 1 *(continued)*

							Y^{p}	
Rutkowska et al. (2012)	FEM	3	Human	V	–	–	Y^{q}	PCMRI peak CSF velocities at five spinal levels
Yiallourou et al. (2012)	FVM-FEM	3	Human	V	–	–	Y^{r}	Validation study: 4D-PCMRI peak CSF velocities, visual interpretation of through-plane velocity profiles
Clarke et al. (2013)	FVM	3	Human	V	–	–	Y^{s}	PCMRI CSF velocity at 5 points at the C2 and C5 levels over the cardiac cycle
Støverud et al. (2013)	FEM	2	Ideal	V	–	–	N^{t}	PSS: velocity and pressure fields, dynamic pressure (SSS obstruction, steady vs. periodic flow)
Martin et al. (2013)	FVM	3	Human	V	–	–	N^{u}	PSS: geometric parameters and hydraulic metrics (healthy vs. pre- vs. post-decompression patients)
Helgeland et al. (2014)	DNS-FVM	3	Human	V	–	–	N^{v}	High spatial and temporal resolution solution of flow in a Chiari patient model
Pahlavian et al. (2014)	FVM	3	Human	V	–	–	Y^{w}	As per Yiallourou et al. (2012)
Pahlavian et al. (2015a)	FVM	3	Human	V	–	–	Y^{x}	Validation study: 4D-PCMRI peak CSF velocities, visual interpretation of through-plane velocity profiles
Martin et al. (2016)	FVM-FEM	3	Human	V	–	–	N	PSS: hydrodynamic and geometric parameters (model geometries segmented from MRI by different human operators)

Abbreviations: Physics: 2w-FSI = two-way fluid-structure interaction (FSI), 1w-FSI = one-way FSI (prescribed moving boundary), CFD = computational fluid dynamics (rigid solids); Maths: Analyt = analytical, Num = numerical; Solution: BEM = boundary element method, Bessel = Bessel functions, Fourier = Fourier analysis, CT = coordinate transformation, FDM = finite difference method, FEM = finite element method, FVM = finite volume method, LBM = Lattice Boltzmann method, MF = Mathieu functions; MoC = method of characteristics, Quad = quadrature, RF = root finding; Dim = spatial dimensions, ∞ = model infinitely long in axial dimension; Geom: Ideal = idealized, Simple = simplified anatomy, Human = human anatomy; Disp = dispersion; Fluids: I = inviscid, V = viscous, V(pore) = viscous pore fluid only, no separate fluid space; Solids: LE = linear elastic, LVE = linear viscoelastic, LPE-Darcy/Biot = linear poroelastic using Darcy's law/Biot's consolidation theory; Y = yes, N = no; Superscripts: a: Dispersion was modelled in an analysis of sound wave attenuation but in a rigid solid model; b: Distensibility calculated from animal data, validates models in Berkouk et al. (2003) and Carpenter et al. (2003), see text for explanation; c: Same validation as Elliott et al. (2009) at non-porous limit but poroelastic damping left as parametric sensitivity study only; d: Assumed that changing the tissue properties from linear elastic in Bertram et al. (2005) to linear viscoelastic would not affect the validation; e: Assumed that adding in a syrinx to the Bertram et al. (2008) model, which changed the pulse wave speed but within the range of human empirical measurements (Kalata et al., 2009), would not affect the original validation from Bertram et al. (2005); f: Only fluid is in the pores of the SC tissue as model does not include SSS, pressure load applied directly to SC surface as boundary condition; g: Cited qualitative comparison of CSF velocity patterns with PCMRI from Roldan et al. (2009), no parameter values specified; h: Stated that peak velocities were in a range for normal human subjects and some patients with Chiari malformation (Quigley et al., 2004; Hentschel et al., 2010; Rutkowska et al., 2012); i: Only fluid is in the pores of the SC tissues as model does not include SSS, CSF pressure wave prescribed as a boundary condition to the pia mater; j: Model of a spinal perivascular space only; k: Only qualitative agreement of CSF velocity profiles with PCMRI was possible because of the low resolution of MR images; l: Verified against steady and periodic analytical solutions, reproduced numerical solution by Loth et al. (2001); m: Verified against two analytical solutions (Aris, 1956, Watson, 1983), the solution in Watson (1983) was previously validated to within a factor of 1.2–2 of empirical data; n: Qualitative comparison of CSF velocity patterns with PCMRI; o: Qualitative agreement of CSF velocity profiles with PCMRI; p: Model driven by MRI-derived velocity measured at one location and validated against MRI velocity from a nearby location, PSS: obstruction permeability (pressure, velocity); q: Model driven by non-physiological (sinusoidal) flow with constant pressure-drop BCs; r: Model driven by MRI-derived velocity profile and validated against MRI velocity data, the agreement between CFD and 4D-PCMRI was not satisfactory but the analysis of the validation was precisely the focus of the study; s: Model driven by MRI-derived flow (Fourier reconstructed) measured at the hindbrain tonsil level and validated against MRI velocity data recorded at C2 and C5 locations; t: Analysis of Bernoulli vs. Navier-Stokes predictions in the SSS with various degrees of obstruction; u: Model driven by MRI-derived flow measured at C2 level, validation not possible because MRI was not performed at any other location; v: Velocity BC generated to reproduce peak velocity amplitudes of a series of patient PCMRI data; w: Models with nerve roots and denticulate ligaments were evaluated for their difference with the validated models from Yiallourou et al. (2012) that did not contain these structures; x: Continuation of the CFD–PCMRI validation study by Yiallourou et al. (2012) but with similar models to Pahlavian et al. (2014), which include nerve roots and denticulate ligaments.

perivascular space (PVS), rather than of the greater contents of the spinal canal. Prescribed PVS wall motion and/or the phasing of the vascular and CSF pressure pulses is used to drive the perivascular flow from the SSS into the SC tissue spaces.

Much of the value of a mathematical model lies in its ability to make predictions about situations that cannot be observed and/or measured in the physical system being modelled. However, the extent to which such predictions are representative of the system in question depends on how well the model can be validated. Of the 37 spinal models that appear in Table 1, 15 were validated (40%). Although this number may seem low, it is largely explained by the dearth of human empirical data as a consequence of ethical considerations and the practical difficulties of measuring small and isolated locations without disturbing the operating conditions of the living system. The same could be said of many, if not most, biomechanical models. Notwithstanding, some of the spinal models in Table 1 are intentionally purely theoretical or numerical and their lack of validation does not diminish their contribution to the understanding of spinal mechanics.

Next we focus on the themes of poroelasticity, dispersion and validation to elucidate areas that demand attention in the modelling of syringomyelia.

1.2.2. Poroelasticity

The poroelastic modelling of the SC tissues has lagged behind simple elastic approaches. Nonetheless, with a sufficient understanding of the basic FSI behaviour now established, several investigators have tackled the poroelastic problem.

Harris and Hardwidge (2010) applied a transient uniform pressure load to the surface of an axisymmetric SC section with and without a syrinx present. The pressure of the pore fluid was determined by Darcy's law (which ignores the effects of the motion of the solid phase relative to the fluid phase and assumes that the porosity remains constant), which was coupled with the linear elasticity equations through a stress–pressure equation. They found that the larger the diffusion constant, the quicker the pressure changes propagated through the SC; if the diffusion constant was sufficiently small, though, then the peak pore pressure did not reach the applied pressure load. Furthermore, the removal of the pressure load was followed by the generation of a transient tensile stress in the SC tissue, which was greater when the syrinx was present thus favouring syrinx expansion. In Støverud et al.'s (2011) model, in addition to a poroelastic cord they included the CSF-filled SSS. Poroelasticity was modelled using Biot's consolidation theory, which is derived from linear elasticity, the Navier–Stokes equations and Darcy's law. The pressure load on the SC was imparted by a longitudinal pressure gradient driving a steady flow through the surrounding SSS. When the SC contained no fluid-filled cavity, the CSF was drawn into the SC region where the SSS pressure was relatively high, with concomitant compression of the SC, and ejected out further downstream where the SSS pressure was lower, causing the SC to become distended. The distended SC had expanded pores, producing the appearance of oedema. It would appear that the CSF influx was due to a pressure gradient set up by the SC pore pressure being lower than the SSS pressure upstream, and vice versa downstream. These findings applied to a SC of uniform permeability and to one of heterogeneous and anisotropic permeability that distinguished the white and grey matter. When a fluid-filled cavity was included in the SC (denoted as the central canal but could equally represent an elongated syrinx), there was preferential flow along this cavity and diminished flow back into the SSS. Drøsdal et al. (2013) extended the above modelling to periodic CSF flow. The findings were equivalent when there was a fluid-filled cavity in the SC. For the patent SC, however, there was no radial pressure gradient in the SC nor fluid exchange between the SC and SSS. This may have been because of the poroelastic treatment being Darcy's law rather than the more complete Biot theory, or simply the porous flow not being able to keep pace with the periodic CSF flow in the SSS.

The poroelastic models in Table 1 that treat wave propagation are those by Elliott (2012) and Støverud et al. (2016). The former was an analytical coaxial tubes model. The elasticity of the SC was described by the pressure–area relation of a thin-walled tube, nominally being the pia mater. Fluid transport across the pia mater and within the SC was modelled with Darcy's law. An explicit expression was derived for the timescale over which viscous and inertial forces compete, which predicts that dilated PVS, SSS flow obstructions, and a stiffer and thicker pial membrane, all associated with syringomyelia, will increase transpial flux and retard wave travel. It was also revealed that poroelastic damping of spinal pulse waves is anisotropic; greater tissue permeability in the radial direction, such as through the PVS traversing the pia mater, and reduced permeability in the axial direction, such as through the interstitial spaces along nerve fibres, will damp the axial-travelling pulse wave. Støverud et al. (2016) investigated some of these predictions in an anatomically detailed 3D model of an isolated SC segment. The wave was implemented as a travelling pressure boundary condition on the surface of the fluid-saturated SC; thus the boundary condition was 1w-FSI but the mechanics within the SC tissue were 2w-FSI. Eleven models were created from permutations of three geometries (grey matter, white matter, central canal; anterior median fissure removed; grey and white matter combined and pia mater included) and variations in elastic and poroelastic properties. As in Støverud et al. (2011) and Drøsdal et al. (2013), the pressure gradients were smaller within the fluid-filled cavity (central canal/syrinx) than in the surrounding tissue. The pressure wave spread faster in the radial direction in the model with a stiff pia mater than in the other poroelastic models. The stiffness and permeability of the pia mater, however, were not investigated separately so the underlying mechanism is unclear. Decreasing the Poisson's ratio (ν) from 0.479 to 0.4 changed the displacement field in the linear elastic model and the maximum displacement shifted from the centre to the boundary of the SC. In the poroelastic model, though, this reduction in ν only had a minor effect. Notwithstanding, only a small range of ν was modelled. Making the permeability of the white matter anisotropic made little difference to the modelling predictions, although only one permeability tensor was trialled. A feature of the poroelastic results was the presence of a pressure gradient in the boundary layer adjacent the pia membrane. The results appear to be consistent with those briefly reported in a pair of conference abstracts by Bertram et al. (2014) and Bertram and Heil (2015). The elastic cord and pia in the 2w-FSI model presented in Bertram (2010) were made poroelastic to examine if the cyclic pressure gradients set up by an obstruction juxtaposed with an underlying syrinx would drive a net flux of CSF into the syrinx. Most of the CSF that entered the SC remained there, producing a cyclic swelling in a tissue boundary layer; very little

of this CSF made it to the syrinx or back out into the SSS. This progressive oedema was diminished by the absence of the syrinx or by the presence of the pia mater, the stiffness of which limited SC deformation.

As noted in Table 1, though, most of the spinal canal models are not poroelastic, which means that poroelasticity is being approximated by an elastic solid(s). The question then arises, what are the most appropriate values for the elastic constants? The Young's modulus can be determined from the wave speed and the Poisson's ratio has typically assumed to be near the incompressible limit of $\nu = 0.5$ (Støverud et al. (2016): 0.4, 0.479; Lockey et al. (1975): 0.48; Bertram and colleagues (Bertram et al., 2005, 2008, Bertram, 2009, 2010); Harris and Hardwidge (2010): 0.49; Cirovic (2009): 0.5).[2] However, although the three phases of the SC—cellular tissue matrix, interstitial fluid and blood—are each almost perfectly incompressible because of their water content, it is likely that localised changes in porosity resulting from fluid displacement may yield an effective compressibility; i.e., an effective $\nu < 0.5$ in the elastic approximation. This was borne out in a previous study based on a lumped-parameter model (Elliott et al., 2011). Moreover, Bilston and Thibault (1996) noted in their experiments on human SCs that the production of a small volume of white fluid associated with tensile failure at high strain rates may have resulted in a change in the effective ν. Furthermore, Fischbein et al. (1999, 2000) have reported clinical cases of fluid accumulation in the SC without the formation of a syrinx, i.e., oedema, which resolved after the associated CSF flow obstruction was removed. This so-called “pre-syrinx” state would likely involve a change in SC porosity hence a change in effective ν. Therefore, when approximating the poroelastic SC as a simple elastic material, the appropriate Poisson's ratio may be somewhat less than the incompressible limit that has previously been assumed.

1.2.3. Dispersion

Dispersion in a cylindrical waveguide is caused by the geometrical interface and boundary conditions. Of all the previous mathematical models relevant to syringomyelia, only the 2D finite element 2w-FSI models of Bertram and colleagues permit wave dispersion (Bertram et al., 2005, 2008, Bertram, 2009, 2010). In their 2005 paper, they presented the propagation of a triangular wave pulse in which its dispersive nature was recognised (Fig. 5(b) therein). This model included fluid viscosity and subsequent versions also included solid viscoelasticity, although this made it more difficult to distinguish between dispersion and damping effects.

Syringomyelia progresses over months to years, either as a congenital malformation or following spinal trauma (Brodbelt and Stoodley, 2003; Milhorat et al., 1999; Sakushima et al., 2012). In contrast, mechanical disturbances of the cerebrospinal system are largely driven by percussive and cardiac pressure sources operating over fractions of a second up to several seconds, respectively. This suggests that the role of biomechanical phenomena in syrinx formation and expansion may be a gradual accumulation of very small effects, rather than the effect of an isolated critical event. Therefore, a dispersion analysis is warranted that captures the FSI over multiple timescales.

1.2.4. Validation

In the case of 2w-FSI models, the standard validation approach is to match the speed of the dominant travelling pressure wave with that measured in vivo to ensure that the dynamic compliance is realistic even with the geometrical simplifications. There have been just two documented sets of CSF pulse wave measurements in humans: the invasive measurements of Williams in 1972 using pressure transducers connected to lumbar puncture needles (Williams, 1972, 1976; Jackson and Williams, 1979), and the non-invasive MRI measurements of Kalata et al. (2009).[3] There are still no equivalent measurements for the PVS to validate the 1w-FSI models. A rigid CFD model does not support wave propagation thus the validation approach is different. Instead, having set the end conditions from MRI-derived velocity profiles, the numerically predicted velocity profiles/peak velocities at one or more intermediate locations are compared to additional MRI measurements.

In the first (2w-FSI) model of CSF pulse waves, Lockey et al. (1975) performed a parametric sensitivity study predicting the influence of dura thickness and SSS blockage on the dura wave speed; the “information on the elastic constants for living or dead dura [were] not available” for validation. A similar approach was employed by Carpenter and colleagues (Carpenter et al., 1999, 2003; Berkouk et al., 2003). In their default configuration they specified the SC distensibility to reproduce the wave speed from the aforementioned in vivo measurements, and then studied the sensitivity of the wave speed and transmural pressure on the cross-sectional area ratio of the fluid and solid components. It was not until Ozawa et al.'s (2004) experiments on rabbit SCs that an empirical estimate could be made of human SC distensibility. The work of Carpenter and colleagues was later re-evaluated with these animal data at hand. Elliott et al. (2009) derived the static compliance (from tube distensibility) independently from the dynamic compliance (from wave speed) and was thus able to retrospectively validate the 1D coaxial tubes model, albeit with revised geometry and implications. The first in a series of numerical models by Bertram et al. (2005) was validated against Williams's measurements of the frequency of end-to-end wave travel in the spinal canal (Williams, 1976); i.e., an alternative measure of dynamic compliance. The speeds of the four predicted waves were subsequently used by Cirovic (2009) to validate an analytical model. In later models by Bertram (2009, 2010), when the incremental refinements were non-trivial, the predicted wave speed values were also compared with empirical measurements, re-establishing the validation.

[2] Although Poisson's ratio is a 2D quantity, Cirovic and Kim (2012) demonstrated strong agreement between the wave speeds predicted by a 1D (analytical) model and a 2D (numerical) model with SC tissue having “near impressibility”. We may thus consider the 1D models of Carpenter and colleagues (Berkouk et al., 2003; Carpenter et al., 2003) and Elliott and colleagues (Elliott et al., 2009; Elliott, 2012) as having $\nu \approx 0.5$.

[3] In Greitz et al.'s (1999) paper on MRI measurements of CSF velocity and CSF stroke volume, they mention the “speed of the volume conduction in the spinal canal (CSF pulse and pressure wave) is approximately 4m/s” in their proposal of a hydrodynamic theory of cystic cord lesions. The source of this wave speed value is not explained.

In the previously mentioned poroelastic models that support wave propagation (Section 1.2.2: Elliott, 2012; Stoverud et al., 2016), the values of SC elastic moduli, porosity and permeabilities were estimated from human brain measurements and animal studies. Validation was limited to the dynamic compliance—no experiments have been published to validate the poroelastic behaviour of the SC.

One-way FSI models have been used to demonstrate two possible mechanisms for pumping CSF from the SSS–up a pressure gradient–and into the spinal cord via the PVS (Bilston et al., 2003, 2010; Wang and Olbricht, 2011). One of these perivascular pumps involves a phase difference between the arrival of the arterial and CSF pulses in the PVSs. By exploring the full range of phase differences, Bilston's group were able to show that the PVS could act as a dynamic one-way valve; when a CSF driving pressure gradient coincided with a deflated artery, fluid would be forced into the cord, but when the CSF pressure gradient reversed, the inflated artery would constrict the surrounding PVS, hindering the egress of fluid by greater flow resistance (this was maximal for a phase difference of 0.4 s for a pulse rate of 60 bpm). Although their predictions were purely numerical and the model omitted most of the spinal canal, they provided the foundation for investigating the physiological requirements, likelihood and implications of this fluid pump. Elliott et al. (2010) developed a lumped-parameter model of a closed cerebrospinal system, also unvalidated, which supports this pumping mechanism in principle with the caveat that there must be enough displaceable venous volume to accommodate the accumulated spinal fluid. Martin et al. (2012) went on to produce a coupled hydrodynamic tree model of the cardiovascular and cerebrospinal fluid systems that predicted the delay between the arrival of adjacent SC blood pulsations and CSF pulsations in the SSS and then computed the perivascular flow into/out of the SC from Bilston et al. (2010) phase delay relation. The phase lag was found to vary to a great degree along the SC depending on craniospinal compliance and vascular anatomy. Martin et al.'s model was built from and validated against human patient data (MRI-measured flow rates of CSF in the SSS at the upper neck region and cerebral blood flow). These three models serve to demonstrate the fundamental role of theoretical modelling, even before validation data is available, in the development of predictions with physiological relevance.

In anatomically realistic CFD models of spinal CSF flow, the 3D geometry and the velocity boundary condition that drives the flow are derived from human MRI. The ideal way of validating such a model would be to compare the predicted pressure field with in vivo measurements, thereby ensuring the pressure-flow relation is satisfied. However, such CSF pressure measurements are currently not possible. Modern ethical protocols do not permit invasive human measurements such as those performed by Williams (Williams, 1972, 1976, Jackson and Williams, 1979), and no techniques have been developed yet for noninvasively measuring CSF pressure. Therefore, and somewhat less satisfying, CFD models are validated against secondary MRI velocity measurements (field or peak value) at one or more locations distant from the boundary condition that already reproduces the MRI velocity conditions. This MRI validation procedure was recently evaluated in detail by Martin and colleagues. Yiallourou et al. (2012) found that their CFD model, driven by 4D PCMRI velocity data, consistently underpredicted the peak CSF velocities (by up to a factor of 4) in other regions of the spinal canal measured by the same MRI. A pair of follow-up studies determined that including ligaments and nerve roots in the static CFD model is not sufficient to reproduce the MRI velocities (which were still 1.4–1.6 times greater than CFD predictions; Pahlavian et al., 2015a), but that even a small amount of prescribed tissue motion (150–300 μm; 1w-FSI) can significantly augment the predicted pressure drops (120%) and peak velocities (60%) in the CSF flow (Pahlavian et al., 2015b). In other words, the role of FSI is significant in cerebrospinal fluid mechanics.

There are, however, theoretical problems in the spinal canal for which a rigid CFD model is particularly well suited. For example, Gupta et al. (2008) and Berselli et al. (2014) derived analytical solutions to pulsatile viscous flow in a straight elliptic annulus and used this to verify an equivalent numerical model. Another example is Støverud et al.'s (2013) analysis of the hypothesis that the pressure of CSF flow past an obstruction of the SSS will follow Bernoulli's principle, with the lower pressure across the reduced cross section causing the SC to expand, thereby accumulating fluid to form a syrinx (Greitz et al., 1999). For a physiological periodic flow, the unsteady viscous and inertial forces were non-negligible so the flow did not follow Bernoulli's principle. These results are fundamental and do not require empirical comparison.

In summary, the validation method depends on the type of model (FSI/CFD), CFD validation has shown that FSI is significant, even when modelling bulk CSF flow (as opposed to wave propagation), and the lack of validation data is not a limiting factor as fundamental contributions are possible from purely theoretical modelling.

1.3. Present approach

Experiments and clinical observations on human spinal cords demonstrate that it exhibits an effective compressibility, likely a result of localised changes in fluid displacement and porosity caused by tissue stress. Also, the contrast between the short timescales of mechanical disturbances and the long timescales of syrinx progression demands an analysis that captures the FSI over multiple timescales. Therefore, in the present paper, we seek to understand the wave propagation characteristics of the spinal canal over the whole frequency spectrum and its sensitivity to the compressibility of the cord material at different stages of syrinx progression. It is desirable to obtain this information explicitly, with minimal computational effort, and the numerical model should be verified and be validated to the extent possible.

To achieve these aims, we approximate the fluid-saturated poroelastic SC material as a simple linear elastic medium but vary Poisson's ratio from nearly perfectly incompressible ($\nu = 0.49$) down to half that value (0.25). We formulate the model as a system of Helmholtz equations describing axisymmetric harmonic motion of the cylindrical layers. These equations are discretised using Chebyshev polynomials and then solved as a generalised eigenvalue problem. This linear algebra approach was devised by Adamou and Craster (2004) as an alternative to root finding for the modelling of generic elastic wave guides. Karpfinger et al. (2008a, 2008b, 2010), later applied this method to geophysical borehole analysis, which involves very stiff materials (rock) being excited in the

megahertz frequency spectrum; the variation of seismic wave speed indicates the rocks' physical characteristics, including porosity, which is useful for hydrocarbon exploration. We explicitly determine the dispersion diagram and the displacement and stress mode shapes for the spinal canal, which involves soft materials being excited in the hertz-to-kilohertz spectrum, and analyse their features. We verify our numerical code by reproducing the dispersion diagram for a semi-infinite cylindrical elastic bar found by root finding, and validate our model's dynamic compliance with published measurements of the speed of CSF pulse waves in humans.

In this paper we make two contributions: (i) a study of the FSI of an elastic waveguide and, using the knowledge so-gained, (ii) a deeper understanding of the pathogenesis of post-traumatic syringomyelia. After deriving the governing equations and describing the details of the numerical implementation (Section 2), we present the verification of the numerical code, assess its accuracy and provide a broad validation of the waveguide model (Section 3.1). Next, we present an eigen-analysis of the waveguide, which includes the dispersion diagrams and plots of the displacement and stress mode shapes (Section 3.2). Up to this point the results have broad applicability to natural and engineered systems. Following on, the focus shifts to simulating the state-by-state progression of post-traumatic syringomyelia, where we characterise the pathogenesis in mechanistic terms (Section 3.3).

2. Methods

Fig. 1(a,b) shows the two cross-sectional models of the spinal canal. The 'healthy' model consists of an elastic cylinder, representing the SC tissue with the attached pia mater, surrounded by an annulus of inviscid fluid, representing CSF in the spinal subarachnoid space (SSS), with a rigid boundary corresponding to the dura mater; the 'diseased' model includes a central cylinder of inviscid fluid that represents a syrinx. We follow the approach of Adamou and Craster (2004) and Karpfinger et al. (2008b) for the derivation of the governing equations and their numerical solution, which is briefly described here.

2.1. Governing equations

The propagation of axisymmetric time-harmonic waves through a semi-infinite cylindrically layered structure are given by

$$\mathbf{u}(r,\, z,\, t) = U(r)e^{i(k_z z-\omega t)}, \tag{1}$$

where $\mathbf{u}$ is the material displacement, r is the radial coordinate, z is the axial coordinate, t is time, U is the displacement amplitude function, k_z is the axial wavenumber and ω is the angular frequency.

2.1.1. Inviscid fluid layers

The linearised Navier-Stokes equation is

$$-\nabla p = \rho_{\mathrm{f}}\ddot{\mathbf{u}}, \tag{2}$$

where p, ρ_{f} and $\ddot{\mathbf{u}}$ are the fluid pressure, density and acceleration, respectively. Expressing the pressure in terms of the fluid displacement,

$$p = -K_{\mathrm{f}}\nabla\cdot\mathbf{u}, \tag{3}$$

where K_{f} is the fluid bulk modulus, and the fluid velocity in terms of a scalar potential, $\widetilde{\varphi}$,

$$\dot{\mathbf{u}} = \nabla\widetilde{\varphi}, \tag{4}$$

leads to the wave equation

$$\nabla^2\widetilde{\varphi} = \frac{1}{c_{\mathrm{f}}^2}\ddot{\widetilde{\varphi}}, \tag{5}$$

where the speed of sound in the fluid is given by

$$c_{\mathrm{f}} = \sqrt{\frac{K_{\mathrm{f}}}{\rho_{\mathrm{f}}}}. \tag{6}$$

The potential $\widetilde{\varphi}$ takes the same separable form as the displacement in (1),

$$\widetilde{\varphi}(r,\, z,\, t) = \widetilde{\Phi}_{\mathrm{f}}(r)e^{i(k_z z-\omega t)}, \tag{7}$$

which reduces (5) into a Helmholtz ordinary differential equation,

$$\underbrace{\left(\frac{\mathrm{d}^2}{\mathrm{d}r^2} + \frac{1}{r}\frac{\mathrm{d}}{\mathrm{d}r} + \frac{\omega^2}{c_{\mathrm{f}}^2}\right)}_{\mathfrak{L}_{\mathrm{f}}}\Phi_{\mathrm{f}} = k_z^2\Phi_{\mathrm{f}}, \tag{8}$$

where $\Phi_{\mathrm{f}} = \widetilde{\Phi}_{\mathrm{f}}/(-i\omega)$.

2.1.2. Elastic solid layers

From linear elasticity theory, the momentum equation is

$$\nabla\cdot\boldsymbol{\sigma} = \rho\ddot{\mathbf{u}}, \tag{9}$$

where $\boldsymbol{\sigma}$, ρ and $\ddot{\mathbf{u}}$ are the stress tensor, density and acceleration of the solid, respectively. For isotropy

$$\boldsymbol{\sigma} = \lambda(\nabla\cdot\mathbf{u})\mathbf{I} + \mu(\mathbf{u}\nabla + \nabla\mathbf{u}), \tag{10}$$

and λ and μ are Lamé's first parameter and the shear modulus, respectively.

The displacement may be decomposed into a scalar potential, $\boldsymbol{\varphi}$, and a vector potential, $\boldsymbol{\psi}$, as follows

$$\mathbf{u} = \nabla\varphi + \nabla\times\boldsymbol{\psi}, \tag{11a}$$

$$\nabla\cdot\boldsymbol{\psi} = 0, \tag{11b}$$

which satisfies (9) if these potentials obey their respective wave equations,

$$\nabla^2\varphi = \frac{1}{c_{s1}^2}\ddot{\varphi}, \tag{12a}$$

$$\nabla^2\boldsymbol{\psi} = \frac{1}{c_{s2}^2}\ddot{\boldsymbol{\psi}}, \tag{12b}$$

where

$$c_{s1} = \sqrt{\frac{\lambda+2\mu}{\rho_s}}, \tag{13a}$$

$$c_{s2} = \sqrt{\frac{\mu}{\rho_s}}, \tag{13b}$$

correspond to the speeds of dilatational (s1) and shear (s2) waves in an infinite elastic medium. For axisymmetric motion $\boldsymbol{\psi} = \{0, \psi_\theta, 0\}$, so we denote $\psi = \psi_\theta$. By expressing the pair of scalar potentials in harmonic form,

$$\varphi = \Phi_s(r)e^{i(k_z z-\omega t)}, \tag{14a}$$

$$\psi = \Psi_s(r)e^{i(k_z z-\omega t)}, \tag{14b}$$

the wave equations (12a,b) become a pair of Helmholtz equations

$$\underbrace{\left(\frac{\mathrm{d}^2}{\mathrm{d}r^2} + \frac{1}{r}\frac{\mathrm{d}}{\mathrm{d}r} + \frac{\omega^2}{c_{s1}^2}\right)}_{\mathfrak{L}_{s1}}\Phi_s = k_z^2\Phi_s, \tag{15a}$$

$$\underbrace{\left(\frac{\mathrm{d}^2}{\mathrm{d}r^2} + \frac{1}{r}\frac{\mathrm{d}}{\mathrm{d}r} - \frac{1}{r^2} + \frac{\omega^2}{c_{s2}^2}\right)}_{\mathfrak{L}_{s2}}\Psi_s = k_z^2\Psi_s. \tag{15b}$$

2.2. Boundary conditions

The interface boundaries between adjacent layers demand continuity of displacement and stress. Between a fluid layer and a solid layer,

$$u_r|_s = u_r|_f, \tag{16a}$$

$$\sigma_{rr}|_s = -p|_f, \tag{16b}$$

$$\sigma_{rz}|_s = 0. \tag{16c}$$

Likewise, we require boundary conditions at the outer surface of our cylindrically layered structure. For an elastic solid cord in vacuo the stress-free condition is

$$\sigma_{rr} = \sigma_{rz} = 0, \tag{17a,b}$$

while for the rigid dura boundary of a fluid-filled SSS the boundary condition is simply

$$u_r = 0. \tag{18}$$

The expressions for displacement, pressure and stress are now given.

2.2.1. Inviscid fluid layers

Substituting (7) and (8) into (4), and noting $\partial/\partial t = -i\omega$ for our harmonic system (7), we arrive at the respective radial and axial displacement components,

$$u_r = \frac{\mathrm{d}\Phi_\mathrm{f}}{\mathrm{d}r}, \tag{19a}$$

$$\breve{u}_z = -\left(\frac{\mathrm{d}^2}{\mathrm{d}r^2} + \frac{1}{r}\frac{\mathrm{d}}{\mathrm{d}r} + \frac{\omega^2}{c_\mathrm{f}^2}\right)\Phi_\mathrm{f}, \tag{19b}$$

where $\breve{u}_z = ik_z u_z$. Similarly the pressure may be obtained by substituting (3), (4), (6) and (7) into (2),

$$p = \omega^2 \rho_\mathrm{f} \Phi_\mathrm{f}. \tag{20}$$

2.2.2. Elastic Solid Layers

Substituting (14a,b) into (11a) gives the radial and axial displacements,

$$u_r = \frac{\mathrm{d}\Phi_\mathrm{s}}{\mathrm{d}r} - \breve{\Psi}_\mathrm{s}, \tag{21a}$$

$$\breve{u}_z = -\left(\frac{\mathrm{d}^2}{\mathrm{d}r^2} + \frac{1}{r}\frac{\mathrm{d}}{\mathrm{d}r} + \frac{\omega^2}{c_{\mathrm{s}1}^2}\right)\Phi_\mathrm{s} + \left(\frac{\mathrm{d}}{\mathrm{d}r} + \frac{1}{r}\right)\breve{\Psi}_\mathrm{s}. \tag{21b}$$

Likewise, substituting (11a) and (14a,b) into (10) gives the normal and shear stress,

$$\sigma_{rr} = \left(2\mu\frac{\mathrm{d}^2}{\mathrm{d}r^2} - \lambda\frac{\omega^2}{c_{\mathrm{s}1}^2}\right)\Phi_\mathrm{s} - 2\mu\frac{\mathrm{d}\breve{\Psi}_\mathrm{s}}{\mathrm{d}r}, \tag{22a}$$

$$\breve{\sigma}_{rz} = -2\mu\left(\frac{\mathrm{d}^3}{\mathrm{d}r^3} + \frac{1}{r}\frac{\mathrm{d}^2}{\mathrm{d}r^2} - \frac{1}{r^2}\frac{\mathrm{d}}{\mathrm{d}r} + \frac{\omega^2}{c_{\mathrm{s}1}^2}\frac{\mathrm{d}}{\mathrm{d}r}\right)\Phi_\mathrm{s} + \mu\left(2\frac{\mathrm{d}^2}{\mathrm{d}r^2} + \frac{2}{r}\frac{\mathrm{d}}{\mathrm{d}r} - \frac{2}{r^2} + \frac{\omega^2}{c_{\mathrm{s}2}^2}\right)\breve{\Psi}_\mathrm{s}; \tag{22b}$$

$\breve{\Psi}_\mathrm{s} = ik_z\Psi_\mathrm{s}$ and $\breve{\sigma}_{rz} = ik_z\sigma_{rz}$.

2.3. Numerical solution

An n^{th}-order derivative operating over a finite interval, in our case a radial thickness, can be approximated at N interpolation points using Chebyshev polynomials; i.e., $D_N^{(n)} \approx d^n/dr^n$ (Weideman and Reddy, 2000). Using these differentiation matrices we can form discrete approximations to the differential operators $\mathfrak{L}_\mathrm{f}$, $\mathfrak{L}_{\mathrm{s}1}$ and $\mathfrak{L}_{\mathrm{s}2}$ in (8), respectively. E.g., the fluid operator becomes

$$L_\mathrm{f} = D_N^{(2)} + \mathrm{diag}(1/R_N)D_N^{(1)} + \mathrm{diag}(\omega^2/c_\mathrm{f}^2) \approx \mathfrak{L}_\mathrm{f}, \tag{23a,b}$$

where $R_N \approx r$ is the vector of radial interpolation points. For the two-layered case of an elastic cylinder (SC) surrounded by an annulus of fluid (SSS), the set of Helmholtz equations may be expressed as

$$L\Theta = k_z^2\Theta, \tag{24}$$

where

$$L = \begin{bmatrix} L_{\mathrm{s}1} & 0 & 0 \\ 0 & L_{\mathrm{s}2} & 0 \\ 0 & 0 & L_\mathrm{f} \end{bmatrix}, \quad \Theta = \begin{Bmatrix} x_{\mathrm{s}1} \\ \breve{x}_{\mathrm{s}2} \\ x_\mathrm{f} \end{Bmatrix} \tag{25a,b}$$

and $x_{\mathrm{s}1} \approx \Phi_{\mathrm{s}1}$, $\breve{x}_{\mathrm{s}2} \approx \breve{\Psi}_{\mathrm{s}2}$ and $x_\mathrm{f} \approx \Phi_\mathrm{f}$ are the discrete approximations of the displacement potential amplitudes. In arriving at the above definition of vector Θ, Eq. (15b) has been multiplied by ik_z, hence $\breve{x}_{\mathrm{s}2}$, to implement the boundary conditions for the solid layer (21a,b; 22a,b), as follows.

Using a similar approach, the matrices for the displacement (T) and stress (S) differential operators may be deduced. To incorporate the boundary conditions into (24), the rows of L corresponding to the interfaces and outer surface are substituted for differences of the respective rows of T and S, giving the modified matrix $\overline{L}$. By zeroing out the same rows of an identity matrix of the same dimension, M, the boundary value problem can be written as

$$\overline{L}\Theta = k_z^2 M\Theta. \tag{26}$$

For this generalised eigenvalue problem the phase velocities are given by the eigenvalues,

$$c = \frac{\omega}{\Re e(k_z)}, \tag{27}$$

and the displacement and stress mode shapes are given by the eigenvectors. The axial displacement and shear stress are recovered by dividing $\breve{u}_z$ and $\breve{\sigma}_{rz}$ through by ik_z. The matrix M is not of full rank thus (26) could be recast as an ordinary eigenvalue problem, although this extra step does not improve the accuracy of the harmonic time-asymptotic response.

The solution to Eq. (26) describes the harmonic response of a cylindrically layered fluid–solid waveguide to an arbitrary perturbation. The mode shapes have characteristic propagation speeds, given by their associated eigenvalues, but they do not contain magnitude information; i.e., the eigenvectors are an intrinsic property of the waveguide, rather than the solution to an initial-value problem, although such a solution can be constructed by the weighted sum of the eigenvectors. For this reason the mode shapes presented will be normalized by their wavelength-specific maxima of displacement and stress.

We developed a C++ code to compute the solution using the `boost` C++ numerical libraries (Boost, 2008) and the LAPACK Fortran subroutine `dggevx` (Anderson et al., 1999). No balancing was used in the latter subroutine because it produced additional numerical error.

2.4. Non-dimensional framework and associated physiological parameters for the spinal system

To present the dispersion behaviour of the fluid–solid waveguide in general form, we must non-dimensionalize the variables. In the canonical case, a semi-infinite cylindrical elastic bar, the only material property required to produce the dispersion diagram is the Poisson's ratio. The phase speed (c) can be non-dimensionalized by the speed of *bar waves*, $c_{\text{bar}} = \sqrt{E/\rho_s}$ (Love, 1927, p. 287), which are infinitely long, longitudinal, compression waves. The wavelength can be non-dimensionalized by the cylinder radius (R), giving a non-dimensional wavenumber R/Λ. When additional fluid/solid layers are included in the waveguide, the mass ratios and elasticity ratios become important. Notwithstanding, in this study the densities of all layers are equal and the elasticity of the solid cylinder is fixed. Therefore, we present all dispersion diagrams as c/c_{bar} versus R/Λ without any loss of generality.

The fluid, representing the CSF in the subarachnoid space and also the fluid in a syrinx, has been assigned the density, ρ_f=1000 kg/m^3, and bulk modulus, K_f=2.3 GPa, of water in accordance with physical measurements (Kiernan, 1998). The solid corresponds to the combined SC parenchyma and pial membrane surrounding it. Tissue is largely water by mass hence the density value ρ_s=1000 kg/m^3; i.e., equal to ρ_f. For the elastic properties of spinal tissues it is more convenient to work from the Young's modulus, E, and the Poisson's ratio, ν; i.e.,

$$\lambda = \frac{E\nu}{(1+\nu)(1-2\nu)}, \tag{28a}$$

$$\mu = \frac{E}{2(1+\nu)}. \tag{28b}$$

The value of Young's modulus, E=15 kPa, is taken from Ozawa et al.'s (2004) measurements of rabbit spinal cords with attached pia mater (with the pia removed the SC tissue had a Young's modulus of 5 ± 2 kPa, from which they deduced the Young's modulus of pia mater to be 2.3 MPa). For Poisson's ratio, in the eigen-analysis of the elastic waveguide (Section 3.2) we choose a default value of $\nu = 0.49$ for an almost perfectly incompressible material to allow comparison with the other published 2w-FSI models; this value is then subject to a parametric sensitivity study (Section 3.2.3), spanning the range 0.25–0.49. The subsequent investigations that apply these general results to analyse the pathogenesis of post-traumatic syringomyelia (Section 3.3) will use a baseline value of 0.25, to permit an effective compressibility that mimics the localised effect of interstitial fluid displacement in a poroelastic cord material, and reach 0.49 for the case of fully compressed SC tissue, mimicking the situation of collapsed fluid pores. The cross-sectional dimensions of the SC, R=4 mm, and dura, r_{dura}=7.5 mm, are taken from Elliott et al. (2009). The default radius of the syrinx, r_{syrinx}=2 mm, is simply chosen to be half that of the SC, but this parameter value will also be varied in a sensitivity study and again, along with r_{dura}, in an analysis of post-traumatic syrinx development (Section 3.3). These physiological parameter values are listed in Table 2.

3. Results and discussion

3.1. Verification and accuracy of the numerical code and general validation of the waveguide model

3.1.1. Verification

We verified the C++ code by reproducing the dispersion diagram for a semi-infinite cylindrical elastic bar from Davies (1948, Fig. 13), which comprises the first three modes to the Pochhammer and Chree equations solved via root finding. As our code solves the dimensional problem, we need to specify the elastic and geometrical properties of the semi-infinite cylinder. The Poisson's ratio must be the same value used by Davies, $\nu = 0.29$. We select the remaining parameter values from our default SC material (E=15 kPa, ρ_s = 1000 kg/m^3, R=4 mm), although their choice is arbitrary (Karpfinger et al., 2008b specified a steel cylinder: λ = 5.34562 GPa, G=3.872 GPa, ρ = 5000 kg/m^3, R=1 m). The numerical formulation defines cylindrical layers that each must have an inner radius, so to approximate a cylinder we set a value of R/1000 (4 μm). This numerical inner surface of the solid cylinder does not require a physical boundary condition (i.e., the relevant rows in matrix L remain unaltered and no zero is substituted in the diagonal of matrix

M; see Section 2.3). We apply a zero-stress boundary condition to the outer surface (17a,b;22a,b) and we set N=50 points for the Chebyshev polynomial (Section 2.3).

The dispersion diagram is shown in Fig. 3. The first three modes from Davies's (1948) calculations are plotted as solid lines and the first thirteen modes from the present model are plotted with circle markers. At long wavelengths ($R/\Lambda \to 0$), only mode I (labelled) is propagatory and the phase speed approaches that of bar waves ($c/c_{\text{bar}} \to 1$, upper dashed line). At shorter wavelengths ($R/\Lambda \to \infty$) there are an infinite number of propagatory modes, all of which approach the speed of surface waves on an ideal, flat, semi-infinite medium, known as *Rayleigh waves* (lower dashed line). The speed of these waves, c_{Rayleigh}, is obtained from the pure real root of the polynomial

$$\kappa^6 - 8\kappa^4 + 8(3 - 2F(\nu))\kappa^2 + 16(F(\nu) - 1) = 0, \tag{29}$$

where $F(\nu) = (1 - 2\nu)/[2(1 - \nu)]$ and $c_{\text{Rayleigh}} = \kappa\, c_{s2}$ (Kolsky, 1953, Eq. (2.37)). As the speed only depends on the Poisson's ratio, Rayleigh waves are non-dispersive. Fig. 3 demonstrates good agreement between the present eigenvalue predictions and Davies's root-finding solution across all wavelengths.

3.1.2. Numerical accuracy

The value of N determines how many modes can be resolved and with what accuracy. This is influenced by the number of layers, their respective thicknesses, and the size of the numerical inner radius. If the inner radius reaches the same order as the smallest radial point spacing then it produces physical effects, which is obviously undesirable. From numerical experiments we found that the above dispersion diagram will be unchanged for $N \geq 25$ and a numerical inner radius $\leq R/20$. In other results N could be as low as 12 but the numerical inner radius had to be smaller, especially for mode shapes. For consistency, in the results that follow we set N=25 for each layer (independent of thickness) in all models and a numerical inner radius of $R/1000$. The only exception to this is one result in which the inner fluid, elastic solid and outer fluid layers had N of 25, 12 and 25, respectively; this necessity appeared to be related to the very low wave speed (Fig. 13 XIV).

There is, however, a limit for the numerical accuracy at very long wavelengths. Consider Fig. 4(a), which zooms in on the propagating (first) mode from Fig. 3. For $R/\Lambda > 0.015$, i.e., $\Lambda < 67R$, the numerical solution agrees with the long-wavelength analytical solution for bar waves, indicated by the dashed line ($c/c_0 = 1$). As the wavelength approaches the infinite limit, though, the numerical eigenvalue problem becomes increasingly ill-conditioned because of the limited precision available to solve the discretised equations. This behaviour can be quantified by plotting the condition numbers of the eigenvalues, as shown in Fig. 4(b); the dotted line corresponds to the double-precision limit of floating point arithmetic (16 significant figures; 64-bit variable type: `double` in the C++ code, `double precision` in the Fortran/LAPACK code); although arbitrarily high precision linear algebra libraries are available, e.g., MPACK (Nakata, 2010), the required eigenvalue subroutines have not been implemented. The condition number measures how much the output value of a function can change for a small change in the input argument. This gives a measure of how sensitive a function is to changes/errors in the input, and how much error in the output results from an error in the input. Generally speaking, for a condition number of 10^k, up to k digits of accuracy will be lost in addition to arithmetic losses of accuracy in the numerical method. In Fig. 4(b), as the wavelength approaches the infinite limit ($R/\Lambda \to 0$), the condition number approaches the numerical accuracy of the variable type, which results in the noisy deviation from the analytical solution seen in Fig. 4(a). In comparison, the condition numbers of the eigenvalues constituting the dispersion diagram in Fig. 3 are several orders of magnitude lower (10^8–10^{14}, not shown). The numerical solution also produces a non-physical mode that appears as a monotonically increasing curve starting from the origin in the dispersion diagram, which is easily filtered out by its abnormally low wave speeds.

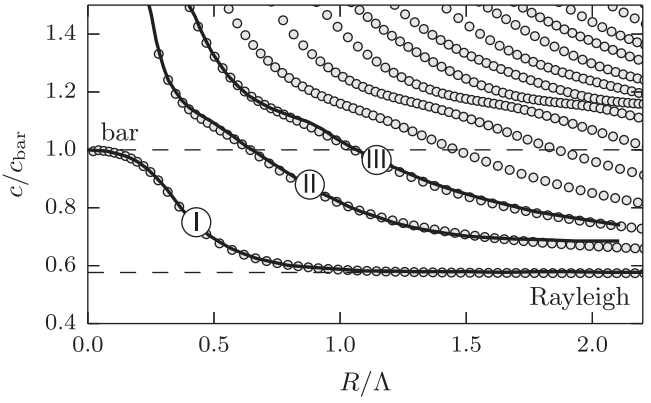

Fig. 3. Verification of our numerical code by comparison of the first three predicted wave modes (I, II, III) with those of the root-finding solution of Davies (1948) in the dispersion diagram for a semi-infinite cylindrical bar having a Poisson's ratio of ν=0.29; c is the wave speed, $c_{\text{bar}} = \sqrt{E/\rho}$ is the theoretical speed of bar waves in a semi-infinite elastic cylinder, where E is the Young's modulus and ρ is the density of the elastic material, R is the radius of the cylinder and Λ is the wavelength. The upper and lower dashed lines indicate the long (bar wave: $R/\Lambda \to 0$) and short (Rayleigh wave: $R/\Lambda \to \infty$) wavelength limits, respectively. Mode I is the only propagatory wave vibration mode at long wavelengths.

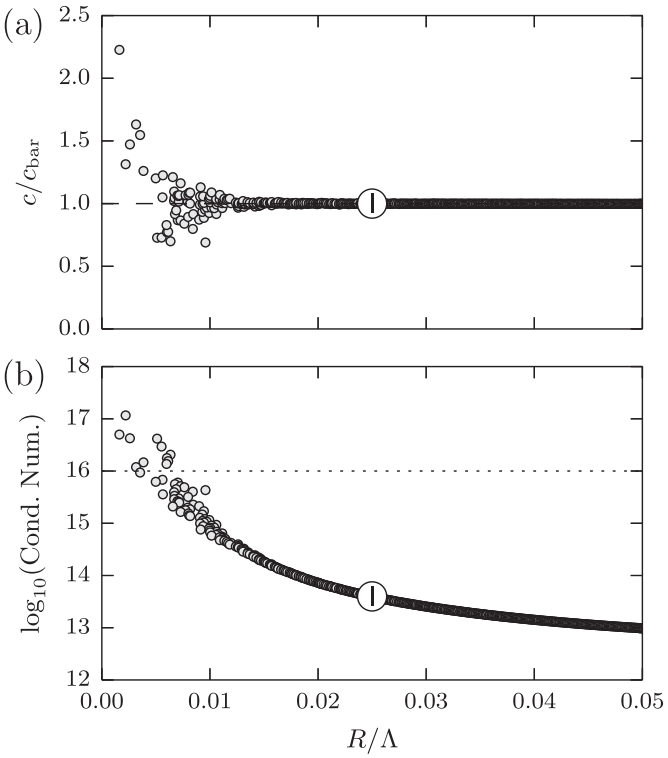

Fig. 4. (a) The data from Fig. 3 replotted at the long-wave limit of the propagating mode I; c_{bar} is the non-dimensional wave speed, where $c_{\mathrm{bar}} = \sqrt{E/\rho}$, and R/Λ is the non-dimensional wavenumber. (b) The condition numbers of the eigenvalues (wave speed) from the dispersion diagram in (a); the dotted line corresponds to the double-precision limit (10^{-16}) of the arithmetic used in the computations. As the wavelength approaches the infinite limit ($R/\Lambda \to 0$), the eigenvalue problem becomes increasingly ill-conditioned relative to the numerical precision available to solve the equations, indicated by the increasing condition number, which results in a noisy deviation from the analytical solution.

3.1.3. General validation

The theory of 3D longitudinal stress wave propagation in an infinite cylindrical rod was developed independently by Pochhammer and Chree in the late 1800s, but the solution to these frequency equations was not found until the 1940s (Bancroft, 1941; Hudson, 1943; Davies, 1948). The experiments on metal rods that led to the validation of the Pochhammer–Chree theory were those by Hopkinson (1914), Davies (1948) and Kolsky (1949). Some examples of dispersion curves (of the first mode at long wavelengths) derived from experiments that match the theory are found in Tu et al. (1953, Fig. 5), Zemanek and Rudnick (1961, Fig. 5) and Yew and Chen (1978, Fig. 2). For more information on the above experiments, the interested reader is referred to the review papers by Al-Mousawi (1986) and Gama et al. (2004). These established results serve to validate our waveguide model for the fundamental case of an elastic solid cylinder. The validation for application to the spinal canal is addressed in Section 3.3.3 in the context of modelling post-traumatic syringomyelia.

3.2. Eigen-analysis of the elastic waveguide

The results presented in this section have general application to waveguides in engineered systems. We analyse the dispersion behaviour and mode shapes of an elastic solid cylinder surrounded by an annulus of inviscid fluid, and compare this with the equivalent results for the cylinder being replaced by a thick-walled elastic tube filled with the same fluid. These fundamental results are also applied to the spinal canal, so we use anatomical terminology throughout to avoid dual nomenclatures. The inner fluid space, elastic solid cylinder/annulus and surrounding fluid annulus will be referred to as the syrinx, spinal cord (SC) and spinal subarachnoid space (SSS), respectively.

3.2.1. Dispersion diagrams

Fig. 5(a) is the dispersion diagram for a semi-infinite cylinder having a Poisson's ratio of $\nu = 0.49$, the default value for our SC material (Table 2); the surface of the cylinder is subject to a zero-stress boundary condition. Although the values of the remaining physical parameters do not affect the non-dimensional dispersion properties of the cylinder, they become relevant as we add additional layers to the geometry; we use the default values of E, ρ and R for our SC (Table 2). The speed of bar waves (upper dashed line) is $c_{\mathrm{bar}} = 3.9$ m/s, which gives the non-dimensional speeds of Rayleigh surface waves, 0.54 (lower dashed line; $c_{\mathrm{Rayleigh}} = 2.1$ m/s), shear waves, 0.56 (dotted line; $c_{s1} = 2.2$ m/s), and dilatational waves, 4.1 (not shown; $c_{s2} = 16$ m/s), in a semi-infinite (surface) or infinite continuum of SC material. The non-dimensional wavenumber axis can be interpreted in terms of the physical dimensions of

the SC. For a cord having radius R=4 mm and length L=400 mm (England and Wakeley, 2006): $R/\Lambda = 0.01$ corresponds to wavelengths as long as the cord or 100 cord radii, i.e., $\Lambda = L = 100R$, and the wavelength decreases as R/Λ increases, e.g., $\Lambda = 40R$ ($R/\Lambda = 0.025$), $\Lambda = 5R$ (0.2), $\Lambda = R$ (1).

Fig. 5(b) is the dispersion diagram for the model of the healthy SC depicted in Fig. 1(a). The outer surface of the model is now the rigid dura, which is implemented as a zero-displacement boundary condition (also employed in the model of the diseased SC). The addition of the SSS fluid layer means the wave energy of mode 1 must overcome greater inertia to propagate; long compressional waves approach the bar speed scaled down by the cross-sectional area fraction of the SSS (0.85, upper dashed line; $c_{\text{bar(scaled)}} = 3.3$ m/s),

$$c_{\text{bar(scaled)}} = \left[\frac{A_{\text{SSS}}}{A_{\text{SC}} + A_{\text{SSS}}}\right]^{1/2} c_{\text{bar}}, \tag{30}$$

where $A_{\text{SC}} = \pi R^2$ and $A_{\text{SSS}} = \pi(r_{\text{dura}}^2 - R^2)$ (Cirovic, 2009, Eq. (18): solution c_{s2}) At shorter wavelengths there are an infinite number of propagatory modes, which approach the speed of *Stonely waves* along the fluid–solid interface (0.48, lower dashed line; $c_{\text{Stonely}} = 1.9$ m/s) as the wavelength becomes small relative to the radial thicknesses of the interfacing solid and fluid layers. The speed of these non-dispersive waves, c_{Stonely}, is obtained from

$$\left[\left(\frac{c_{s2}}{c_{\text{Stonely}}}\right)^2 - \left(\frac{c_{s2}}{c_{\text{f}}}\right)^2\right]^{1/2} G\left(\frac{c_{s2}}{c_{\text{Stonely}}}\right) + \frac{\rho_{\text{f}}}{\rho_{\text{s}}}\left[\left(\frac{c_{s2}}{c_{\text{Stonely}}}\right)^2 - \left(\frac{c_{s2}}{c_{s1}}\right)^2\right]^{1/2} = 0 \tag{31}$$

where

$$G\left(\frac{c_{s2}}{c_{\text{Stonely}}}\right) = \left[1 - 2\left(\frac{c_{s2}}{c_{\text{Stonely}}}\right)^2\right]^2 - 4\left(\frac{c_{s2}}{c_{\text{Stonely}}}\right)^2\left[\left(\frac{c_{s2}}{c_{\text{Stonely}}}\right)^2 - \left(\frac{c_{s2}}{c_{s1}}\right)^2\right]^{1/2}\left[\left(\frac{c_{s2}}{c_{\text{Stonely}}}\right)^2 - 1\right]^{1/2} \tag{32}$$

is related to the Rayleigh-wave polynomial (Strick and Ginzbarg, 1956, Eqs. (1,2)).

The addition of the annular fluid space supports another wave, mode 2, which is also propagatory at the long-wave limit (i.e., has a finite velocity at $R/\Lambda \to 0$). We defer the description of this mode until the introduction of the inner fluid space so that it can be characterised in more general terms. Although waves composed of very long or short wavelengths will be non-dispersive, as per the aforementioned horizontal asymptotes, physiological excitation generates waves that contain a broad spectrum of wavelengths. The wavenumber–velocity curves in Fig. 5(a) and (b) are monotonically decreasing so the longer wavelengths in each mode will travel with a higher phase speed. Therefore, all mode 0 and mode 1 waves will spread out as they travel.

Introducing a syrinx changes the SC model from an elastic cylinder to a fluid-filled elastic tube. As seen in Fig. 5(c), at long wavelengths the longitudinal compressional wave (mode 1), termed a *Lamb wave* (Cirovic, 2009, Eq. (17)), speeds up (0.97, upper dashed line; 3.7 m/s), which is because of the fluid having a greater bulk modulus and a lower (zero) shear modulus than the solid it replaces. The tube also permits a transmural pressure wave to propagate (mode 0), termed a *Young wave* (Cirovic, 2009, Eq. (17)), which involves a localised distension/constriction of the tube and is slower than the Lamb wave, indicated here at the long-wave limit (0.44, lower dashed line; 1.7 m/s). At long wavelengths, the speeds of these two waves, c_i, are the roots of the biquadratic equation

$$\left(\frac{c_i}{c_{s2}}\right)^4 + \left[3\frac{A_{\text{SC}}}{(A_{\text{syrinx}} + A_{\text{SC}} + A_{\text{SSS}})} - 4\right]\left(\frac{c_i}{c_{s2}}\right)^2 + 3\left[\frac{A_{\text{SC}}}{(A_{\text{syrinx}} + A_{\text{SC}} + A_{\text{SSS}})}\frac{A_{\text{SSS}}}{(A_{\text{syrinx}} + A_{\text{SC}})}\right] = 0 \tag{33}$$

where $A_{\text{syrinx}} = \pi r_{\text{syrinx}}^2$, $A_{\text{SC}} = \pi(R^2 - r_{\text{syrinx}}^2)$ and A_{SSS} is as defined previously (Cirovic, 2009, Eq. (17)).

Fig. 5(d) shows the same dispersion diagram as 5(c) except zoomed out to reveal the full wavelength spectrum behaviour of mode 2. As demonstrated in the inset, none of the wave modes cross over; the blank section behind the inset corresponds to where yet

Table 2
Default anatomical parameter values.

Medium	Parameter	Value	Description
Fluid	ρ_{f}	1000 kg/m^3	Density
	K_{f}	2.3 GPa	Bulk modulus
Solid	ρ_{s}	1000 kg/m^3	Density
	E	15 kPa	Young's modulus
	ν	0.49	Poisson's ratio
(Geometry)	r_{syrinx}	2 mm	Radius of syrinx
	R	4 mm	Radius of spinal cord
	r_{dura}	7.5 mm	Radius of dura mater

higher frequency (>60 kHz) modes would appear, which are also kinked and more closely spaced. Therefore, upon distinguishing mode 2, we see that it has a speed that drops dramatically as R/Λ increases from 0. At the long-wavelength limit this *constrained longitudinal wave* (9.0, upper dashed line; 34.7 m/s) is much faster than the Lamb and Young modes. Its speed is given by

$$c_{\text{constrained}} = \left[\frac{A_{\text{syrinx}} + A_{\text{SC}} + A_{\text{SSS}}}{A_{\text{SC}}}\right]^{1/2} c_{\text{s1}} = \left[\frac{A_{\text{syrinx}} + A_{\text{SC}} + A_{\text{SSS}}}{A_{\text{SC}}}\right]^{1/2} H(\nu) c_{\text{bar}}, \tag{34a,b}$$

where $H(\nu) = \sqrt{(1-\nu)/[(1+\nu)(1-2\nu)]}$ and the cross-sectional areas are as defined above for Eq. (33). In other words, the constrained wave has the speed of dilatational waves through an infinite SC medium scaled up to include the cross-sectional area of the fluid surrounding the SC (cf. Bertram et al., 2005, Eq. (6)). Mode 2 exists because of the presence of the outer fluid layer (SSS) and in the healthy model its speed at the long wavelength limit is 7.8 (30.0 m/s, not visible in Fig. 5(b)), which is obtained from Eqs. (34a,b), with $A_{\text{syrinx}} = 0$. Mode 2 differs from modes 0 and 1 by its more dramatic dispersion. Thus a broad spectrum mode-2 impulse would spread out more as it travels than the equivalent response to impulses in modes 0 and 1.

The Young-wave curve in Fig. 5(c) shows a local minimum at $R/\Lambda = 0.44$ (and $c_2/c_0 = 0.35$), meaning that an impulse with wavelengths localised around 9 mm—approximately the diameter of the SC (Elliott et al., 2009; Morishita et al., 2009; Kim et al., 2013)—will propagate with minimal dispersion. Replotting Fig. 5 as ω vs. Λ (not shown) reveals that the group velocity ($\partial\omega/\partial\Lambda$) of these and all other wave modes is always positive, thus groups of waves will have an amplitude modulation envelope that propagates with a finite velocity.

3.2.2. Mode shapes

Fig. 6 shows the displacement and stress mode shapes for mode 1 (bar) and mode 2 (constrained) in the model of the healthy spinal canal having the default parameter values listed in Table 2. Similarly, Fig. 7 shows the mode shapes for mode 0 (Young), mode 1 (Lamb) and mode 2 (constrained) in the diseased model having a syrinx of size $r_{\text{syrinx}}/R = 0.5$. The three wavelengths correspond to $40R$ ($R/\Lambda = 0.025$), $5R$ ($R/\Lambda = 0.2$) and $1R$ ($R/\Lambda = 1$). As in the schematics in Fig. 1(a,b), the SC tissue has been shaded grey (Fig. 6: $0 \le r/R \le 1$; Fig. 7: $0.5 \le r/R \le 1$) to distinguish it from the fluids in the SSS ($1 \le r/R \le 1.875$) and syrinx when present (Fig. 7: $0 \le r/R \le 0.5$). As the mode shapes describe the harmonic response of the waveguide, which contain no magnitude information, the displacements ($\hat{u}_r$, $\hat{u}_z$) and stresses ($\hat{\sigma}_{rr}$, $\hat{\sigma}_{rz}$) have been normalized by their wavelength-specific modal maxima: $u_{\max} = \max(|u_r|, |u_z|) = \max(|u_z|)$, $\sigma_{\max} = \max(|\sigma_{rr}|, |\sigma_{rz}|) = \max(|\sigma_{rr}|)$, so $\hat{u}_r = u_r/u_{\max}$, $\hat{u}_z = u_z/u_{\max}$, $\hat{\sigma}_{rr} = \sigma_{rr}/\sigma_{\max}$, $\hat{\sigma}_{rz} = \sigma_{rz}/\sigma_{\max}$, and fluid pressure $\hat{p} = -\hat{\sigma}_{rr}$; i.e., a positive pressure is equivalent to a compressive radial (normal) stress. A given wavelength will change speed according to the geometrical configuration, as discussed in relation to the dispersion diagrams, thereby altering its frequency. Therefore, the non-dimensional speed and the frequency are given for each pair of mode shape plots. The mode shapes are dependent on E/ρ, ν and K_{f}, where $\rho_{\text{s}} = \rho_{\text{f}} = \rho$.

In all of the wave modes in both models, we see that at long wavelengths axial displacement dominates over radial ($\hat{u}_z \gg \hat{u}_r$), normal (radial) stress dominates over shear ($\hat{\sigma}_{rr} \gg \hat{\sigma}_{rz}$) but these become of the same order of magnitude as the wavelength approaches the radius of the SC. The geometrical similarity of the displacement mode shapes show that modes 1 and 2 of the healthy model (Fig. 6) become modes 1 and 2, respectively, of the diseased model (Fig. 7), when the syrinx is added. Mode 0 has no equivalent mode in the healthy model, though, as it requires a flexible-walled tube.

At long wavelengths, the SC tissue and the SSS fluid move axially out of phase for mode 0 (Fig. 7) and mode 1 (Figs. 6 and 7).The syrinx fluid also moves relative to the SC in these modes; mode 0 excites syrinx fluid motion in phase with the SC but with a larger relative amplitude, whereas in mode 1 the motion is of comparable amplitude but out of phase. Both wave modes would contribute to 'sloshing' motions of the syrinx fluid, which Williams (1980) first proposed as a mechanism for syrinx elongation through tissue hydrosection and remains a viable pathogenesis candidate (Elliott et al., 2013). Long wavelengths of mode 2, however, excite in-phase axial motion of the SSS fluid and SC tissue at similar amplitudes (Figs. 6 and 7) and very little motion of the syrinx fluid (Fig. 7).

In the healthy model, for all but the shortest wavelengths of mode 1, the peak stress is a normal stress at the centre of the SC (Fig. 6). In the presence of a syrinx of radius $r_{\text{syrinx}}/R = 0.5$, the stress is more concentrated (higher gradients) and peaks in the innermost portion of the SC tissue adjacent to the syrinx for all wave modes and wavelengths (Fig. 7). Being linear models, the associated strain profiles are identical. SC tissue damage in rats has been significantly correlated with maximum principal strain in contusion and dislocation injuries (Russell et al., 2012).

3.2.3. Parametric study

Here we investigate the sensitivity of the wave-bearing characteristics of the spinal canal to changes in the syrinx size (r_{syrinx}/R) and tissue compressibility (ν). To the knowledge of the authors, the Poisson's ratio of SC tissue has not been measured. Soft biological tissues exhibit non-linear viscoelastic behaviour, which is difficult to quantify because of the microstructural sensitivity to experimental protocols, sample preparation, preload, strain and strain rate (Tan et al., 2013). It is thus understandable that empirical estimates of SC tissue Young's modulus, a linear property, vary by some two orders of magnitude (Elliott et al., 2013). In our linear model, however, given that K_{f} is constant, E only serves to scale the wave speed as $\sqrt{E/\rho_{\text{s}}}$, and tissue density is all but invariant, as are CSF and SSS fluid densities. Therefore, E, ρ_{s} and ρ_{f} will be kept equal at the default values listed in Table 2.

In Fig. 8 the wave speed (c_2/c_{bar}) is plotted against Poisson's ratio ν for mode 2 in (a) the healthy model and in (b) the diseased model having the default syrinx occupying half of the cord radius ($r_{\text{syrinx}}/R = 0.5$). In each plot the solid line is the theoretical long-wave value and the three dotted lines with markers correspond to eigenvalue solutions at progressively shorter wavelengths. In both

models we see that c_2/c_{bar} is more strongly dependent on ν at longer wavelengths (smaller R/Λ). The theoretical and numerical predictions are in better agreement for larger ν, as near the limit of $\nu = 0.5$ the solid layer approaches the incompressibility of the two fluid layers, approximating the homogeneity of the theoretical wave's infinite medium; see Eq. (34a,b).

Fig. 9 again shows the variation of c/c_{bar} with ν but this time for all three modes of the diseased model at a single long wavelength ($R/\Lambda = 0.025$) and syrinx radii r_{syrinx}/R of (a) 0.25, (b) 0.5 and (c) 0.75. Clearly the wave speed of mode 2 is more dependent on ν than that of modes 0 and 1. Furthermore, the wave speed of mode 2 is of the same order of magnitude as that of modes 0 and 1 for small ν and small r_{syrinx}. The eigenvalue predictions for mode 2 agree better with the long-wave theory for thinner walled tubes; i.e., for larger r_{syrinx}/R.

In Fig. 10 the data from Fig. 9 has been replotted with the syrinx radius on the abscissa, giving separate plots for each of the three ν values (a) 0.49, (b) 0.37 and (c) 0.25. The additional markers at $r_{syrinx}/R = 0$ correspond to the healthy model. It is evident that the wave speed of mode 2 is more sensitive to r_{syrinx}/R than are modes 0 and 1. Here, as observed by Cirovic (2009) in his analytical model, modes 0 and 1 converge to (almost) the same speed as the syrinx radius reduces to zero for $\nu = 0.49$. When the SC has appreciable compressibility, though, these two wave modes maintain distinct speeds. The relationship between the stress concentration in the SC and the syrinx radius will be presented in the section that follows.

3.3. Pathogenesis of post-traumatic syringomyelia

The findings from Section 3.2, that have general applicability in FSI, will now be used to interpret the following results that pertain specifically to spinal-cord mechanics and their pathological augmentation. Although the full wavelength spectrum is physiologically relevant, we limit the foregoing analysis to long wavelengths to keep the scope manageable and to permit direct comparison with other published work. The same methods could readily be used, though, to repeat the investigation using a wavelength that is of similar magnitude to the SC radius.

3.3.1. Background

The causes of syringomyelia have been postulated in myriad hypotheses that attempt to make sense of its association with almost every pathology of the spinal canal and craniocervical junction (Klekamp, 2002). These include malformations of the brain, SC and the bones that house them (e.g., Chiari malformation, spina bifida), tumours (in the SC, SSS and epidural space), degenerative diseases of the spine (e.g., disc disease, scoliosis, spinal stenosis), and diseases of the arachnoid mater following meningitis, surgery, haemorrhage and trauma. Of all patients presenting with syringomyelia, approximately 10% will have suffered SC trauma (Moriwaka et al., 1995; Sakushima et al., 2012). The most common causes of SC injury are automotive accidents and falls, which collectively account for between two thirds and three quarters of all cases (Norton, 2010; Chen et al., 2013).

In the first 30 years after suffering a spinal injury, around a quarter of patients will develop a syrinx, usually juxtaposed to the injury site (Brodbelt and Stoodley, 2003). Although the mechanisms governing the formation and expansion of these syrinxes remain unknown, what these patients have in common are arachnoiditis and subarachnoid scar tissue formation (Klekamp et al., 1997), which can obstruct CSF flow (Klekamp et al., 2001; Klekamp, 2002; Gottschalk et al., 2010), can constrain the SC's movement by abnormal tethering (Klekamp, 2002; Schwartz et al., 1999), and—it has been proposed—may reduce spinal canal compliance (Brodbelt and Stoodley, 2003).

In what follows we investigate the progression of CSF flow blockage in the SSS and the subsequent formation and radial expansion of a syrinx through simulations of a sequence of discrete states. The spinal canal, like the rest of the human body, is governed by homeostasis, which is a physiological control system that regulates certain variables to maintain a stable and healthy state. Typical examples of homeostasis include the regulation of temperature, of fluid volume and pressure, and the balance between acidity and alkalinity. We analyse the mechanistic origins of CSF blockage and syrinx formation and consider how they might be related to determine if there is any mechanical benefit in the presence of the syrinx in post-traumatic syringomyelia. In other words, we look for mechanical variables, such as wave speed and stress, whose regulation could be part of a homeostatic control process attempting to recover from a pathological perturbation.

The following two sections detail the modelling limitations (Section 3.3.2) and the validation of the waveguide model (Section 3.3.3) specific to the spinal canal. It is at the reader's discretion to continue in textual order or jump straight to the main results in Sections 3.3.4 and 3.3.5 and return to Sections 3.3.2 and 3.3.3 after assimilating the analysis.

3.3.2. Limitations of the present approach to modelling the spinal canal

We have presented the solution to an eigenvalue problem that gives the dispersion behaviour and associated mode shapes of a cylindrical waveguide having fluid and solid layers. We have used this as a tool for studying the broad wave propagation characteristics of the spinal CSF system and how they vary in the presence of a syrinx. Before we apply our model to a more detailed analysis of the development of post-traumatic syringomyelia, it is prudent to review how well the simplified mechanics represents the human anatomy and physiology.

Unlike other spinal FSI models (Table 1), we do not solve an initial-value problem. The eigensolution is an intrinsic property of the system that represents the harmonic response to an arbitrary perturbation—it contains wave speed and shape information for all propagation modes but no amplitude information. The response to a specific perturbation will be the weighted sum of the mode shapes across the spectrum of wavelengths for all modes. As this is the first attempt at modelling the dispersion behaviour and the displacement and stress mode shapes of the spinal canal, we made several simplifications to keep the analysis tractable.

The cross-sectional structure of the healthy SC model (Fig. 1(a)) is a significant abstraction of the anatomy depicted in Fig. 2(b).

Some features have been omitted (central canal, spinal nerve roots, denticulate ligaments, spinal blood vessels, epidural fat) while others have been idealized (no distinction between grey and white matter, pia mater and SC tissue treated as one, simple elastic SC tissue, rigid dura, inviscid fluids). These simplifications affect the dynamic compliance of the spinal canal hence its wave propagation characteristics.

To simplify the analysis we made the dura rigid, which most closely approximates the limiting situation of a SSS fully obstructed with arachnoid scar tissue. In a fully flexible model, though, there are four wave modes: (i) mode 0*, a Young mode of the inner tube (SC), mostly involving motion of the inner tube; (ii) mode 1*, a mixed Lamb mode of the inner tube (SC) with highly coupled motion of both tubes; (iii) mode 2*, a mixed Young mode of the outer tube (dura) involving highly coupled motion of both tubes; and (iv) mode 3*, a Lamb mode of the outer tube (dura), mostly involving motion of the outer tube (Cirovic, 2009; Bertram, 2009). By making the dura rigid we remove the outer tube as a wave-bearing structure and its contribution to the overall dynamic compliance, which has several consequences. Mode 0* speeds up and the involved deformation amplitude of the SC reduces (becoming our mode 0), causing a concomitant reduction in the syrinx and SSS fluid sloshing. Mode 1* also speeds up but as the motion of the SC is uncoupled from that of the dura (becoming our mode 1), the full effect of the rigid dura is less straightforward to predict. Modes 2* and 3* are replaced by our mode 2, first predicted by Bertram et al. (2005), which is essentially the contribution of the SC to the mixed Young (2*) and Lamb (3*) modes of the dura (cf. mode 'w3' in Fig. 11 of Bertram, 2009). The Lamb mode of the dura (3*) is the least significant in terms of fluid movement in the SSS (Cirovic, 2009) and, by implication, in the syrinx (Elliott, 2012), for almost perfectly incompressible tissues. The Young mode of the dura (2*), however, generates more significant fluid motions, albeit only when the SSS is significantly obstructed and the syrinx has just initiated (Cirovic, 2009). Nonetheless, the fluid movements caused by mode 2* are secondary to those involved in the Young mode of the more compliant SC (0*), which is the mode least affected by our imposition of a rigid dura (mode 0).

The effect of treating the grey matter and white matter as a single homogeneous material is unclear. The Young's moduli of these two types of nervous tissue have been reported as being quite similar in rabbits (3.0 kPa and 3.5 kPa, respectively, by pipette aspiration, Ozawa et al., 2001), yet quite different in cows (1660 ± 160 kPa @ 0.05 s^{-1} and 940 ± 130 kPa @ 0.05 s^{-1}, respectively, by 1D tension, Ichihara et al., 2001). The individual Young's moduli of the grey matter and white matter in human SC, however, have not been measured. In the SC, neither do we distinguish between the soft nervous tissues and the microscopically thin yet much stiffer pia mater membrane that surrounds the SC (Fig. 2(a) and (b)). Bertram showed in a finite element model that the pia mater

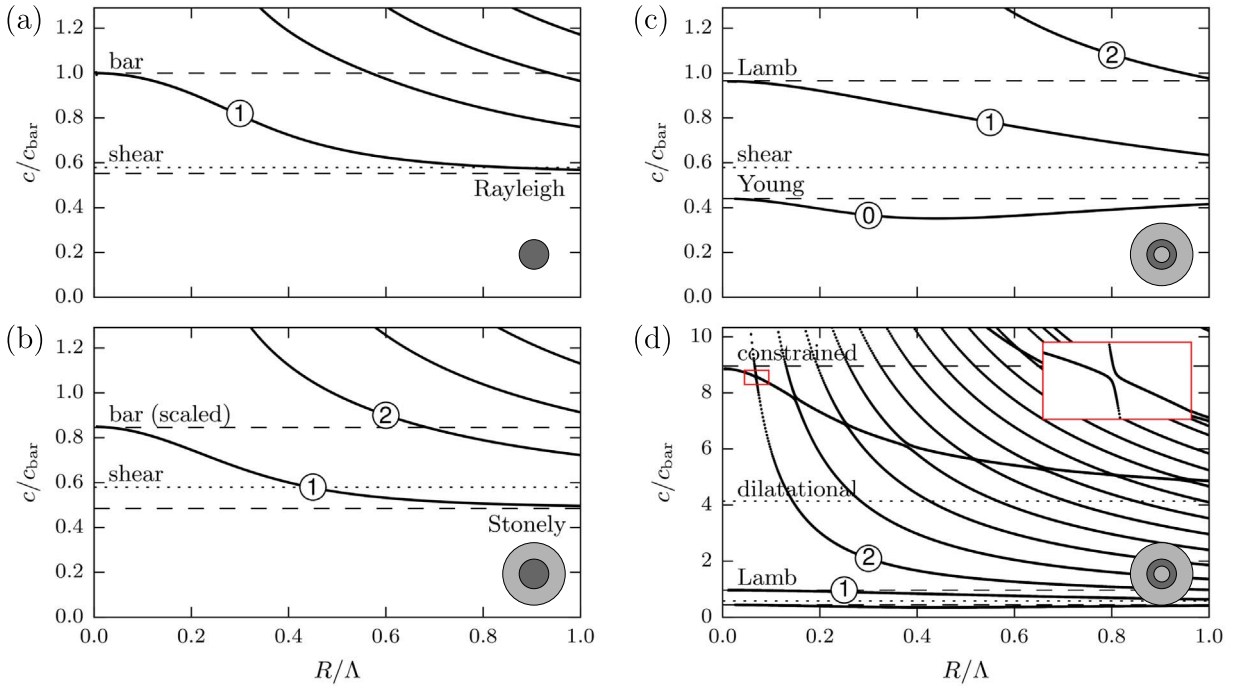

Fig. 5. Dispersion diagrams for the spinal canal models indicated by the inset cross-sectional diagrams; c_{bar} is the non-dimensional wave speed, where $c_{bar} = \sqrt{E/\rho}$, and R/Λ is the non-dimensional wavenumber. (a) Spinal cord in vacuo, i.e., a simple elastic cylinder, exhibiting a single propagatory mode at long wavelengths, mode 1, which approaches the speed of bar waves and Rayleigh waves at long ($R/\Lambda \to 0$) and short ($R/\Lambda \to \infty$) wavelength limits, respectively (equivalent to the dispersion diagram of Fig. 3 but with $\nu = 0.49$). (b) Healthy spinal canal, corresponding to the cross-section shown in Fig. 1(a), exhibiting two propagatory modes (1, 2) at the long wavelength limit; mode 1 is slowed by the presence of the fluid layer, which approaches the speed of Stonely waves at short wavelengths. (c) Diseased spinal canal, corresponding to the cross-section shown in Fig. 1(b), which has three propagatory wave modes (0, 1, 2) at long wavelengths, mode 0 appearing with the inclusion of the inner fluid cylinder. (d) The same data as plot (c) but zoomed out to reveal the long-wavelength limit of mode 2. A similar rescaling of the vertical axis would show the extent of mode 2 in plot (b). The inset figure in (d) demonstrates that the higher-order wave modes do not cross each other, thus what appears to be a thick solid line approaching the speed of constrained waves at the long wavelength limit is a graphical artefact caused by the finite size of the circular markers used to plot each eigenvalue. The values of the fluid, solid and geometrical parameter values are given in Table 2.

makes little difference to the mechanics of the intact SC but acts to limit SC distension when a syrinx is present (Bertram, 2010); this protective role agrees with the measurements of Ozawa et al. (2004) on rabbit SCs. Therefore, incorporating a separate pia mater membrane would modify the mode shapes of our diseased model.

The dura mater has a Young's modulus approximately 100 times greater than that of the pia mater, which has a Young's modulus approximately 100 times greater than the SC nervous tissue (Elliott et al., 2013). Thus, there are three main sources of spinal compliance spanning four orders of magnitude. In the present work, we reduce this to one source of compliance, the SC. Nonetheless, we are still able to capture three of the four wave modes.

The cardiac reciprocating CSF flow in the healthy SSS appears to be inertia dominated. Loth et al. (2001) computed the Womersley numbers ($\mathrm{Wo} = R_{\mathrm{hyd}}\sqrt{\omega\rho/\mu}$, where R_{hyd} is the hydraulic radius, ω is the pulsation frequency, ρ is the density and μ is the dynamic viscosity) at various cross sections of the spinal canal of Visual Man (of the Visible Human Project) for a periodic flow of 50 bpm, and found the values varied between 5 and 17. Martin et al. (2013) performed CFD simulations in the 3D model of a healthy spinal canal, constructed from MRI and driven by MRI-derived flow profiles, and computed $\mathrm{Wo}=12.7 \pm 1.3$ (lower Wo were computed in pre- and post-surgery models of patients with Chiari I malformation, which causes a CSF obstruction in the craniocervical junction).[4] In general, for $\mathrm{Wo} > 10$, the viscous effects will be small. Also, Stockman's (2006) flow computations showed that subarachnoid obstacles, such as trabeculae and denticulate ligaments, do not greatly modify the fluid velocity profiles. In our spinal geometry, $R_{\mathrm{hyd}} = (r_{\mathrm{dura}} - R)$ for the SSS and $R_{\mathrm{hyd}} = r_{\mathrm{syrinx}}$ for the syrinx. As we are modelling pulse waves, $\omega = 2\pi/\tau$, where $\tau = w/(2c)$ is the rise time for a pulse of width w having speed c (Elliott, 2012). For $\mu = 10^{-3}$ Pa.s (Loth et al., 2001; Martin et al., 2013), w=10 cm (Bertram et al., 2005), $c = c_{\mathrm{bar}}$ and the remaining parameter values from Table 2, Wo for the SSS spans from 77 for the healthy state down to 11 for the state of maximum obstruction ($r_{\mathrm{dura}} - R = 0.5$ mm), and the same range is found for the syrinx, 11 for the small syrinx ($r_{\mathrm{syrinx}} = 0.5$ mm) up to 77 for the largest syrinx ($r_{\mathrm{syrinx}} = 3.5$ mm). Dispersion will generally cause waves to spread out as they travel (Fig. 5), i.e., w will become larger, which will cause Wo to increase. Wave modes faster than the bar wave speed will also have a higher Wo. Therefore, the inviscid assumption is reasonable for modelling pulse wave propagation.

We chose a simple elastic (non-viscoelastic and non-poroelastic) solid to remove any sources of damping, thereby restricting our attention to wave propagation; having an inviscid fluid, of course, also serves this purpose. Nonetheless, SC nervous tissue, like all soft tissues, exhibits time-dependent deformation and associated energy losses. The majority of measurements of SC tissue elasticity, with or without pia mater, indicate that it is strain-rate dependent. As these experiments have been carried out on several different types of animals (cows, rabbits, guinea pigs, cats, dogs) and on humans, at various strain rates (0, 0.05–10 s^{-1}), in different directions (axial, transverse) and with different test modes (1D tension, compression, pipette aspiration), it is not surprising that the elastic moduli span three orders of magnitude (3–1400 kPa); for details, see Table 1 in Elliott et al. (2013). This lack of agreement does not permit us to determine how much wave attenuation is being neglected in assuming a simple elastic SC; for similar reasons, Bertram et al. (2008) did not attempt a comparison of the viscoelastic properties of his spinal canal model with published experiments. The SC is also poroelastic, which we account for in terms of its effect on overall tissue compressibility by varying ν between 0.25 and 0.49. The 1D analytical models of Elliott (2012) indicated that in a healthy spinal canal there will be little wave damping attributable to porous effects. Nonetheless, pathological alterations in the anatomy associated with syringomyelia, such as dilated PVS, SSS flow obstructions, and a stiffer and thicker pial membrane, were predicted to increase transpial flux and retard wave travel. In designing a fully poroelastic spinal model that supports free wave propagation (the wave propagation in Støverud et al. (2016) was prescribed by a moving boundary condition), one would need to take into account anisotropy, as it was also shown that the damping of a pressure wave increases with greater radial permeability (pia mater) but with lesser axial permeability (SC).

The full mechanics and property variations (with load) for actual spinal-cord material are currently unknown but will be extremely complex (and dependent upon multiple parameters). It is clear, though, that both the effective Poisson's ratio as well as the Young's modulus would change (Beatty and Stalnaker, 1986). In this work we deal with the former based on present (published) knowledge and heuristics. Our FSI methods could be applied to an improved model of spinal-cord tissue mechanics when the salient data become available.

To formulate the governing equations as Helmholtz ordinary differential equations (Eqs. (8) and (15a,b)), it was necessary to perform a separation of variables (r, z), which made the problem axisymmetric (Eq. (1)). Looking at Fig. 2(a), the spinal anatomy clearly varies in the circumferential direction; e.g., the denticulate ligaments attach to the lateral surfaces near the nerve roots, and blood vessels are predominantly located on the anterior and posterior surfaces (not shown in figure). From Fig. 2(b) we also see that the cord and SSS have elliptical cross sections. All published 2w-FSI models of the spinal canal are axisymmetric, as introducing a circumferential coordinate would either complicate the analytical treatment or make for impracticable computation times (the 3D model by Støverud et al. (2016) omits the SSS, making it a model of the SC rather than of the spinal canal). Although none of the FSI models include the above mentioned anatomical features, Bertram et al. (2008) did study the effect of pathological cord tethering, implemented in such a way that did not obstruct CSF flow. It was found that when a pulse wave passed through the spinal canal, axial tethering caused local tensile radial stress in the cord when it was not fixed cranially, and inextensible string connections between the cord and dura induced similar stress and also localised low pressure in the cord ($-(\sigma_{rr} + \sigma_{zz})/2$). It was suggested that tensile radial stress could create a syrinx cavity and transiently lowered pressure could draw in interstitial fluid if efflux were inhibited, filling the syrinx. The influence of denticulate ligaments and nerve roots on CSF flow—driven by the cardiac cycle—has been studied in 3D CFD models by Stockman (2006, 2007) and Pahlavian et al. (2014). The main effect of these structures was to increase fluid mixing; the CSF pressure was not greatly altered. Similarly, in moving from a circular to an elliptic rigid spinal canal,

[4] The Womersley number equation in Martin et al. (2013) contains a typographic error (p.4) but the calculations listed in Table 2 therein are correct.

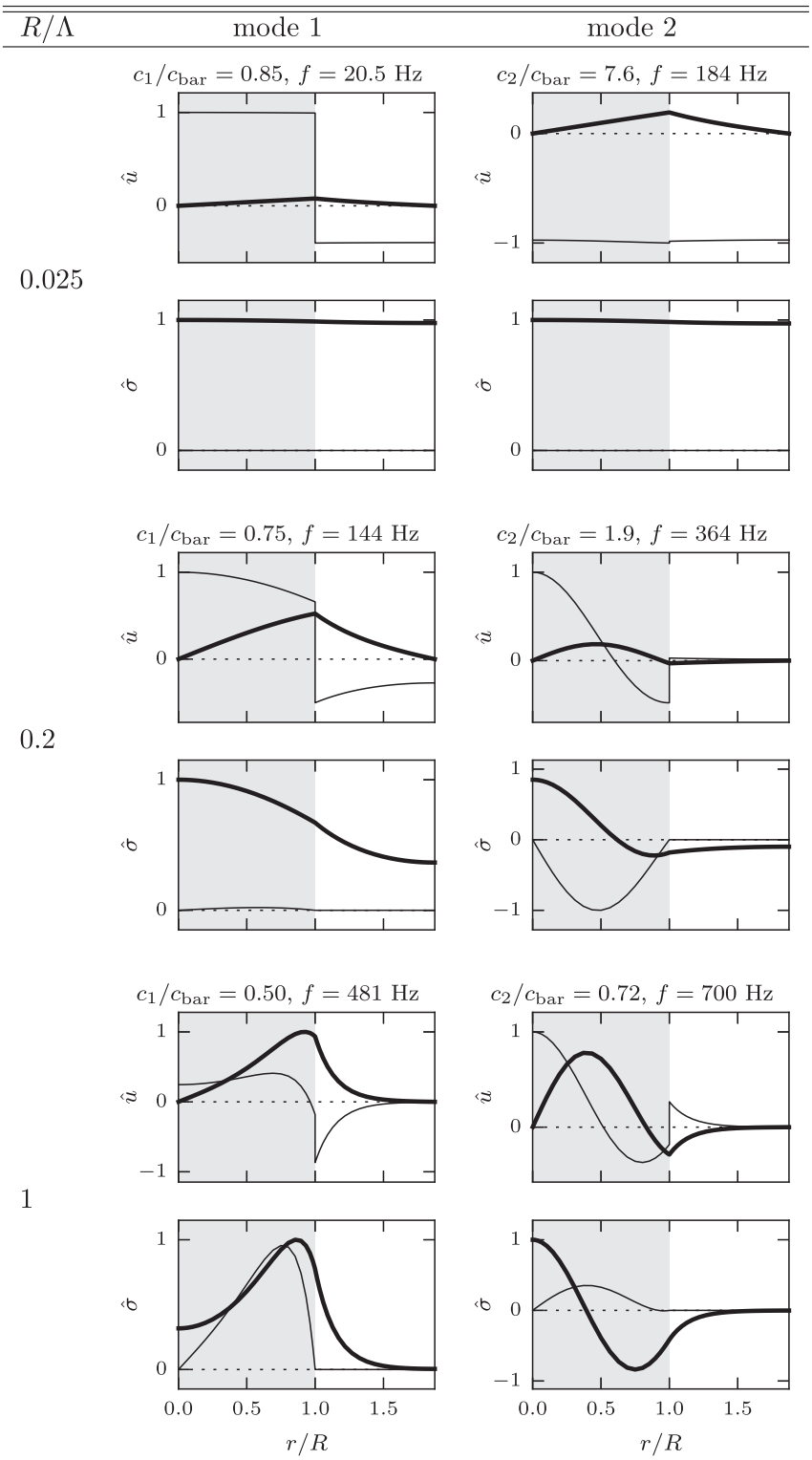

Fig. 6. Displacement (u) and stress (σ) mode shapes for the model of the healthy spinal canal (corresponding to the cross-section shown in Fig. 1(a)), which have been normalized by their wavelength-specific displacement and stress maxima, respectively; i.e., $\max(u) = \max(u_z)$, $\max(\sigma) = \max(\sigma_{rr})$, therefore $\hat{u}_r = u_r/\max(u_z)$, $\hat{u}_z = u_z/\max(u_z)$, $\hat{\sigma}_{rr} = \sigma_{rr}/\max(\sigma_{rr})$, $\hat{\sigma}_{rz} = \sigma_{rz}/\max(\sigma_{rr})$. In each plot the shaded region ($0 \le r/R \le 1$) corresponds to the inner elastic solid cylinder (spinal cord) and the remaining white region ($1 \le r/R \le 1.875$) corresponds to the outer fluid annulus (spinal subarachnoid space). Mode shapes are shown for long ($R/\Lambda = 0.025$), medium (0.2) and short wavelengths (1) of wave modes 1 and 2, where R is the spinal cord radius and Λ is the wavelength. The fluid, solid and geometrical parameter values are taken from Table 2, thus ν =0.49 in all plots. The thick lines (——) correspond to radial displacement ($\hat{u}_r$) and normal stress ($\hat{\sigma}_{rr}$); the thin lines (———) correspond to axial displacement ($\hat{u}_z$) and shear stress ($\hat{\sigma}_{rz}$). The non-dimensional speed (c_1/c_{bar}, c_2/c_{bar}) and the frequency (f) are provided for each mode shape; $c_{\text{bar}} = \sqrt{E/\rho}$.

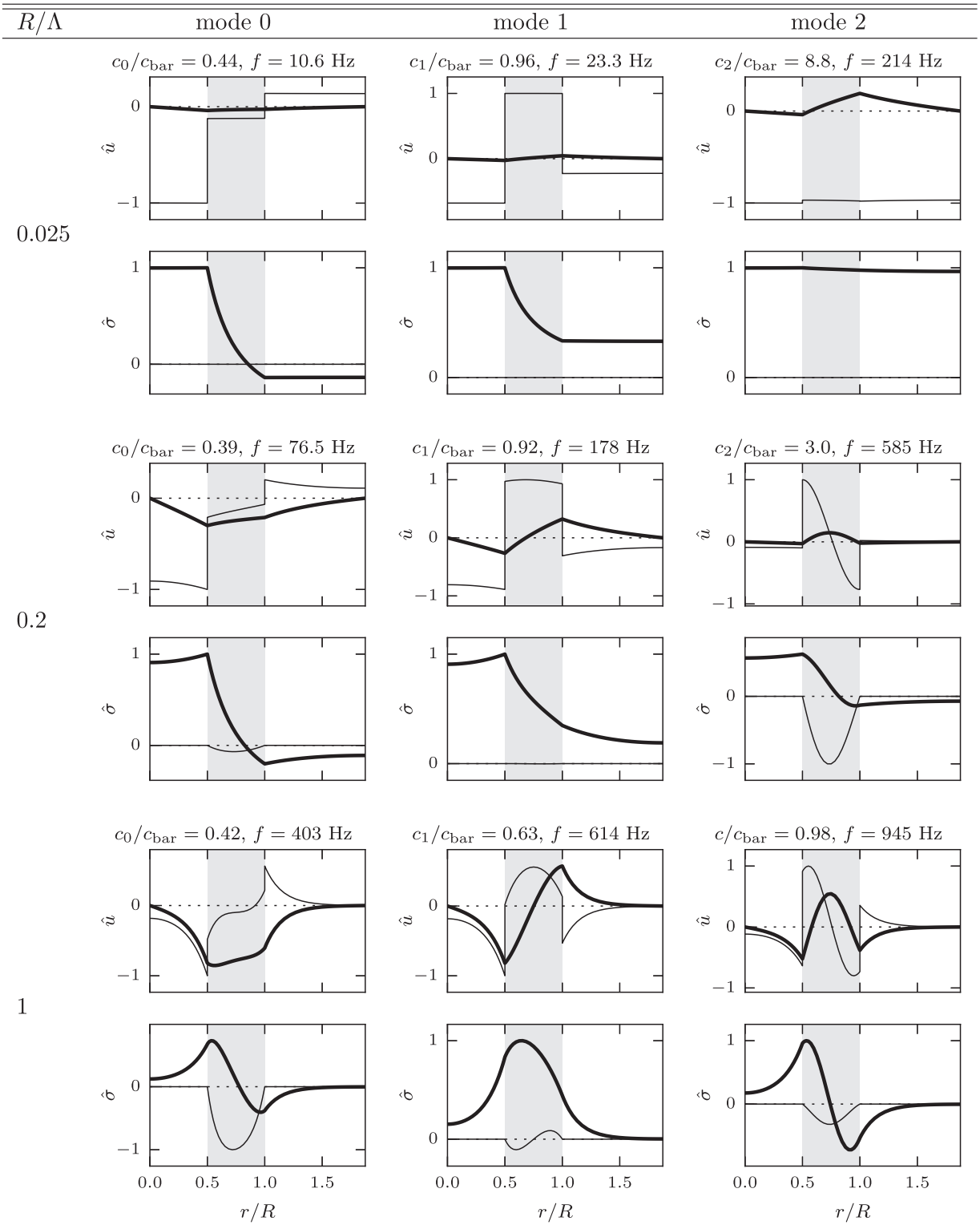

Fig. 7. Displacement (u) and stress (σ) mode shapes for the model of the diseased spinal canal (corresponding to the cross-section shown in Fig. 1(b)), which have been normalized by their wavelength-specific displacement and stress maxima, respectively; i.e., $\max(u) = \max(u_z)$, $\max(\sigma) = \max(\sigma_{rr})$, therefore $\hat{u}_r = u_r/\max(u_z)$, $\hat{u}_z = u_z/\max(u_z)$, $\hat{\sigma}_{rr} = \sigma_{rr}/\max(\sigma_{rr})$, $\hat{\sigma}_{rz} = \sigma_{rz}/\max(\sigma_{rr})$. In each plot the leftmost white region ($0 \le r/R \le 0.5$) corresponds to the inner fluid annulus (syrinx), the intermediate shaded region ($0.5 \le r/R \le 1$) corresponds to the elastic solid annulus (spinal cord), and the rightmost white region ($1 \le r/R \le 1.875$) corresponds to the outer fluid annulus (spinal subarachnoid space). Mode shapes are shown for long ($R/\Lambda = 0.025$), medium (0.2) and short wavelengths (1) of wave modes 0, 1 and 2, where R is the spinal cord radius and Λ is the wavelength. The fluid, solid and geometrical parameter values are taken from Table 2, thus ν =0.49 in all plots. The thick lines (——) correspond to radial displacement ($\hat{u}_r$) and normal stress ($\hat{\sigma}_{rr}$); the thin lines (———) correspond to axial displacement ($\hat{u}_z$) and shear stress ($\hat{\sigma}_{rz}$). The non-dimensional speed (c_0/c_{bar}, c_1/c_{bar}, c_2/c_{bar}) and the frequency (f) are provided for each mode shape; $c_{\text{bar}} = \sqrt{E/\rho}$.

even with eccentricity, Loth et al. (2001) found that the location of the peak velocity changed but the pressure profile was not significantly different.

Our governing equations model wave propagation in the longitudinal direction but for simplicity we assume small perturbations from longitudinally invariant cross-sectional geometry and elastic properties. The spinal anatomy, however, is not homogeneous. Broadly speaking, the elastic tissues and fluid spaces taper from the head end to the tail end. Furthermore, the segmental nature of the spine means that tissue structures, such as denticulate ligaments and nerve roots, repeat with every vertebra, giving the spinal canal periodically discontinuous elastic properties. These anatomical features would tend to scale the wave speeds, augment the mode shapes and induce wave reflection and refraction. Nonetheless, the main features of the dispersion diagram, the velocity ratios of fluid and solid layers and the locations of stress concentrations are unlikely to change in a qualitative way.

The final point we address here is the linearisation of the governing equations. The speeds of undamped waves are independent of their amplitude. Our mode shapes only apply to small perturbations and we acknowledge that percussive excitation may involve pressure amplitudes and gradients beyond the linear regime. The cough-induced CSF pulse waves measured by Williams (1976) varied in peak-to-baseline amplitude from 1.3 to 12.9 kPa (10–97 mmHg) and had a duration of 0.6–0.9 s. In a linear 1D coaxial tube model with flexible SC, dura and vertebral column, with interposing fluid in the SSS and epidural space, Cirovic and Kim (2012) predicted radial cord strains of up to 0.005 in the healthy cord and 0.03 in a cord section with a syrinx for an excitation of 1 kPa at one end of the tube; there was good agreement with an equivalent 2D finite element model. As the pulse wave in the SC (i.e., mode 1) had speeds of 6.8 m/s (heatlhy) and 2.8 m/s (cord section with syrinx), the overall compliance of the model is comparable to the present model. Similarly, Bertram predicted radial cord strains of up to 0.0001 for an excitation of 100-Pa amplitude (Bertram, 2009) and up to 0.002 for a 1-kPa excitation in models containing a syrinx (Bertram, 2010). According to the elasticity measurements of Ozawa et al. (2004), on rabbit SCs at least, the transverse stress–strain relationship of the cord without the pia will remain approximately linear for stretch ratios up to 1.3. When the pia mater was left attached, though, this relationship exhibited a slight concave upwards, which is accounted for by the differing material properties of soft hydrated substances (i.e., SC; Saxena et al., 2009) and collagen and elastin (i.e., pia; Meyers et al., 2008). Therefore, we would expect that a larger magnitude cough would still scale the mode shapes approximately linearly.

3.3.3. Validation of the waveguide model for application to the spinal canal

In the in vivo studies of spinal CSF pulse waves in humans, one subject with fused vertebrae volunteered for MRI study (Kalata et al., 2009) and the other subjects were patients referred for radiology following the diagnosis of back/neck problems (pain,

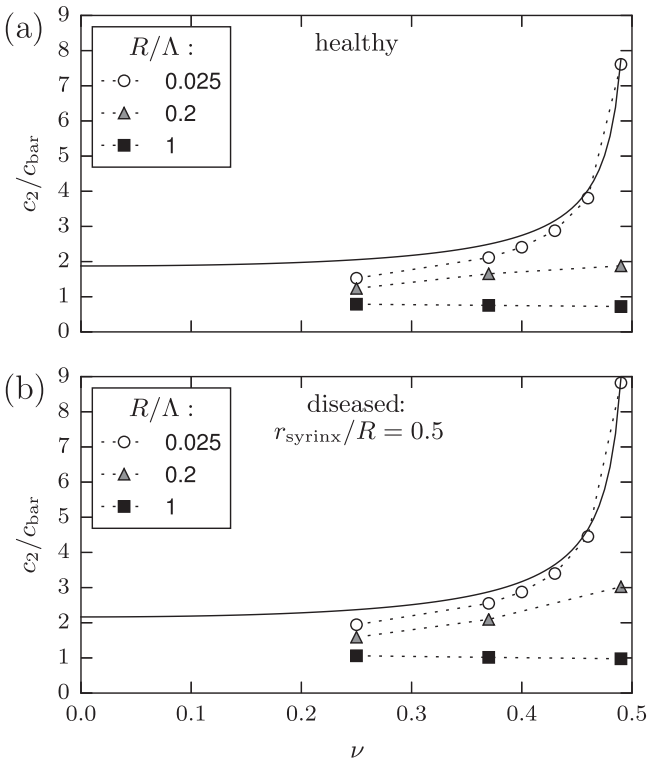

Fig. 8. Plots of the non-dimensional speed of mode 2 ($c_2/c_{\rm bar}$) over a range of compressibilities (ν) of the elastic solid (spinal cord tissue) for (a) the healthy model, and (b) the diseased model with a 2-mm-radius syrinx (corresponding to Fig. 1(a) and (b), respectively). The numerical eigenvalue solutions at long (R/Λ=0.025), medium (0.2) and short (1) wavelengths, indicated by shaded markers, are compared to the theoretical long-wave solution (R/Λ=0), which is plotted as a solid line; R is the spinal cord radius, Λ is the wavelength, $c_{\rm bar} = \sqrt{E/\rho}$, and non-varying model parameters are those listed in Table 2.

myelopathy, multiple sclerosis, muscle weakness, degeneration of intervertebral discs; Williams, 1976; Kalata et al., 2009). In Williams's (1976) cases, three patients were found to have normal radiology (imaging modality not specified) and there were findings of narrowed and of blocked SSS amongst the others; the clinical findings of the subjects in Kalata et al.'s (2009) study were not reported. Therefore, none of the measured wave speeds in humans correspond to a SC with a documented syrinx. Given that in a healthy SC the central canal almost disappears by adulthood (Milhorat et al., 1994), it is likely that most of the measured CSF pulse waves correspond to mode 1, as mode 2 travels too quickly (as does mode 3). If the central canal were patent or if an undetected syrinx were present in any of the subjects, possible in association with any of the spinal pathologies presented (Klekamp, 2002), then mode 0 waves would also have been present, which travel at a similar speed to mode 1 and thus may also correspond to the measured CSF pulse wave. In Bertram's (2009) simulations, mode 0 produced the largest (inward) deflection of the SC and thus induced the greatest fluid motion in the syrinx and SSS, whereas mode 1 caused the greatest rise in CSF pressure in the SSS (and also in the syrinx). Given that Williams (1976) measured CSF pressure and Kalata et al. (2009) measured CSF velocity, both in the SSS, it is likely that Williams's wave speed corresponds to mode 1, whereas Kalata et al's may correspond to either mode 0 (CSF motion) or mode 1 (no syrinx). Therefore, to validate our waveguide model, the predicted speeds of modes 0 and 1 should be close to the speeds of pulse waves measured in vivo; i.e., a non-dimensional speed of around 1 (1.1, Williams, 1976; 1.2 ± 0.4, Kalata et al., 2009). From

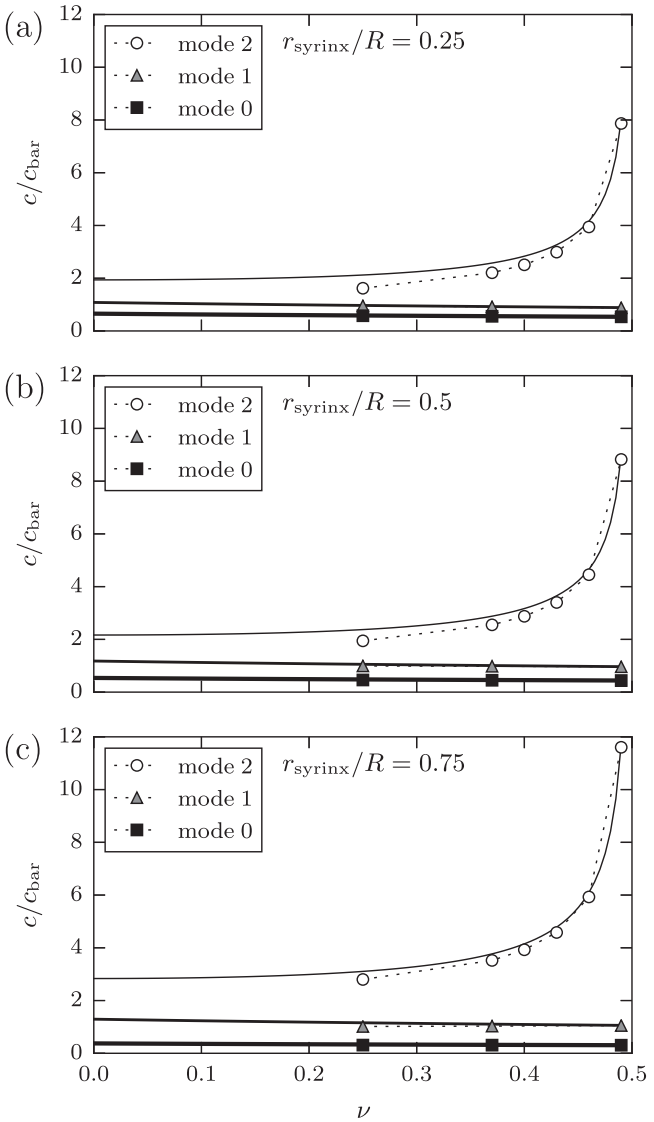

Fig. 9. Plots of the non-dimensional speeds of modes 0, 1 and 2 (c/c_{bar}) over a range of compressibilities (ν) of the elastic solid (spinal cord tissue) for three different sized syrinxes in the diseased model: (a) small, $r_{\text{syrinx}}/R = 0.25$, (b) medium, $r_{\text{syrinx}}/R = 0.5$, (c) large, $r_{\text{syrinx}}/R = 0.75$; r_{syrinx} is the syrinx radius, R is the radius of the spinal cord and $c_{\text{bar}} = \sqrt{E/\rho}$, see Fig. 1(b) for model configuration. The shaded markers indicate the numerical eigenvalue solution at a long wavelength ($R/\Lambda = 0.025$) and the solid lines of like tone correspond to their respective theoretical long-wave solutions ($R/\Lambda = 0$); Λ is the wavelength. Non-varying model parameters are those listed in Table 2.

Figs. 5(b,c), 9 and 10, we see that these waves have speeds approximately in the range 0.5–1 for small to medium sized syrinxes (r_{syrinx}/R=0–0.5) over the range of tissue compressibilities explored (ν=0.25–0.49). On this basis we deem that the dynamic compliances of our models are functionally appropriate—hence validated—by their associated wave speeds.

By comparing the lumbar and cisternal pressure traces recorded by Williams (1976), one observes that the wave propagation appears to involve dispersion. However, as the origin of the cough impulses were at a site somewhere between these two transducer locations, and with wave damping being clearly in effect, it would be difficult to characterise their dispersive nature. Furthermore, the tubes that connected the needles to the transducers had a natural frequency of 23 Hz, so to remove vibrations from the connecting lines all frequencies above 15 Hz were filtered from the output signal. Nonetheless, one can identify from the pressure traces a lowest frequency of approximately 5 Hz, giving a longest wavelength of approximatley 1 m, which would be nondispersive according to Fig. 5(b) and (c); mode 1, $R/\Lambda \approx 0.0005$. Higher frequencies (shorter wavelengths) are evident, though, in Kalata et al.'s (2009) MR measurements of CSF velocity. Broadly speaking, we would expect dispersion to occur at intermediate wavelengths in all modes, which would be most pronounced for mode 2 and least pronounced for mode 0, the latter being nondispersive for wavelengths around the diameter of the SC.

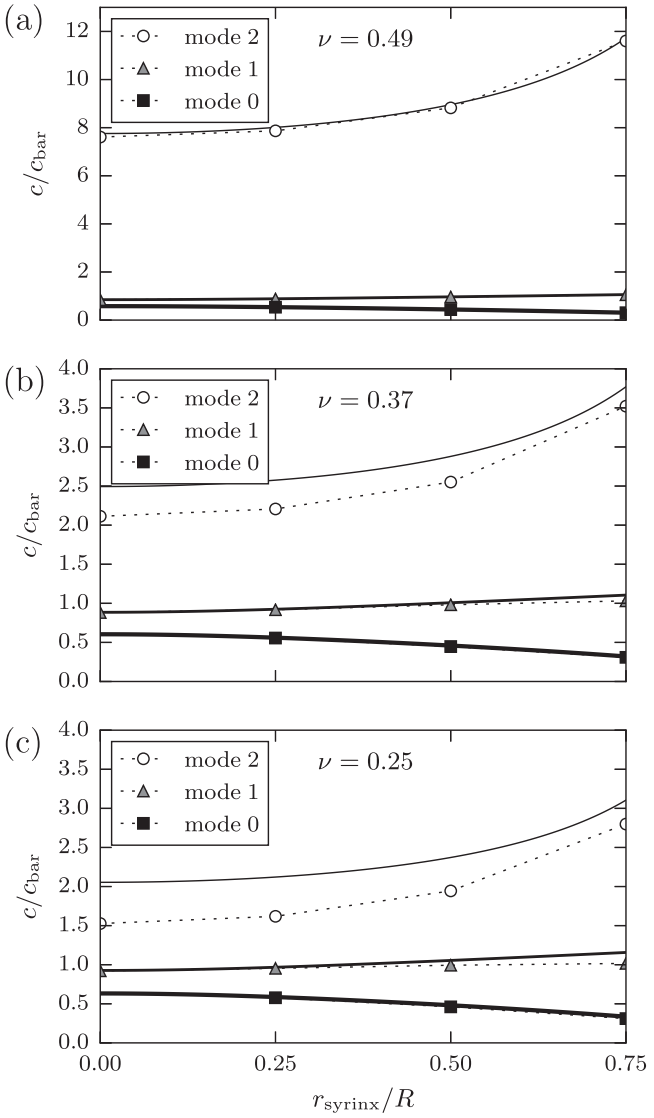

Fig. 10. Plots of the non-dimensional speeds of modes 0, 1 and 2 (c/c_{bar}) over a range of non-dimensional syrinx radii (r_{syrinx}/R) for three different compressibilities of the elastic solid (spinal cord tissue) in the diseased model: ν = (a) 0.49, (b) 0.37 and (c) 0.25; r_{syrinx} is the syrinx radius, R is the radius of the spinal cord and $c_{bar} = \sqrt{E/\rho}$, see Fig. 1(b) for model configuration. The shaded markers indicate the numerical eigenvalue solution at a long wavelength (R/Λ=0.025) and the solid lines of like tone correspond to their respective theoretical long-wave solutions (R/Λ=0); Λ is the wavelength. The solution at r_{syrinx}/R=0 corresponds to the healthy model with no syrinx. Non-varying model parameters are those listed in Table 2. Note that (a) has a different ordinate scale to (b) and (c).

3.3.4. Geometrical disease progression

Fig. 11(a) represents a healthy SC with the gradual blockage of the SSS (states I–VII: r_{dura} = 7.5 → 4.5 mm, 0.5 mm decrements; r_{syrinx} = 0 mm) and the subsequent formation of a syrinx (states VIII–XIV: r_{dura} = 4.5 mm; r_{syrinx} = 0 → 3.5 mm, 0.5 mm increments) in our axisymmetric cross-sectional model. From operating on patients with syrinxes, what appears to happen is that injury causes arachnoiditis—membranes of arachnoid that cross the SSS—and these appear to at least partially obstruct the SSS and may also

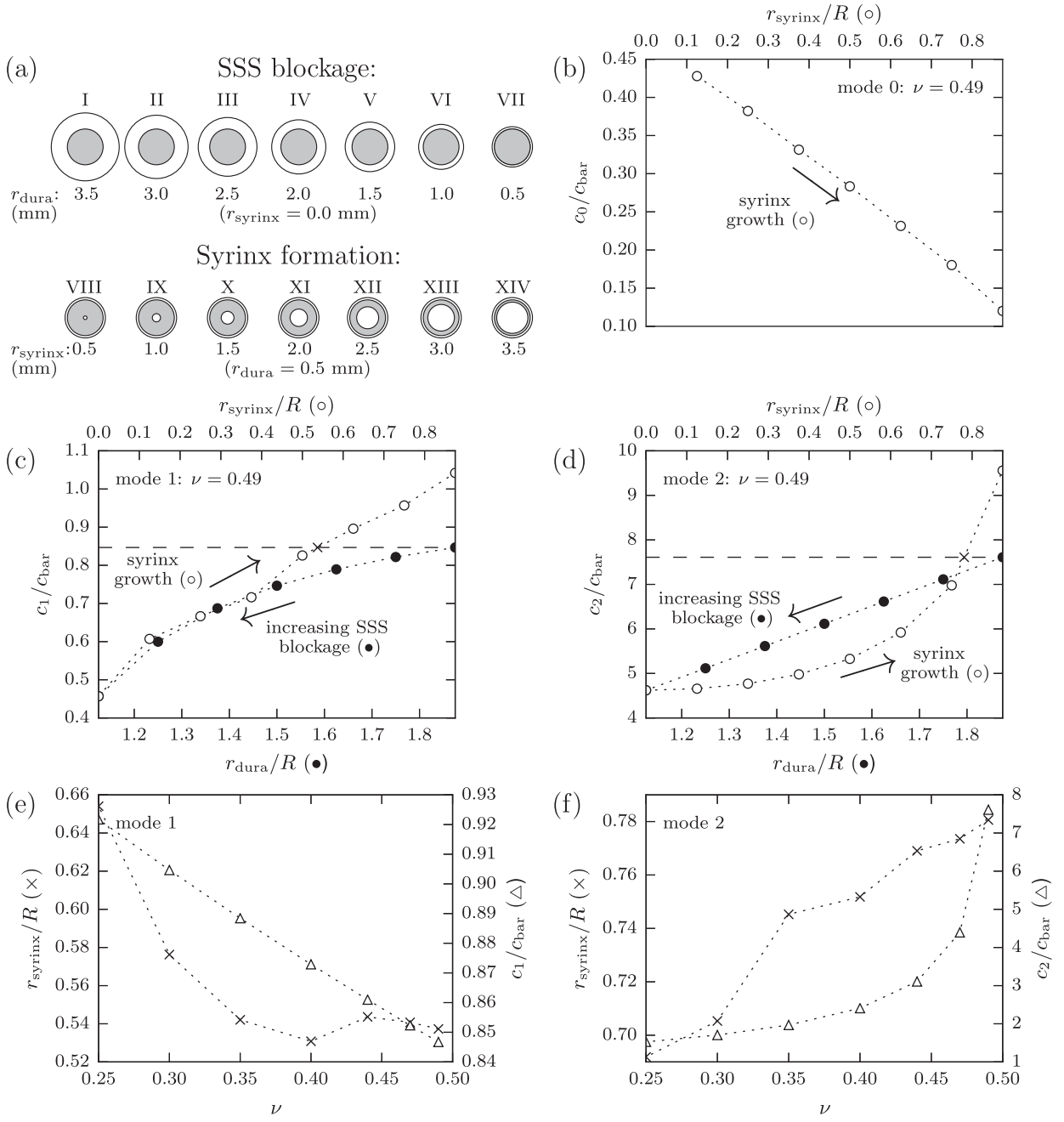

Fig. 11. Panel (a) depicts a series of discrete states that represent the geometric progression of spinal subarachnoid space (SSS) blockage (I–VII) and subsequent syrinx formation (VIII–XIV). The non-dimensional speeds of long waves (R/Λ=0.025) of modes 0, 1 and 2 (c_0/c_{bar}, c_1/c_{bar} and c_2/c_{bar}) throughout this sequence for ν=0.49 are shown in panels (b), (c) and (d), respectively; the lower abscissa indicates the degree of obstruction in states I–VII (r_{dura}/R), the results of which are plotted with '•' markers, and the upper abscissa indicates the size of the syrinx in states VIII–XIV (r_{syrinx}/R), the results of which are plotted with '○' markers; r_{syrinx} is the syrinx radius, r_{dura} is the dural radius, R is the radius of the spinal cord and Λ is the wavelength. The reattainment of the healthy wave speeds of modes 1 and 2 in the post-traumatic configuration are marked with an '×' in panels (c) and (d), respectively. These points of reattainment are replotted in panels (e) and (f), respectively, along with the equivalent points for ν = 0.25, 0.30, 0.35, 0.40, 0.44 and 0.47; the left ordinate indicates the radius of the syrinx required for reattainment (r_{syrinx}/R, '×' markers) and the right ordinate indicates the reattained wave speed (c/c_{bar}, '△' markers). Non-varying model parameters are those listed in Table 2.

tether the SC in a localised or more diverse area. This induces the syrinx. As the SC increases in size with the expansion of the syrinx, the SSS is further reduced. Therefore, in contrast to Fig. 11(a), real obstruction of the SSS is not axisymmetric, the scar tissue forms across the SSS rather than only at the dura mater boundary, which causes SC tethering, and it also involves distension of the SC due to syrinx expansion. Furthermore, the progression illustrated in Fig. 11(a) is unlikely to be linear in time. Nonetheless, we seek to understand this idealized disease process before adding more complex features. For this reason, to block the SSS we chose to reduce the diameter of the dura rather than increase that of the SC, as the latter would have introduced a concomitant change in the stiffness of the SC. Therefore, let us consider how this series of geometrical augmentations affects the speeds of long wavelengths ($R/\Lambda = 0.025$) of modes 0, 1 and 2 for the default Poisson's ratio $\nu = 0.49$, which are plotted in Fig. 11(b), (c) and (d), respectively. We defer analysing the associated effects on the stress and displacement mode shapes to the next section in which we include changes to tissue compressibility.

Mode 0 only exists in conjunction with a syrinx, thus the data in Fig. 11(b) refer to the obstructed states (VIII–XIV). As the syrinx distends, the mode 0 wave slows down, approaching zero velocity at the limit of an infinitely thin tube; i.e., $c_{\text{bar}}\sqrt{\delta_s/2}\sqrt{A_{\text{SSS}}/(A_{\text{syrinx}} + A_{\text{SC}} + A_{\text{SSS}})}$, where $\delta_s = 1 - r_{\text{syrinx}}/R$ (Cirovic, 2009, Eq. (19): c_{s1}). This occurs because the thinner the tube wall, the more fluid there is hence the greater the radial fluid inertia that must be overcome to permit the almost pure radial motion (distension/constriction) required for mode-0 wave travel. For smaller syrinx radii, less compressibility confers a slightly greater wave speed because the greater axial expansion (i.e., in the direction of wave travel) produced by the radial distension contributes to the wave propagation, but this ν dependency disappears when the tube wall is thin (plot omitted for brevity).

The mode-1 wave speed behaviour is shown in Fig. 11(c). As the SSS becomes increasingly obstructed (reducing r_{dura}/R, '•' markers, refer to lower abscissa), c_1/c_{bar} drops. This occurs because bringing the rigid dura boundary closer to the flexible SC surface constrains the coupled fluid–solid wave motion of the CSF and SC; as $\sqrt{A_{\text{SSS}}/(A_{\text{SC}} + A_{\text{SSS}})}$ approaches the theoretical limits of 0 (complete obstruction) and 1 (hypothetical situation of a very distended dura or a very thin SC, i.e., $r_{\text{dura}} \gg R$), c_1/c_{bar} also approaches 0 and 1, respectively; see Eq. (30). Having the rigid dura closer to the flexible SC surface means that the radial displacement becomes proportionally larger with respect to the (annular) channel height, which demands greater axial displacement of fluid to accommodate it; when the wave height is of the same order as the channel height, the radial distension requires the displacement of a column of fluid on either side of it (Burke et al., 2014). Therefore, a more blocked SSS increases the hydrodynamic inertial load in the SSS, which slows down mode 1. Introducing a syrinx causes the speed of mode 1 to rise again (increasing r_{syrinx}/R, '○' markers, refer to upper abscissa). As the syrinx expands to its radial limit, i.e., making the SC a thin-walled tube, the wave speed approaches $c_{\text{bar}}\sqrt{1/(1-\nu^2)}$ (Cirovic, 2009, Eq. (19): solution c_{s2}). Mode 1, without the presence of an inner fluid conduit, involves radial distension in a solid cylinder, which induces shear. When the syrinx appears, the shear strain diminishes as the wall thickness reduces, thus the wave propagates faster as it does not entail as much strain energy. When the syrinx reaches a radius of $r_{\text{syrinx}}/R = 0.54$, the wave speed of the healthy system is reattained (indicated by the '×' marker at the intersection with the dashed line).

Fig. 11(d) plots the equivalent situation for mode 2, the constrained longitudinal wave. As the SSS becomes increasingly obstructed, c_2/c_{bar} drops, because of the concomitant rise in hydrodynamic inertial load, as described above. Unlike mode 1, though, mode 2 always has a finite speed—even when the SSS is completely obstructed (as per Eqs. (34a,b) with $A_{\text{syrinx}} = 0$)—because the wave predominantly involves dilatational motion in the longitudinal direction. The introduction and expansion of a syrinx raises the mode-2 wave speed, which reattains the value of the healthy system at $r_{\text{syrinx}}/R = 0.78$ ('×' marker) and continues to rise, theoretically without bound, when the SC becomes a thin-walled tube ($r_{\text{syrinx}} \to 1$). As the wall thickness of the tube decreases, the wave motion involves ever less shear strain, hence the greater speed.

Repeating this simulation sequence of the geometrical evolution of post-traumatic syrinx formation for a series of ν values (down to 0.25), and calculating the syrinx radii at which the healthy wave speed is reattained, we generate Fig. 11(e) for mode 1 and Fig. 11(f) for mode 2. The healthy wave speed for mode 1 decreases slightly with increasing ν ($c_1/c_{\text{bar}} = 0.925 \to 0.845$, '△' markers) and, broadly speaking, this speed is reattained post-blockage at progressively smaller syrinx radii ($r_{\text{syrinx}}/R = 0.65 \to 0.53$, '×' markers); there is a slight deviation from the monotonic r_{syrinx}/R behaviour at $\nu = 0.40$–0.49, the cause of which is unknown. In contrast, the speed of mode 2 in the healthy configuration increases dramatically at higher ν values ($c_2/c_{\text{bar}} = 1.5 \to 7.5$), and a correspondingly more distended syrinx ($0.69 \to 0.78$) is needed to reattain this speed.

3.3.5. Geometrical and elastic disease progression

If the SC maintains its healthy diameter in the presence of a fluid-filled syrinx then there must be a concomitant reduction of fluid volume in the SC tissue; i.e., a decrease in the porosity of the tissue matrix and in the volume of the contained interstitial fluid. On this basis, the effective compressibility of the SC will be reduced. We therefore consider the post-traumatic modelling sequence depicted in Fig. 12(a). As before, the SSS is gradually obstructed (states I–VII) and a syrinx subsequently forms and expands (VIII–XIV). To allow the tissue compressibility to reduce as the syrinx expands, though, we assign to the healthy SC tissue $\nu = 0.25$, and then after the syrinx forms we gradually increment ν from 0.30 up to 0.49 as r_{syrinx} increases from 1 mm to 3.5 mm; see schematic annotations for (r_{syrinx}, ν) pairings in states VIII–XIV. Having established the wave speed behaviour resulting from simulations of purely geometrical changes in a post-traumatic syringomyelia development sequence (Section 3.3.4), we now look at how this behaviour is modified in the presence of changes to ν, and also analyse the associated mode shape behaviour.

Figs. 12(b) and (c) show how the wave speeds of modes 0, 1 and 2 change throughout the pathological sequence; 'Δ' markers correspond to SSS obstruction (lower abscissa, r_{dura}/R) and '∘' markers correspond to syrinx formation (upper abscissa, r_{syrinx}/R), which are shaded according to wave mode as indicated in the figure legends. As in the purely geometrical disease progression, modes 1 and 2 slow down with the gradual obstruction of the SSS but then recover their wave speeds with the expansion of the syrinx, which

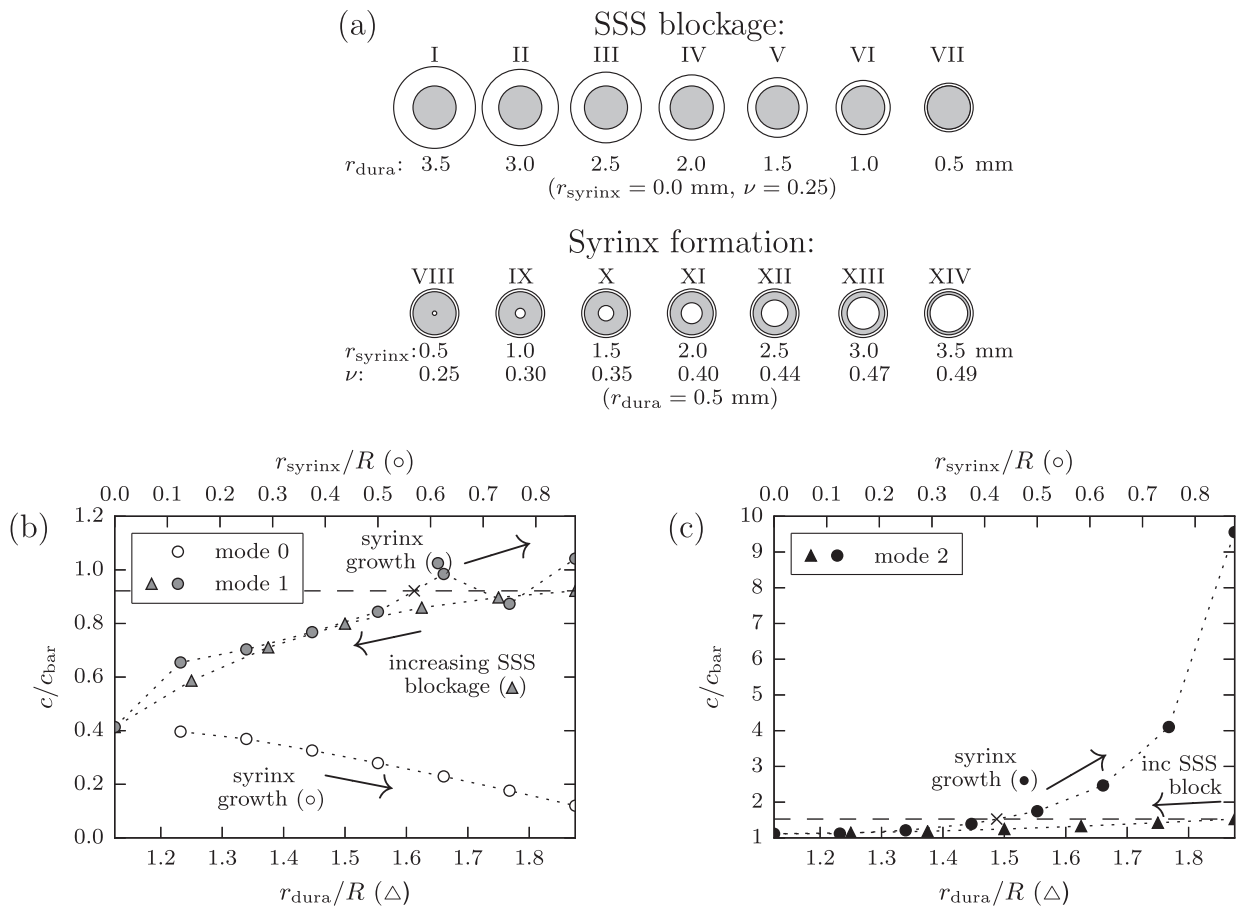

Fig. 12. Panel (a) depicts a series of discrete states that represent the geometric progression of spinal subarachnoid space (SSS) blockage at $\nu = 0.25$ (I–VII) followed by syrinx formation accompanied with decreasing spinal cord compressibility, indicated by increasing ν (VIII–XIV). Panels (b) and (c) show how the non-dimensional speeds (c/c_{bar}) of long waves (R/Λ=0.025) of modes 0 and 1, and 2, respectively, change during these simulated states of the disease progression. The lower abscissa indicates the degree of obstruction in states I–VII (r_{dura}/R), the results of which are plotted with '△' markers, and the upper abscissa indicates the size of the syrinx in states VIII–XIV (r_{syrinx}/R), the results of which are plotted with '○' markers; r_{syrinx} is the syrinx radius, r_{dura} is the dural radius, R is the radius of the spinal cord and Λ is the wavelength. Non-varying model parameters are those listed in Table 2. Note that (c) has a different ordinate scale to (b).

is also accompanied with the appearance and slowing of mode 0. Mode 1 recovers its healthy speed of 0.92 at a syrinx radius of 0.57 and mode 2 recovers its healthy speed of 1.53 at a slightly smaller radius, 0.42 ('×' markers on horizontal dashed lines). The deviation from non-monotonic behaviour in the speed of mode 1 at state XIII, where c/c_{bar} drops back below the dashed line (Fig. 12(b)), is related to the aforementioned trend observed in Fig. 11. The mode shapes of this case (Fig. 14 XIII), however, are consistent with the general trends for syrinx formation, which will be discussed below.

In terms of homeostasis, the mechanical advantages and disadvantages of a slower or faster wave speed are unknown. A slower wave exposes the cord tissue to potentially damaging stresses and spatial stress gradients for a longer duration, but a faster wave involves higher temporal stress gradients (i.e., more explosive impulses), which could also be damaging. Physical experiments are needed to evaluate the influence of wave speed on the degree of SC tissue injury.

Figs. 13–15 show the displacement and stress mode shapes for modes 0, 1 and 2, respectively, for the pathological sequence depicted in Fig. 12(a). The obstructed part of the SSS is shaded with a dotted pattern. We observe that the axial motions of the SC and the fluids in the syrinx and SSS change with SSS obstruction and syrinx size, and these tend to have a greater amplitude than the radial distension and constriction of the SC ($\hat{u}_z \gg \hat{u}_r$). The radial stress profiles in the SC tissue are affected by the size of the syrinx, but not by the degree of SSS obstruction; the shear stress is essentially non-existent ($\hat{\sigma}_{rr} \gg \hat{\sigma}_{rz}$). Pre-syrinx stress profiles are uniform and invariant (Figs. 14 I–VII and 15 I–VII). There is a phase-speed jump with a concomitant jump in frequency for mode 1 upon the appearance of the syrinx; i.e., $c_1/c_{\text{bar}} = 0.414$, $f = 10.0$ Hz (VII) $\rightarrow c_1/c_{\text{bar}} = 0.655$, $f = 15.8$ Hz (VIII), Fig. 14. We speculate that this jump occurs because at small syrinx radii the viscous forces being neglected in the syrinx are non-trivial in the fluid–structure wave motion. There is no such jump for mode 2, which involves primarily longitudinal dilatation in the SC tissue.

Regarding the progression of post-traumatic syringomyelia, we are interested in two mechanical features: fluid sloshing and stress concentrations. Sloshing is the axial movement of the syrinx fluid relative to the SC; it may be in phase or out of phase. Sloshing was proposed by Williams as a means of generating a stress concentration at the ends of a syrinx that could tear the SC tissue and elongate the syrinx cavity (Williams, 1980). A review of published modelling predictions indicates that this hypothesis

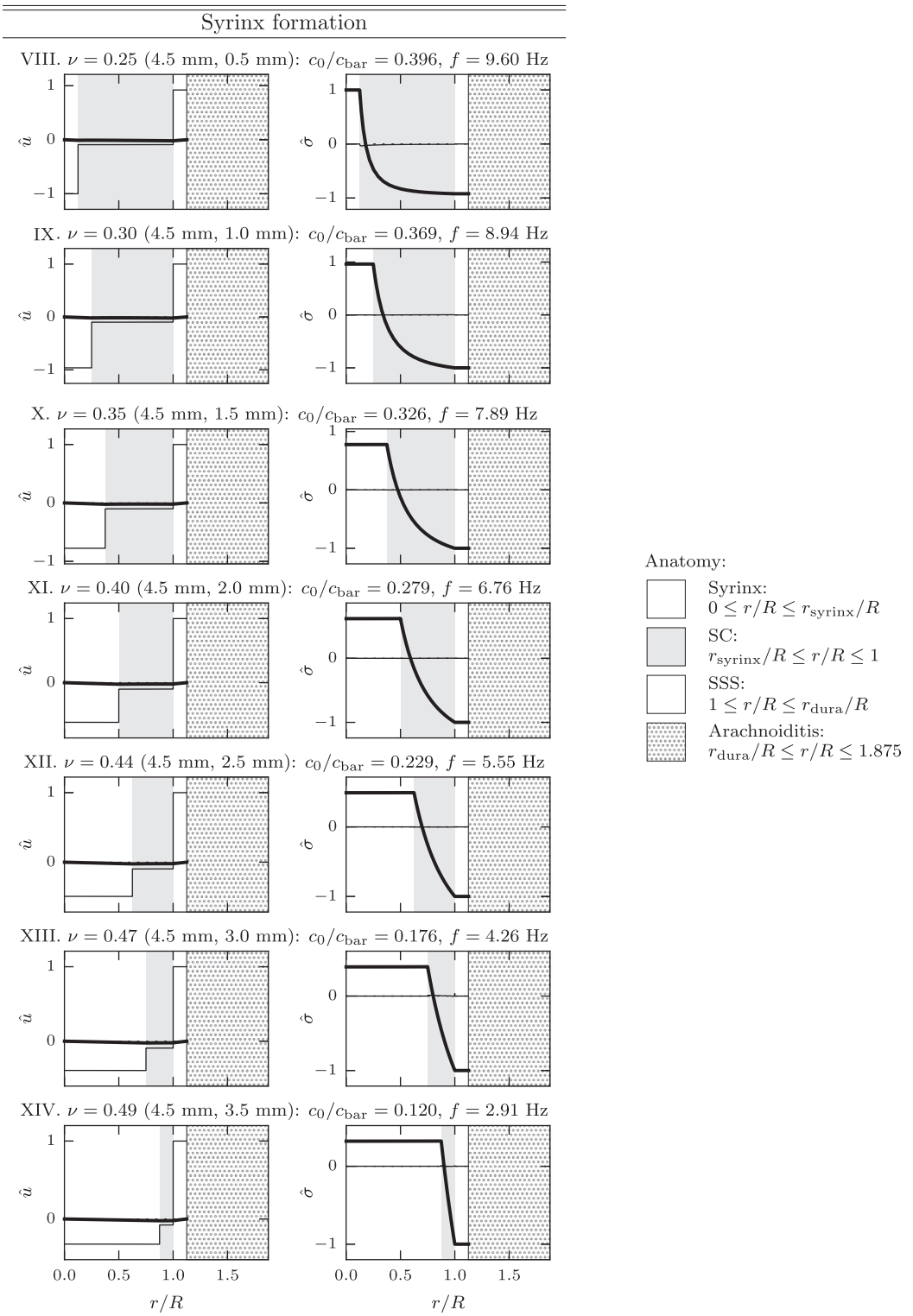

Fig. 13. Displacement (u) and stress (σ) mode shapes of mode 0 during states VIII–XIV of the simulated pathological sequence depicted in Fig. 12(a), which have been normalized by their wavelength-specific displacement and stress maxima, respectively; i.e., $\max(u) = \max(u_z)$, $\max(\sigma) = \max(\sigma_{rr})$, therefore $\hat{u}_r = u_r/\max(u_z)$, $\hat{u}_z = u_z/\max(u_z)$, $\hat{\sigma}_{rr} = \sigma_{rr}/\max(\sigma_{rr})$, $\hat{\sigma}_{rz} = \sigma_{rz}/\max(\sigma_{rr})$. Thick lines (——) correspond to radial displacement ($\hat{u}_r$) and normal stress (σ_{rr}); thin lines (———) correspond to axial displacement ($\hat{u}_z$) and shear stress ($\hat{\sigma}_{rz}$). The Poisson's ratio, dural radius, syrinx radius, non-dimensional speed (c_0/c_{bar}) and the frequency (f) are provided for each state; r_{syrinx} is the syrinx radius, r_{dura} is the dural radius, R is the radius of the spinal cord, Λ is the wavelength and $c_{\mathrm{bar}} = \sqrt{E/\rho}$. Non-varying fluid, solid and geometrical parameter values are taken from Table 2.

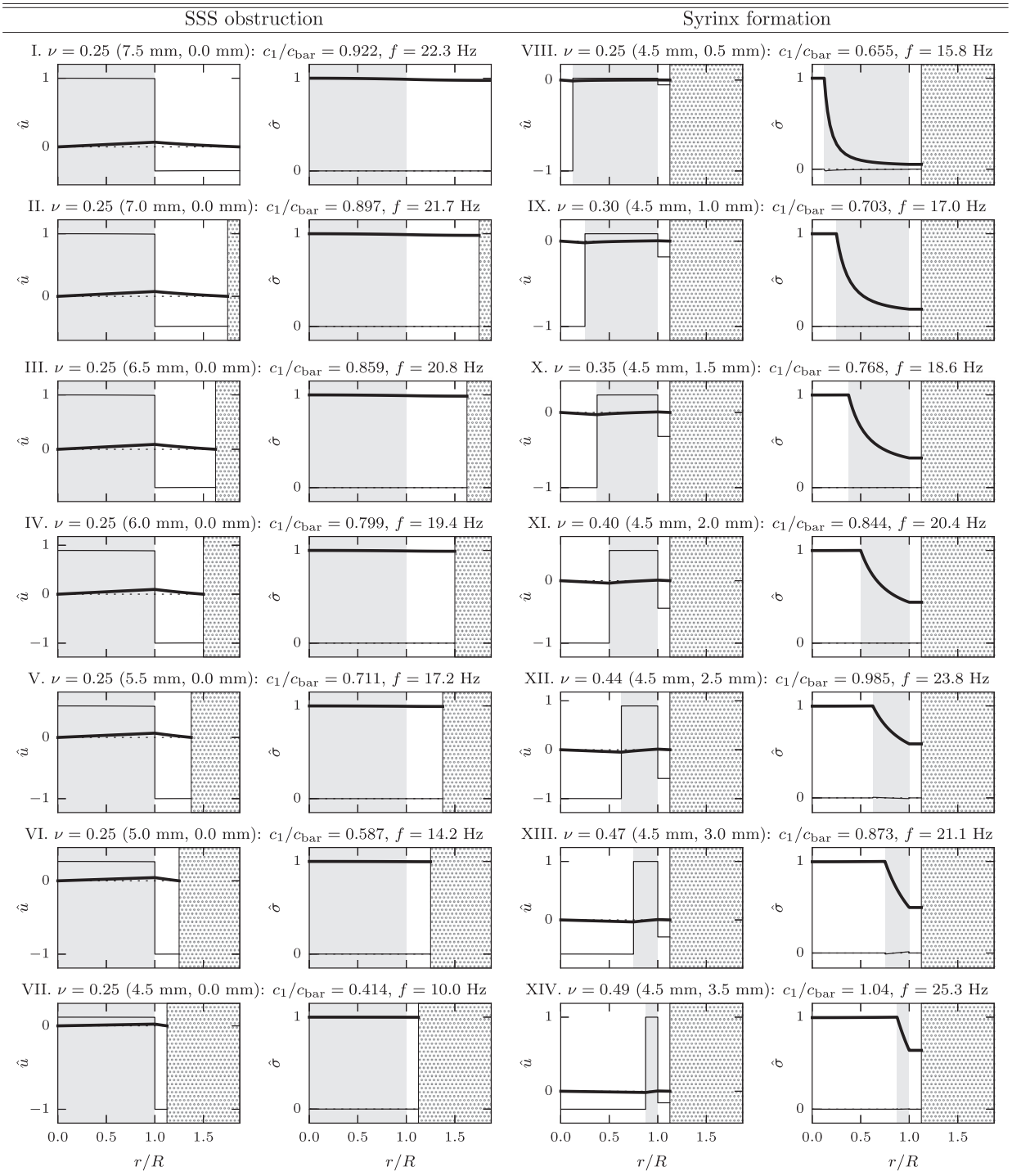

Fig. 14. Displacement (u) and stress (σ) mode shapes of mode 1 during states I–XIV of the simulated pathological sequence depicted in Fig. 12(a), which have been normalized by their wavelength-specific displacement and stress maxima, respectively; i.e., $\max(u) = \max(u_z)$, $\max(\sigma) = \max(\sigma_{rr})$, therefore $\hat{u}_r = u_r/\max(u_z)$, $\hat{u}_z = u_z/\max(u_z)$, $\hat{\sigma}_{rr} = \sigma_{rr}/\max(\sigma_{rr})$, $\hat{\sigma}_{rz} = \sigma_{rz}/\max(\sigma_{rr})$. Anatomical shading as per Fig. 13; thick lines (——) correspond to radial displacement ($\hat{u}_r$) and normal stress ($\hat{\sigma}_{rr}$); thin lines (———) correspond to axial displacement ($\hat{u}_z$) and shear stress ($\hat{\sigma}_{rz}$). The Poisson's ratio, dural radius, syrinx radius, non-dimensional speed (c_0/c_{bar}) and the frequency (f) are provided for each state; r_{syrinx} is the syrinx radius, r_{dura} is the dural radius, R is the radius of the spinal cord, Λ is the wavelength and $c_{\text{bar}} = \sqrt{E/\rho}$. Non-varying fluid, solid and geometrical parameter values are taken from Table 2.

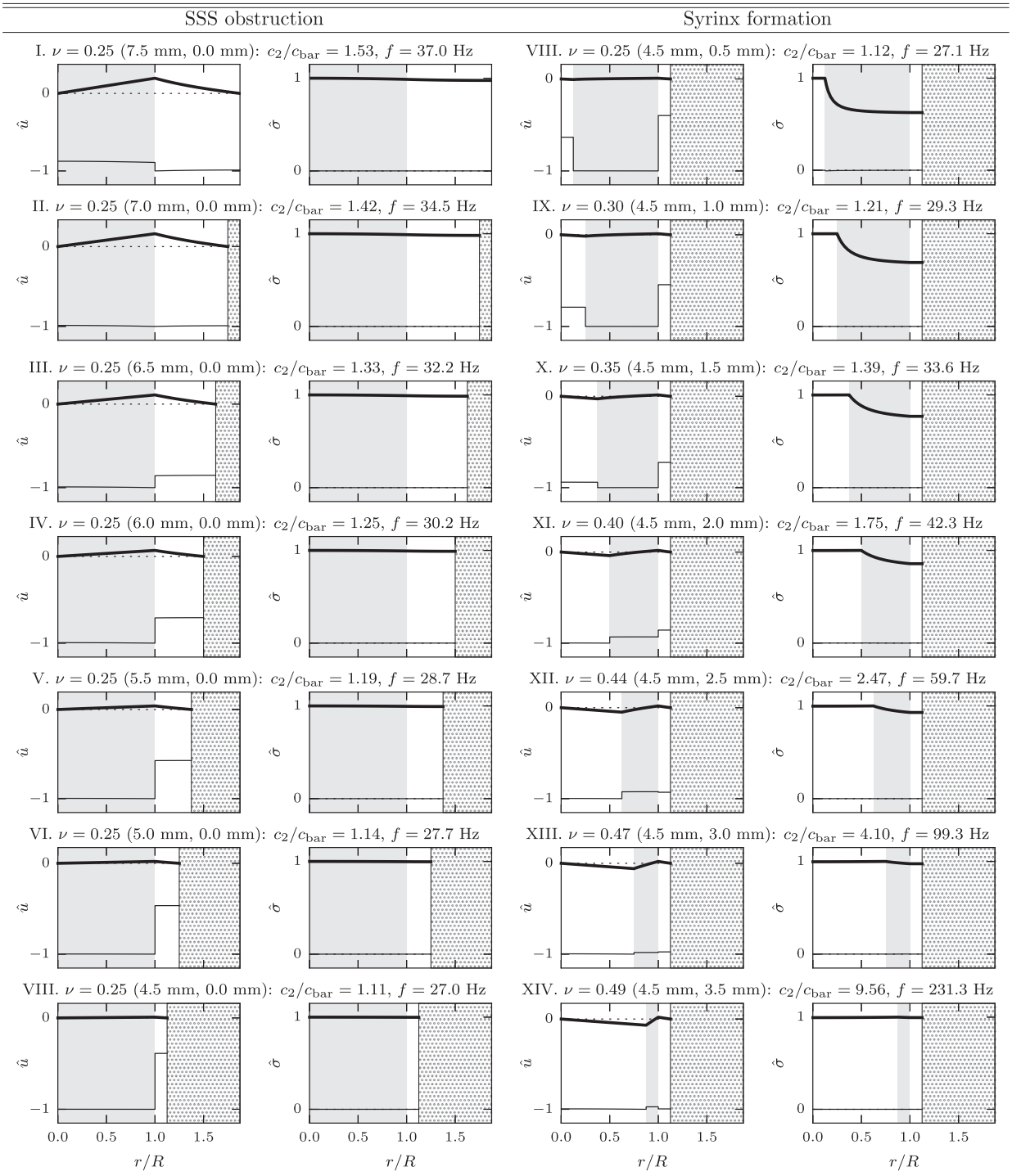

Fig. 15. Displacement (u) and stress (σ) mode shapes of mode 2 during states I–XIV of the simulated pathological sequence depicted in Fig. 12(a), which have been normalized by their wavelength-specific displacement and stress maxima, respectively; i.e., $\max(u) = \max(u_z)$, $\max(\sigma) = \max(\sigma_{rr})$, therefore $\hat{u}_r = u_r/\max(u_z)$, $\hat{u}_z = u_z/\max(u_z)$, $\hat{\sigma}_{rr} = \sigma_{rr}/\max(\sigma_{rr})$, $\hat{\sigma}_{rz} = \sigma_{rz}/\max(\sigma_{rr})$. Anatomical shading as per Fig. 13; thick lines (——) correspond to radial displacement ($\hat{u}_r$) and normal stress ($\hat{\sigma}_{rr}$); thin lines (———) correspond to axial displacement ($\hat{u}_z$) and shear stress ($\hat{\sigma}_{rz}$). The Poisson's ratio, dural radius, syrinx radius, non-dimensional speed (c_0/c_{bar}) and the frequency (f) are provided for each state; r_{syrinx} is the syrinx radius, r_{dura} is the dural radius, R is the radius of the spinal cord, Λ is the wavelength and $c_{\text{bar}} = \sqrt{E/\rho}$. Non-varying fluid, solid and geometrical parameter values are taken from Table 2.

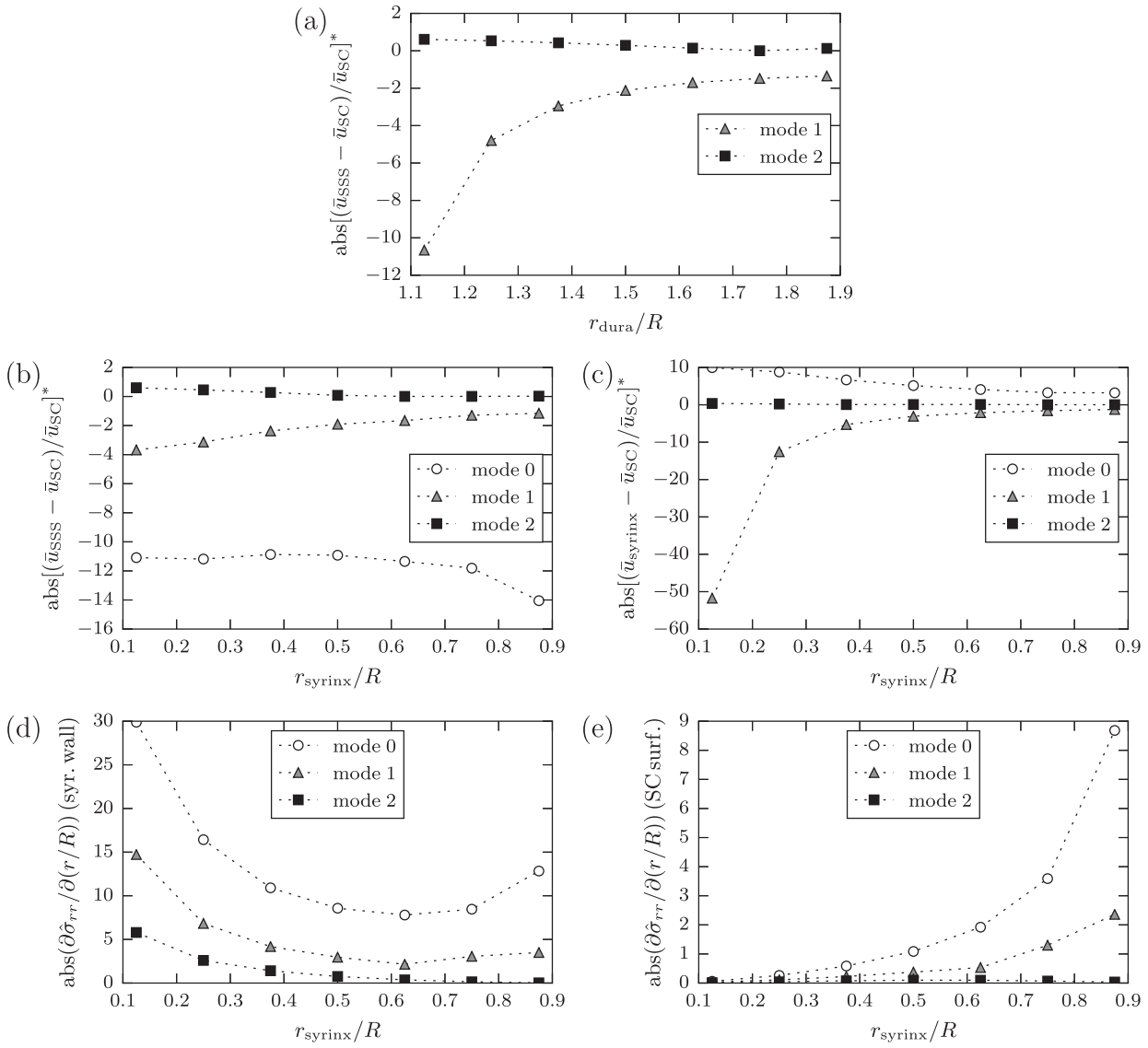

Fig. 16. Analysis of the mode shapes presented in Figs. 13–15 of the simulated pathological sequence depicted in Fig. 12(a). Plot (a) presents the movement of fluid in the spinal subarachnoid space (SSS) relative to the motion of the spinal cord (SC), termed the SSS fluid slosh ratio (abs $[(\bar{u}_{\mathrm{SSS}} - \bar{u}_{\mathrm{SC}})/\bar{u}_{\mathrm{SC}}]^*$), for modes 1 and 2 during states I–VII of the SSS blockage, which are indicated by their non-dimensional dural radius (r_{dura}/R); i.e., before the formation of the syrinx. Plots (b) and (c) show the SSS fluid slosh ratio and the syrinx fluid slosh ratio (abs $[(\bar{u}_{\mathrm{syrinx}} - \bar{u}_{\mathrm{SC}})/\bar{u}_{\mathrm{SC}}]^*$), respectively, for modes 0, 1 and 2 during states VIII–XIV, i.e., during syrinx formation. The quantities $\bar{u}_{\mathrm{SC}}$ and $\bar{u}_{\mathrm{SSS}}$ are the $\hat{u}_z$ values averaged over the SC and SSS regions, respectively; the asterisks in abs $[(\bar{u}_{\mathrm{SSS}} - \bar{u}_{\mathrm{SC}})/\bar{u}_{\mathrm{SC}}]^*$ and abs $[(\bar{u}_{\mathrm{syrinx}} - \bar{u}_{\mathrm{SC}})/\bar{u}_{\mathrm{SC}}]^*$ signify multiplication by the signs of $\bar{u}_{\mathrm{SSS}}/\bar{u}_{\mathrm{SC}}$ and $\bar{u}_{\mathrm{syrinx}}/\bar{u}_{\mathrm{SC}}$, respectively, so that a positive sign indicates in phase motion and a negative sign indicates out of phase motion. Plots are presented of the radial stress gradient (abs $(\partial\hat{\sigma}_{rr}/\partial(r/R))$) during syrinx formation (states VIII–XIV) for modes 0, 1 and 2 in (d) at the syrinx wall and in (e) at the SC surface. r_{syrinx} is the syrinx radius, r_{dura} is the dural radius and R is the radius of the spinal cord. Non-varying fluid, solid and geometrical parameter values are taken from Table 2.

remains feasible (Elliott et al., 2013). Likewise, concentrations of stress in the SC tissue surrounding a syrinx are likely to be detrimental; an outward normal stress on the inner wall of the cord favours syrinx formation and expansion, and a shear stress may contribute to the parallel separation of nerve fibres, potentially leaving a collapsed cavity where fluid may accumulate.

We begin by characterising the obstruction of the SSS. Fig. 14 I–VII shows that in mode 1 as the SSS becomes increasingly obstructed, the amplitude of axial SSS motion increases relative to that of the SC, but they always remain out of phase. The opposite trend occurs for axial displacement in mode 2, with both fluid and solid moving in phase; see Fig. 15 I–VII. This sloshing-type motion of CSF in the SSS is plotted in Fig. 16(a); $\bar{u}_{\mathrm{SC}}$ and $\bar{u}_{\mathrm{SSS}}$ are the $\hat{u}_z$ values averaged over the SC region ($0 \le r/R \le 1$) and SSS region ($1 \le r/R \le r_{\mathrm{dura}}/R$), respectively; the asterisk in $\mathrm{abs}[(\bar{u}_{\mathrm{SSS}} - \bar{u}_{\mathrm{SC}})/\bar{u}_{\mathrm{SC}}]^*$ signifies multiplication by the sign of $\bar{u}_{\mathrm{SSS}}/\bar{u}_{\mathrm{SC}}$, i.e., positive indicates in-phase motion, negative indicates out-of-phase motion.

When the syrinx appears, we need to consider the movement of the fluids inside and outside the SC by all three wave modes. For

mode 0, from Fig. 13 we see that the SC scarcely moves in comparison to the fluids (VIII–XIV), and the growth of the syrinx corresponds to greater amplitudes of SSS fluid motion (out of phase) and smaller amplitudes of syrinx fluid motion (in phase); these trends are shown in Fig. 16(b) and (c), respectively. The situation is different for mode 1, shown in Fig. 14 VIII–XIV. Here the SC, initially almost stationary, increases in displacement amplitude as the syrinx expands, eventually dominating over the fluid motions either side. The SSS fluid motion is out of phase with the SC and grows and then decays in amplitude, but is always reducing in amplitude relative to the SC (Fig. 16(b)). The motion of the syrinx fluid is also out of phase with that of the SC and its amplitude shows the opposite trend to the SC, with its initially large amplitude gradually diminishing with the expansion of the cavity (Fig. 16(c)). Finally, we consider the evolution of the axial displacement mode shapes of mode 2 in Fig. 15 VIII–XIV. The overall behaviour is that the motions of the SC and the fluids in the syrinx and SSS, always in phase, eventually reach the same amplitude as the syrinx becomes fully expanded. Both fluids have lower amplitudes than the SC although the syrinx fluid amplitude is always greater than that of the SSS fluid. The relative fluid motions are plotted in Fig. 16(b) and (c).

We now turn our attention to radial stress concentration in the SC tissue. Although the eigenvectors do not contain magnitude information, we can find stress concentrations by identifying regions of high gradient; i.e., a high localisation indicates the potential for high stress magnitude. From Figs. 13–15 we observe that in all three modes the peak gradient is initially adjacent the syrinx when the syrinx is small (VIII) but as the syrinx expands the stress profiles become of almost uniform gradient (IX–XIV). Fig. 16(d) and (e) plot the absolute values of the stress gradients at the syrinx wall and at the SC surface, respectively. At the syrinx wall, all three modes have a maximum stress gradient when the syrinx is smallest. For mode 2 this stress gradient diminishes monotonically as the syrinx expands, whereas for modes 0 and 1 there is a minimum stress gradient for an intermediate non-dimensional syrinx radius of 0.625. This implies that syrinx expansion driven by radial stress concentration would be more likely to halt at a radius around half that of the SC, rather than continue until the SC became a thin-walled tube. The stress gradient at the SC surface increases with the expansion of the syrinx for modes 0 and 1 but essentially reduces towards zero for mode 2. This suggests that the thin pia mater membrane that surrounds the SC will be required to take on an increasing proportion of the radial load imparted by modes 0 and 1 as the syrinx expands, whereas mode 2 will tend to be borne by the SC alone.

3.3.6. Clinical implications of the results

We have investigated the progression of CSF blockage and syrinx formation in simulations of the development sequence of post-traumatic syringomyelia.

While the SC remains intact, this modelling does not predict any state suggestive of syrinx formation; the dominant normal stress remains of uniform profile across the cord cross section (Figs. 14 and 15). At shorter wavelengths, the peak normal stress does tend to shift to the centre of the SC but there are no significant stress gradients (Fig. 6). The cause of syrinx genesis remains an open question (for a recent engineering evaluation of proposed hypotheses, see Elliott et al. (2013)). Once the post-traumatic syrinx is present, however, our model makes the following predictions.

Our results demonstrate a relative motion of the syrinx fluid to the SC tissue, either in phase or out of phase, depending on the wave mode, the syrinx radius and degree of CSF blockage in the SSS; modes 0 and 1 produce the larger amplitude movements. Therefore, Williams's 'slosh' hypothesis that the inertia of such fluid motion could induce stress in the SC tissue and thereby extend the syrinx remains feasible.

We submit that the pia mater membrane serves to maintain the stress in the SC at a healthy level by bearing an increasing proportion of the load as the syrinx expands. In Fig. 16(e) we saw that, in the absence of a separate pia mater, the normal stress concentration at the SC surface caused by modes 0 and 1 increases as the syrinx radially expands. As the pia mater is much stiffer than the SC tissue, it would bear this load.

Finally, we return to the question of homeostasis—despite the associated neurological damage, is there any benefit in the presence of a syrinx? We propose two hypotheses:

1. *Syrinx expansion serves to alleviate the stress concentration induced in SC tissue by the sloshing motion of syrinx fluid.* As demonstrated in Fig. 16(c), as the syrinx radially expands, the relative motion between the syrinx fluid and the surrounding SC tissue in wave modes 0, 1 and 2 diminishes. This would tend to favour shorter but thicker syrinxes, which would localise neurological damage to fewer spinal levels.
2. *Syrinx expansion to an intermediate radius serves to minimise stress concentration in the SC tissue adjacent to the syrinx wall.* Fig. 16(d) shows that modes 0 and 1 will have a minimum normal stress in the syrinx wall for a non-dimensional syrinx radius of 0.625.

Therefore, both of these homeostatic mechanisms may serve to reduce the damage otherwise caused by the underlying pathological processes leading to a syrinx in the first place (e.g., arachnoiditis, scar tissue formation, Chiari malformation).

Surgical experience tells us that no treatment works as intended for all patients. We did not simulate any treatments in this modelling study. Nonetheless, given that normal stress in the wall of the syrinx has the same magnitude as the syrinx fluid pressure, our hypothesized homeostatic mechanisms would be aided by treatments that lower pressure in the syrinx. On this basis, anatomical realignment (arachnoid lysis and pseudomeningocele formation) and shunts would be beneficial as they equilibrate the syrinx fluid pressure with that outside the SC (thereby stopping the filling mechanism). Further modelling is warranted, though, to evaluate such therapeutic mechanisms.

4. Conclusion

In this paper we developed 2D axisymmetric models of a cylindrically layered elastic fluid–solid waveguide and solved the harmonic eigenvalue problem. We used these models as an analogue of the spinal canal to investigate the wave characteristics of post-traumatic syringomyelia.

The speeds of modes 0, 1 and 2 match the analytical solutions at the long-wave limit (Young, Lamb and constrained longitudinal waves, respectively), and the short-wave speeds of mode 1 match the theoretical values of Rayleigh (solid) and Stonely (solid–fluid) surface waves for the elastic cylinder only and the elastic cylinder with the surrounding annulus of fluid, respectively. At these long- and short-wavelength limits the waves are non-dispersive. Furthermore, we showed that for an elastic cylinder (SC) with an inner fluid conduit (syrinx) of half its diameter, mode 0 waves with wavelength approximately equal to the diameter of the elastic cylinder are also non-dispersive. From the mode shape analysis we found that at long wavelengths axial displacement dominates over radial, normal stress dominates over shear but these become of the same order of magnitude as the wavelength approaches the radius of the elastic cylinder (SC). Wave modes 0 and 1 contribute to the relative movement between the elastic cylinder and the fluid contained within, akin to the sloshing motion of syrinx fluid described by Williams, and modes 0, 1 and 2 involve normal stress concentrations in the inner wall of the elastic cylinder (SC tissue) adjacent to the contained fluid (syrinx). In contrast to wave modes 0 and 1, the phase speed of mode 2 is strongly dependent on the Poisson's ratio of the elastic cylinder (SC) and on the radius of the inner fluid conduit (syrinx), particularly at long wavelengths.

We have simulated the progression sequence of post-traumatic syringomyelia, showing that the stress induced by syrinx fluid sloshing diminishes with the continued radial expansion of the syrinx. Furthermore, the largest normal stress concentrations at the syrinx boundary, which appear directly during the passage of wave modes 0 and 1, also diminish with initial expansion of the syrinx; however, they reach a minimum for intermediate syrinx diameters. Therefore, we hypothesize that syrinx development may be part of a homeostatic mechanism to alleviate stress in the SC.

The choices of inviscid fluid and linear elastic solid were made to limit the number of physical parameters to better demonstrate the numerical method and the physical interpretation of the results. However, by modelling all the layers as poroelastic with differing porosities it would be possible to include fluid viscosity in the syrinx and SSS, more realistically treat the fluid-saturated tissue, and by adding extra layers one could also include the pia mater and permit the dura mater to be flexible, thereby enabling additional wave modes. This would also allow investigation of the variability of the (poro)elastic properties of the SC with syrinx distension, a key area for future development when our present hypothesis for homeostasis is further refined and consolidated. The modelling techniques presented and deployed in the present paper serve as a platform for more realistic modelling of the spinal-cord system.

Acknowledgements

We acknowledge the support of both the Australian Research Council through the project DP0559408 and the WA State Centre of Excellence in eMedicine. DAL's time has been supported in the U.K. by Engineering and Physical Sciences Research Council Programme Grant EP/N016602/1. We also thank Dr. Ian Davies and Dr. Garry Leadbeater from the Department of Mechanical Engineering, Curtin University, for fruitful discussions.

References

Adamou, A.T.I., Craster, R.V., 2004. Spectral methods for modelling guided waves in elastic media. J. Acoust. Soc. Am. 116 (3), 1524–1535.
Al-Mousawi, M.M., 1986. On experimental studies of longitudinal and flexural wave propagations: an annotated bibliography. Appl. Mech. Rev. 39 (6), 853–865.
Anderson, E., Bai, Z., Bischof, C., Blackford, S., Demmel, J., Dongarra, J., Croz, J.D., Greenbaum, A., Hammarling, S., McKenney, A., Sorensen, D., 1999. LAPACK Users' Guide 3rd ed. Society for Industrial and Applied Mathematics, Philadelphia, PA.
Aris, R., 1956. On the dispersion of a solute in a fluid flowing through a tube. Proc. R. Soc. Lond. 235, 67–77.
Bancroft, D., 1941. The velocity of longitudinal waves in cylindrical bars. Phys. Rev. 59 (7), 588–593.
Beatty, M.F., Stalnaker, D.O., 1986. The Poisson function of finite elasticity. J. Appl. Mech. 53, 807–813.
Berkouk, K., Carpenter, P.W., Lucey, A.D., 2003. Pressure wave propagation in fluid-filled co-axial elastic tubes part 1: basic theory. ASME J. Biomech. Eng. 125 (6), 852–856.
Berselli, L.C., Guerra, F., Mazzola, B., Sinibaldi, E., 2014. Pulsatile viscous flows in elliptical vessels and annuli: solution to the inverse problem, with applications to blood and cerebrospinal fluid flow. SIAM J. Appl. Math. 74 (1), 40–59.
Bertram, C.D., Brodbelt, A.R., Stoodley, M.A., 2005. The origins of syringomyelia: numerical models of fluid/structure interactions in the spinal cord. ASME J. Biomech. Eng. 127 (7), 1099–1109.
Bertram, C.D., Heil, M., 2015. Effects of adding poroelasticity to an existing FSI model of spinal CSF dynamics in syringomyelia with adjacent subarachnoid space stenosis interactions: porous effects. In: Proceedings of the 3rd CSF Dynamics Symposium, Olivier Baledent and Diane de Zelicourt, Le logis du Roy, Amiens, France http://csfdynamics.org/amiens2015/
Bertram, C.D., Bilston, L.E., Stoodley, M.A., 2008. Tensile radial stress in the spinal cord related to arachnoiditis or tethering: a numerical model. Med. Biol. Eng. Comput. 46, 701–707.
Bertram, C.D., Russell, M.J., Heil, M., 2014. Modelling of spinal-cord fluid-structure interactions: porous effects. In: Proceedings of the 7th World Congress of Biomechanics, Boston, USA, https://esbiomech.org/7th-world-congress-on-biomechanics/.
Bertram, C.D., 2009. A numerical investigation of waves propagating in the spinal cord and subarachnoid space in the presence of a syrinx. J. Fluids Struct. 25, 1189–1205.
Bertram, C.D., 2010. Evaluation by fluid/structure-interaction spinal-cord simulation of the effects of subarachnoid-space stenosis on an adjacent syrinx. ASME J. Biomech. Eng. 132 (6), 061009.
Bilston, L.E., Thibault, L.E., 1996. The mechanical properties of the human cervical spinal cord in vitro. Ann. Biomed. Eng. 24 (1), 67–74.
Bilston, L.E., Fletcher, D.F., Brodbelt, A.R., Stoodley, M.A., 2003. Arterial pulsation-driven cerebrospinal fluid flow in the perivascular space: a computational model. Comput. Methods Biomech. Biomed. Eng. 6 (4), 235–241.
Bilston, L.E., Fletcher, D.F., Stoodley, M.A., 2006. Focal spinal arachnoiditis increases subarachnoid space pressure: a computational study. Clin. Biomech. 21,

579–584.
Bilston, L.E., Stoodley, M.A., Fletcher, D.F., 2010. The influence of the relative timing of arterial and subarachnoid space pulse waves on spinal perivascular cerebrospinal fluid flow as a possible factor in syrinx developments. J. Neurosurg. 112 (4), 808–813.
Boost. 2008. Boost c++ libraries. ⟨http://www.boost.org⟩.
Brodbelt, A.R., Stoodley, M.A., 2003. Post-traumatic syringomyelia: a review. J. Clin. Neurosci. 10 (4), 401–408.
Burke, M.A., Lucey, A.D., Howell, R.M., Elliott, N.S.J., 2014. Stability of a flexible insert in one wall of an inviscid channel flow. J. Fluids Struct. 48, 435–450.
Carpenter, P.W., Berkouk, K., Lucey, A.D., 1999. A theoretical model of pressure wave propagation in the human spinal CSF system. Eng. Mech. 6, 213–228.
Carpenter, P., Berkouk, K., Lucey, A., 2003. Pressure wave propagation in fluid-filled co-axial elastic tubes part 2: mechanisms for the pathogenesis of syringomyelia. ASME J. Biomech. Eng. 125 (6), 857–863.
Cathalifaud, P., Maher, M., Zagzoule, M., 2015. A one-dimensional model of wave propagation within the co-axial viscous fluid filled spinal cavity. In: Proceedings of the 3rd CSF Dynamics Symposium, Olivier Baledent and Diane de Zelicourt, Le logis du Roy, Amiens, France, http://csfdynamics.org/amiens2015/.
Chen, Y., Tang, Y., Vogel, L.C., DeVivo, M.J., 2013. Causes of spinal cord injury. Top. Spinal Cord Injury Rehabil. 19 (1), 1–8.
Cheng, S., Stoodley, M.A., Wong, J., Hemley, S., Fletcher, D.F., Bilston, L.E., 2012. The presence of arachnoiditis affects the characteristics of CSF flow in the spinal subarachnoid space: a modelling study. J. Biomech. 45 (7), 1186–1191.
Cirovic, S., Kim, M., 2012. A one-dimensional model of the spinal cerebrospinal-fluid compartment. J. Biomech. Eng. 134 (2), 021005.
Cirovic, S., 2009. A coaxial tube model of the cerebrospinal fluid pulse propagation in the spinal column. ASME J. Biomech. Eng. 131 (2), 021008.
Clarke, E.C., Fletcher, D.F., Stoodley, M.A., Bilston, L.E., 2013. Computational fluid dynamics modelling of cerebrospinal fluid pressure in Chiari malformation and syringomyelia. J. Biomech. 46 (11), 1801–1809.
Davies, R.M., 1948. A critical study of the Hopkinson pressure bar. Philos. Trans. R. Soc. Lond. Ser. A 240 (821), 375–457.
Drøsdal, I.N., Mardal, K.-A., Støverud, K., Haughton, V., 2013. Effect of the central canal in the spinal cord on fluid movement within the cord. Neuroradiol. J. 26 (5), 585–590.
Elliott, N.S.J., Lockerby, D.A., Brodbelt, A.R., 2009. The pathogenesis of syringomyelia: A re-evaluation of the elastic-jump hypothesis. ASME J. Biomech. Eng. 131 (4), 044503.
Elliott, N.S.J., Lucey, A.D., Lockerby, D.A., Brodbelt, A.R., 2010. Wave propagationin an elastic waveguide: fluid-structure interactions in a spinal disease. In: Teh, K., Davies, I., Howard, I. (Eds.), Proceedings of the 6th Australasian Congress on Applied Mechanics, 1434–1443.
Elliott, N.S.J., Lockerby, D.A., Brodbelt, A.R., 2011. A lumped-parameter model of the cerebrospinal system for investigating arterial-driven flow in posttraumatic syringomyelia. Med. Eng. Phys. 33, 874–882.
Elliott, N.S.J., Bertram, C.D., Martin, B.A., Brodbelt, A.R., 2013. Syringomyelia: a review of the biomechanics. J. Fluids Struct. 40, 1–24.
Elliott, N.S.J., Lucey, A.D., Lockerby, D.A., Brodbelt, A.R., 2014. Syringomyelia and the fluid-structure interactions of a cerebrospinal waveguide. In: Proceedings of the ASME 2014 Pressure Vessels and Piping Conferences, vol. 4, Fluid Struct. Interact., pp. PVP2014–29096: V004T04A083.
Elliott, N.S.J., 2012. Syrinx fluid transport: modeling pressure-wave-induced flux across the spinal pial membrane. J. Biomech. Eng. 134 (3), 031006.
England, M.A., Wakeley, J.W., 2006. Color Atlas of the Brain and Spinal Cord: An Introduction to Normal Neuroanatomy, 2nd ed., Mosby.
Fischbein, N.J., Dillon, W.P., Cobbs, C., Weinstein, P.R., 1999. The 'presyrinx' state: a reversible myelopathic condition that may precede syringomyelia. Am. J. Neuroradiol. 20, 7–20.
Fischbein, N.J., Dillon, W.P., Cobbs, C., Weinstein, P.R., 2000. The "presyrinx" state: is there a reversible myelopathic condition that may precede syringomyelia? Neurosurg. Focus 8, 1–13.
Gama, B.A., Lopatnikov, S.L., Gillespie, J.W., Jr., 2004. Hopkinson bar experimental technique: a critical review. Appl. Mech. Rev. 57 (4), 223–250.
Gottschalk, A., Schmitz, B., Mauer, U.M., Bornstedt, A., Steinhoff, S., Danz, B., Schlötzer, W., Rasche, V., 2010. Dynamic visualization of arachnoid adhesions in a patient with idiopathic syringomyelia using high-resolution cine magnetic resonance imaging at 3T. J. Magn. Reson. Imaging 32 (1), 218–222.
Greitz, D., Ericson, K., Flodmark, O., 1999. Pathogenesis and mechanics of spinal cord cysts: a new hypothesis based on magnetic resonance studies of cerebrospinal fluid dynamics. Int. J. Neuroradiol. 5, 61–78.
Gupta, S., Poulikakos, D., Kurtcuoglu, V., 2008. Analytical solution for pulsatile viscous flow in a straight elliptic annulus and application to the motion of the cerebrospinal fluid. Phys. Fluids 20, 093607.
Harris, P.J., Hardwidge, C., 2010. A porous finite element model of the motion of the spinal cord. In: Constanda, C., Pérez, M.E. (Eds.), Integral Methods in Science and Engineering (Chapter 18) 2. Springer, 193–201, Computational Methods.
Helgeland, A., Mardal, K.-A., Haughton, V., Reif, B.A.P., 2014. Numerical simulations of the pulsating flow of cerebrospinal fluid flow in the cervical spinal canal of a Chiari patient. J. Biomech. 47 (5), 1082–1090.
Hentschel, S., Mardal, K.-A., Løvgren, A.E., Linge, S., Haughton, V., 2010. Characterization of cyclic CSF flow in the foramen magnum and upper cervical spinal canal with MR flow imaging and computational fluid dynamics. Am. J. Neuroradiol. 31, 997–1002.
Hopkinson, B., 1914. A method of measuring the pressure produced in the detonation of high explosives or by the impact of bullets. Philos. Trans. R. Soc. Lond. Ser. A 213, 437–456.
Hudson, G.E., 1943. Dispersion of elastic waves in solid circular cylinders. Phys. Rev. 63 (1–2), 46–51.
Ichihara, K., Taguchi, T., Shimada, Y., Sakuramoto, I., Kawano, S., Kawai, S., 2001. Gray matter of the bovine cervical spinal cord is mechanically more rigid and fragile than the white matter. J. Neurotrauma 18 (3), 361–367.
Jackson, J.R., Williams, B., 1979. Errors in velocity measurement by the pitot tube principle in fluids with slowly propagated pressure waves. J. Biomed. Eng. 1, 50–54.
Kalata, W., Martin, B.A., Oshinski, J.N., Jerosch-Herold, M., Royston, T.J., Loth, F., 2009. MR measurement of cerebrospinal fluid velocity wave speed in the spinal canal. Proc. IEEE Trans. Biomed. Eng. 56 (6), 1765–1768.
Karpfinger, F., Gurevich, B., Bakulin, A., 2008a. Modeling of axisymmetric wave modes in a poroelastic cylinder using spectral method. J. Acoust. Soc. Am. Express Lett. 124 (4), EL230–EL235.
Karpfinger, F., Gurevich, B., Bakulin, A., 2008b. Modeling of wave dispersion along cylindrical structures using the spectral method. J. Acoust. Soc. Am. 124 (2), 859–865.
Karpfinger, F., Valero, H.P., Gurevich, B., Bakulin, A., Sinha, B., 2010. Tube wave signatures in cylindrically layered poroelastic media computed with spectral method. Geophys. J. Int. 183, 1005–1013.
Kiernan, J.A., 1998. Barr's the Human Nervous System, An Anatomical Viewpoint, Lippincott Williams & Wilkins.
Kim, K.H., Park, J.Y., Kuh, S.U., Chin, D.K., Kim, K.S., Cho, Y.E., 2013. Changes in spinal canal diameter and vertebral body height with age. Yonsei Med. J. 54 (6), 1498–1504.
Klekamp, J., Batzdorf, U., Samii, M., Bothe, H.W., 1997. Treatment of syringomyelia associated with arachnoid scarring caused by arachnoiditis or trauma. J. Neurosurg. 86, 233–240.
Klekamp, J., Volkel, K., Bartels, C.J., Samii, M., 2001. Disturbances of cerebrospinal fluid flow attributable to arachnoid scarring cause interstitial edema of the cat spinal cord. Neurosurgery 48, 174–185.
Klekamp, J., 2002. The pathophysiology of syringomyelia–historical overview and current concept. Acta Neurochir. 144, 649–664.
Kolsky, H., 1949. An investigation of the mechanical properties of materials at very high rates of loading. Proc. Phys. Soc. Lond. Sect. B 62 (II-B), 676–700.
Kolsky, H., 1953. Stress Waves in Solids.
Linge, S.O., Haughton, V., Løvgren, A.E., Mardal, K.A., Langtangen, H.P., 2010. CSF flow dynamics at the craniovertebral junction studied with an idealized model of the subarachnoid space and computational flow analysis. Am. J. Neuroradiol. 31, 185–192.
Linge, S.O., Haughton, V., Løvgren, A.E., Mardal, K.A., Helgeland, A., Langtangen, H.P., 2011. Effect of tonsillar herniation on cyclic CSF flow studied with computational flow analysis. Am. J. Neuroradiol. 32, 1472–1481.
Linge, S.O., Mardal, K.-A., Helgeland, A., Heiss, J.D., Haughton, V., 2014. Effect of craniovertebral decompression on CSF dynamics in Chiari malformation type I studied with computational fluid dynamics. J. Neurosurg. Spine 21, 559–564.

Lockey, P., Poots, G., Williams, B., 1975. Theoretical aspects of the attenuation of pressure pulses within cerebrospinal fluid pathways. Med. Biol. Eng. Comput. 13, 861–869.
Loth, F., Yardimci, M.A., Alperin, N., 2001. Hydrodynamic model of cerebrospinal fluid motion within the spinal cavity. ASME J. Biomech. Eng. 123, 71–79.
Love, A.E.H., 1927. The Mathematical Theory of Elasticity 4th ed.. Dover (reprint).
Martin, B.A., Reymond, P., Novy, J., Balédent, O., Stergiopulos, N., 2012. A coupled hydrodynamic model of the cardiovascular and cerebrospinal fluid system. Am. J. Physiol.-Heart Circ. Physiol. 302 (7), H1492–H1509.
Martin, B.A., Kalata, W., Shaffer, N., Fischer, P., Luciano, M., Loth, F., 2013. Hydrodynamic and longitudinal impedance analysis of cerebrospinal fluid dynamics at the craniovertebral junction in type I Chiari malformation. PLoS One 8 (10), e75335.
Martin, B.A., Yiallourou, T.I., Pahlavian, S.H., Thyagaraj, S., Bunck, A.C., Loth, F., Sheffer, D.B., Kröger, J.R., Stergiopulos, N., 2016. Inter-operator reliability of magnetic resonance image-based computational fluid dynamics prediction of cerebrospinal fluid motion in the cervical spine. Ann. Biomed. Eng. 44 (5), 1524–1537.
Meyers, M.A., Chen, P.-Y., Lin, A.Y.-M., Seki, Y., 2008. Biological materials: structure and mechanical properties. Prog. Mater. Sci. 53, 1–206.
Milhorat, T.H., Kotzen, R.M., Anzil, A.P., 1994. Stenosis of central canal of spinal cord in man: incidence and pathological findings in 232 autopsy cases. J. Neurosurg. 80, 716–722.
Milhorat, T.H., Chou, M.W., Trinidad, E.M., Kula, R.W., Mandell, M., Wolpert, C., Speer, M.C., 1999. Chiari I malformation redefined: clinical and radiographic findings for 364 symptomatic patients. Neurosurgery 44, 1005–1017.
Morishita, Y., Naito, M., Hymanson, H., Miyazaki, M., Wu, G., Wang, J.C., 2009. The relationship between the cervical spinal canal diameter and the pathological changes in the cervical spine. Eur. Spine J. 18, 877–883.
Moriwaka, F., Tashiro, K., Tachibana, S., Yada, K., 1995. Epidemiology of syringomyelia in Japan–the nationwide survey. Rinsho Shinkeigaku 35, 1395–1397 (in Japanese).
Nakata, M., 2010. The MPACK (MBLAS/MLAPACK); A Multiple Precision Arithmetic Version of BLAS and LAPACK, version 0.6.7. ⟨http://mplapack.sourceforge.net⟩.
Norton, L., 2010. Spinal cord injury, Australia 2007–08. Technical Report Injury Research and Statistics Series no. 52, Cat. no. INJCAT 128, Australian Institute of Health and Welfare, Canberra.
Ozawa, H., Matsumoto, T., Ohashi, T., Sato, M., Kokuban, S., 2001. Comparison of spinal cord gray matter and white matter softness: measurement by pipette aspiration method. J. Neurosurg. Spine 2 95, 221–224.
Ozawa, H., Matsumoto, T., Ohashi, T., Sato, M., Kokuban, S., 2004. Mechanical properties and function of the spinal pia mater. J. Neurosurg. Spine 1 1, 122–127.
Pahlavian, S.H., Yiallourou, T., Tubbs, R.S., Bunck, A.C., Goodin, F.L.M., Raisee, M., Martin, B.A., 2014. The impact of spinal cord nerve roots and denticulate ligaments on cerebrospinal fluid dynamics in the cervical spine. PLoS One 9 (4), e91888.
Pahlavian, S.H., Bunck, A.C., Loth, F., Tubbs, R.S., Yiallourou, T., Kroeger, J.R., Heindel, W., Martin, B.A., 2015a. Characterization of the discrepancies between four-dimensional phase-contrast magnetic resonance imaging and in-silico simulations of cerebrospinal fluid dynamics. ASME J. Biomech. Eng. 137 (5), 051002.
Pahlavian, S.H., Loth, F., Luciano, M., Oshinski, J., Martin, B.A., 2015b. Neural tissue motion impacts cerebrospinal fluid dynamics at the cervical medullary junction: a patient-specific moving-boundary computational model. Ann. Biomed. Eng. 43 (12), 2911–2923.
Quigley, M.F., Iskandar, B., Quigley, M.A., Nicosia, M., Haughton, V., 2004. Cerebrospinal fluid flow in foramen magnum: temporal and spatial patterns at MR imaging in volunteers and in patients with Chiari I malformation. Radiology 232 (1), 229–236.
Roldan, A., Wieben, O., Haughton, V., Osswald, T., Chesler, N., 2009. Characterization of CSF hydrodynamics in the presence and absence of tonsillar ectopia by means of computational flow analysis. Am. J. Neuroradiol. 30, 941–946.
Russell, C.M., Choo, A.M., Tetzlaff, W., Chung, T.E., Oxland, T.R., 2012. Maximum principal strain correlates with spinal cord tissue damage in contusion and dislocation injuries in the rat cervical spine. J. Neurotrauma 29 (8), 1574–1585.
Rutkowska, G., Haughton, V., Linge, S., Mardal, K.-A., 2012. Patient-specific 3D simulation of cyclic CSF flow at the craniocervical region. Am. J. Neuroradiol. 33, 1756–1762.
Sakushima, K., Tsuboi, S., Yabe, I., Hida, K., Terae, S., Uehara, R., Nakano, I., Sasaki, H., 2012. Nationwide survey on the epidemiology of syringomyelia in Japan. J. Neurol. Sci. 313 (1–2), 147–152.
Saxena, T., Gilbert, J.L., Hasenwinkel, J.M., 2009. A versatile mesoindentation system to evaluate the micromechanical properties of soft, hydrated substrates on a cellular scale. J. Biomed. Mater. Res. Part A 90, 1206–1217.
Schwartz, E.D., Falcone, S.F., Quencer, R.M., Green, B.A., 1999. Posttraumatic syringomyelia: pathogenesis, imaging, and treatment. Am. J. Roentgenol. 173, 487–492.
Shaffer, N., Martin, B.A., Rocque, B., Madura, C., Wieben, O., Iskandar, B.J., Dombrowski, S., Luciano, M., Oshinski, J.N., Loth, F., 2014. Cerebrospinal fluid flow impedance is elevated in type I Chiari malformation. ASME J. Biomech. Eng. 136 (2), 021012.
Støverud, K.-H., Mardal, K.-A., Haughton, V., Langtangen, H.P., 2011. CSF flow in Chiari I and syringomyelia from the perspective of computational fluid dynamics. Neuroradiol. J. 24 (1), 20–23.
Støverud, K.-H., Langtangen, H.P., Haughton, V., Mardal, K.-A., 2013. CSF pressure and velocity in obstructions of the subarachnoid spaces. Neuroradiol. J. 26 (2), 218–226.
Støverud, K.-H., Alnæs, M., Langtangen, H.P., Haughton, V., Mardal, K., 2016. Poro-elastic modeling of syringomyelia - a systematic study of the effects of pia mater, central canal, median fissure, white and gray matter on pressure wave propagation and fluid movement within the cervical spinal cord. Comput. Methods Biomech. Biomed. Eng. 19 (6), 686–698.
Stockman, H.W., 2006. Effect of anatomical fine structure on the flow of cerebrospinal fluid in the spinal subarachnoid space. ASME J. Biomech. Eng. 128, 106–114.
Stockman, H.W., 2007. Effect of anatomical fine structure on the dispersion of solutes in the spinal subarachnoid space. ASME J. Biomech. Eng. 129 (5), 666–675.
Strick, E., Ginzbarg, A.S., 1956. Stonely-wave velocities for a fluid-solid interface. Bull. Seismol. Soc. Am. 46, 281–292.
Tan, K., Cheng, S., Bilston, L.E., 2013. Characterising soft tissues under large amplitude oscillatory shear and combined loading. J. Biomech. 46 (6), 1060–1066.
Tang, J.W., Nicolle, A.D., Klettner, C.A., Pantelic, J., Wang, L., Suhaimi, A.B., Tan, A.Y.L., Ong, G.W.X., Su, R., Sekhar, C., Cheong, D.D.W., Tham, K.W., 2013. Airflow dynamics of human jets: sneezing and breathing - potential sources of infectious aerosols. PLoS One 8 (4), e59970.
Tu, L.Y., Brennan, J.N., Sauer, J.A., 1953. Dispersion of ultrasonic pulse velocity in cylindrical rods. J. Acoust. Soc. Am. 27 (5), 550–555.
Wang, P.W., Olbricht, W.L., 2011. Fluid mechanics in the perivascular space. J. Theor. Biol. 247, 52–57.
Watson, E.J., 1983. Diffusion in oscillatory pipe flow. J. Fluid Mech. 133, 233–244.
Weideman, J.A.C., Reddy, S.C., 2000. A MATLAB differentiation matrix suite. ACM Trans. Math. Softw. 26 (4), 465–519.
Williams, B., 1972. Combined cisternal and lumbar pressure recordings in the sitting position using differential manometry. J. Neurol. Neurosurg. Psychiatry 35, 142–143.
Williams, B., 1976. Cerebrospinal fluid pressure changes in response to coughing. Brain 99, 331–346.
Williams, B., 1980. On the pathogenesis of syringomyelia: a review. J. R. Soc. Med. 73 (11), 798–806.
Williams, B., 1990. Syringomyelia. Neurosurg. Clin. N. Am. 1, 653–685.
Yew, E.H., Chen, C.S., 1978. Experimental study of dispersive waves in beam and rod using FFT. J. Appl. Mech. 45, 940–942.
Yiallourou, T.I., Kröger, J.R., Stergiopulos, N., Maintz, D., Martin, B.A., Bunck, A.C., 2012. Comparison of 4D phase-contrast MRI flow measurements to computational fluid dynamics simulations of cerebrospinal fluid motion in the cervical spine. PLoS One 7 (12), e52284.
Zemanek, J., Rudnick, I., 1961. Attenuation and dispersion of elastic waves in a cylindrical bar. J. Acoust. Soc. Am. 33 (10), 1238–1288.